Synthesis, Characterization and Catalytic Activity of Immobilized Metallic Nanoparticles

D I S S E R T A T I O N

zur Erlangung des akademischen Grades

d o c t o r r e r u m n a t u r a l i u m

(Dr. rer. nat.)
im Fach Chemie
eingereicht an der

Mathematisch-Naturwissenschaftlichen Fakultät I
Humboldt-Universität Berlin
von

Frau Dipl. Chem. Stefanie Wunder

Präsident der Humboldt-Universität zu Berlin:
Prof. Dr. Jan-Hendrik Olbertz

Dekan der Mathematisch-Naturwissenschaftlichen Fakultät:
Prof. Stefan Hecht, PhD

Gutachter/innen: 1. Prof. Dr. M Ballauff
2. Prof. Dr. K. Rademann

Eingereicht am: 24. 05. 2012
Tag der mündlichen Prüfung: 31. 10. 2012

"*The man who moves a mountain begins by carrying away small stones*."

~ old chinese proverb ~

Meiner Familie

Abstract

In this work, gold and platinum nanoparticles were synthesized into spherical polyelectrolyte brushes (SPB) in order to apply them as catalysts for kinetic studies of the reduction of *p*-nitrophenol by sodium borohydride. It was found that the reaction follows the Langmuir-Hinshelwood mechanism where both educts must adsorb onto the surface of the catalyst in order to react. Thereby, the rate determining step is the surface reaction of both educts. After the reaction, the product, *p*-aminophenol, desorbs from the surface and a free active site is formed. With this model the intrinsic reaction rate and the adsorption constants for both educts could be determined. The measurements at different temperatures allowed the calculation of the activation energy and the adsorption enthalpy and entropy of the educts.

Besides the reaction mechanism, the induction time of the reaction was analyzed. Here, it was shown that the reason of this delay time is a restructuring of the nanoparticle surface. The induction time is solely dependent on the concentration of *p*-nitrophenol on the surface of the nanoparticles and independent of the applied concentrations of borohydride. Moreover, hints for a spontaneous reconstruction of the nanoparticles without *p*-nitrophenol were found.

In the second part, the catalytic oxidation of morin by manganese oxide has been studied. These nanoparticles were embedded inside the polyelectrolyte layer of the SPB. Previous studies have shown that these nanostructures are of K^+-birnessite type, octahedral, edge-sharing MnO_6 with interlaying layers of potassium ions. These nanoparticles were used for systematic studies of the oxidation of morin with hydrogen peroxide. It was shown that in this case the reaction followed a Langmuir-Hinshelwood kinetics as well. Here, the intrinsic rate constants and the adsorption constants could be obtained for different temperatures. The activation energy and the adsorption enthalpy and entropy could be determined accordingly. The adsorption enthalpy is exothermic in both cases.

Key words: Langmuir-Hinshelwood mechanism, nanoparticles, spherical polyelectrolyte brushes, kinetics

Zusammenfassung

In dieser Arbeit wurden Gold- und Platin-Nanopartikel in sphärischen Polyelektolyt-Bürsten (SPB) synthetisiert. Diese wurden zu mechanistischen Untersuchungen der *p*-Nitrophenol-Reduktion mittels Natriumborhydrid herangezogen. Dabei konnte der Mechanismus der Reaktion auf der Oberfläche der Nanopartikel aufgeklärt werden. Die Reaktion folgt einem Langmuir-Hinshelwood Mechanismus. Hierbei adsorbieren beide Edukte auf die Oberfläche, bevor sie im geschwindigkeitsbestimmenden Schritt zu *p*-Aminophenol umgesetzt werden. Nach der Reaktion desorbiert das Reaktionsprodukt *p*-Aminophenol. Mittels des Langmuir-Hinshelwood Modells konnten für verschiedene Temperaturen die intrinsische Geschwindigkeitskonstante, sowie die Adsorptionskonstanten der Edukte bestimmt werden. Mit diesen Daten konnten dann die Enthalpie und Entropie der Adsorption der Edukte und die Aktivierungsenergie der intrinsischen Geschwindigkeitskonstante berechnet werden.

Neben dem Reaktionsmechanismus wurde ein weiteres Phänomen der *p*-Nitrophenol Reduktion untersucht, die Induktionszeit. Hierbei konnte gezeigt werden, dass diese Totzeit der Reaktion wahrscheinlich auf eine Restrukturierung der Nanopartikeloberfläche zurückzuführen ist. Diese Induktionszeit ist unabhängig von den eingesetzten Konzentrationen des Borhydrids, hingegen abhängig von der Konzentration an *p*-Nitrophenol auf der Oberfläche der Nanopartikel, was auf Restrukturierung der Nanopartikel durch *p*-Nitrophenol hindeutet. Zudem wurden Hinweise auf eine spontane Rekonstruktion der Nanopartikel gefunden, die unabhängig von der Konzentration des *p*-Nitrophenols ist.

Des Weiteren wurde die katalytische Oxidation von Morin mit Manganoxid Nanopartikeln untersucht. Diese sind in der Polyelektrolytschale der SPB immobilisiert. Vorausgegangene XRD-Messungen ergaben, dass diese aus K^+-Birnessit bestehen. Mit diesen MnO_x-Nanopartikel wurde die Oxidation von Morin systematisch untersucht. Analysen der Reaktionskinetik ergaben, dass auch in diesem Fall der Langmuir-Hinshelwood Mechanismus vorliegt. Hierbei konnten die Adsorptionskonstanten und Geschwindigkeitskonstanten für verschiedene Temperaturen ermittelt werden und somit die Aktivierungsenergie der Oxidation sowie die Adsorptionsenthalpie und Entropie der Edukte.

Schlagwörter: Langmuir-Hinshelwood-Mechanismus, Nanopartikel, Sphärische Polyelektrolyt-Bürsten, Kinetik

Content

1. Introduction 1

1.1 Stabilization of Metal Nanoparticles 1
1.2 Synthesis of Nanoparticles 2
1.3 Catalytic Model Reactions 3
1.3.1 Reduction of *p*-Nitrophenol 4
1.3.2 Oxidation of Flavonols 5
1.4 Objectives of this Thesis 7

2. Fundamentals 8

2.1 Polymer brushes 8
2.1.1 Spherical Polyelectrolyte Brushes (SPB) 9
2.1.2 Synthesis of Nanoparticles inside Spherical Polyelectrolyte Brushes 10
2.2 Heterogeneous catalysis 13
2.2.1 Adsorption Isotherms 13
2.2.2 Eley-Rideal Mechanism 17
2.2.3 Langmuir-Hinshelwood Mechanism 18
2.2.4 Rate controlled or diffusion controlled 20
2.2.5 Surface Reconstruction and Restructuring 21

3. Results and Discussion 25

3.1 Reduction of *p*-Nitrophenol – Literature Survey 25
3.1.1 Reaction Rate Constant 28
3.1.2 Activation Energy 33
3.1.3 Induction Time 39
3.2 Reduction of *p*-Nitrophenol Using Metal Nanoparticles inside SPB as Catalysts 40
3.2.1 Investigation of the Reaction Mechanism 43
3.2.2 Langmuir-Hinshelwood Reaction Mechanism 44
3.2.3 Adsorption Isotherms 46
3.2.4 Temperature dependence of the apparent rate constant 50
3.2.5 Thermodynamic Parameters 53
3.2.6 Compensation Plot 54
3.2.7 Induction Time 59
3.2.8 Kinetic of the Surface Restructuring 62
3.3 Catalysis by Manganese Oxides 67
3.4 Literature Survey for the Oxidation of Morin 67
3.4.1 Decomposition of H_2O_2 Catalyzed by Manganese Oxides 70

3.4.2 Oxidation Reactions Catalyzed by Manganese Oxides ... 71
3.5 Oxidation of Morin using SPB-MnO_x as Catalyst ... 72
3.5.1 The UV-vis Spectrum of Morin ... 73
3.5.2 The Role of Oxygen in the Oxidation of Morin ... 75
3.5.3 H_2O_2 as Oxidizing Agent ... 77
3.5.4 Kinetic Study of the Catalytic Morin Oxidation ... 79
3.5.5 Influence of the Buffer System on the Oxidation ... 80
3.5.6 Langmuir-Hinshelwood Model ... 82
3.5.7 Analysis of the Thermodynamic Parameters ... 87

4. Summary ... 90
5. Experimental Part ... 92

5.1 Equipment ... 92
5.1.1 TEM ... 92
5.1.2 DLS ... 92
5.1.3 NMR ... 93
5.1.4 Ultrafiltration ... 93
5.1.5 TGA ... 93
5.1.6 UV-vis spectroscopy ... 94
5.2 Chemicals ... 95
5.3 Synthesis ... 96
5.3.1 Photo initiator (HMEM) ... 96
5.3.2 Polystyrene Core Synthesis ... 96
5.3.3 Synthesis of the Polyelectrolyte Brushes grafting on the Polystyrene Core ... 97
5.3.4 Metallic Nanoparticles ... 97
5.3.5 Manganese Oxide Nanoparticles ... 98
5.3.6 Catalytic reactions ... 99

Bibliography ... 104
Appendix ... 117

5.4 Activation energies of *p*-nitrophenol reduction ... 124
5.5 List of Tables ... 126
5.6 List of Figures ... 128

Abbreviations ... 133
Publications ... 137
Acknowledgment ... 139
Selbständigkeitserklärung ... 141

1. Introduction

Metallic nanoparticles have been studied intensively within the last decade.[1] This interest originates from the fact that nanomaterials have enhanced catalytic properties compared to the bulk metal. For example, gold was thought to be catalytically inactive for a long period of time. In 1980 Haruta and coworkers reported about the catalytic conversion of oxygen with carbon monoxide at low temperature,[2] and Hutchings and coworkers applied gold catalysts for the hydrochlorination of ethylene to vinyl chloride.[3] Since then many attempts have been made to apply gold nanoparticles as active catalysts.[4-10] Further examples for other catalyzed reactions are C-C coupling reactions [11-13] or hydrogenations,[14, 15] which can be catalyzed by palladium nanoparticles. Platinum nanoparticles are known for hydrogenation reactions.[16, 17] Recently, bimetallic nanoparticles have come into the focus of interest for catalysts due to cooperative effects of both metals.[18-21]

1.1 Stabilization of Metal Nanoparticles

Although metal nanoparticles are catalytically active, one major drawback of these particles is their tendency to agglomerate. To prevent aggregation various approaches are pursued to stabilize nanoparticles. These stabilizers should not interfere with the catalyzed reaction or block the surface of the catalyst. Furthermore, the catalyst should be easily removed from product after the reaction. Homogeneously distributed nanoparticles can be stabilized by electrostatic or steric approaches.[22] The latter can be achieved by the application of dendrimers,[19, 23] micelles,[24] or ligands.[22, 25, 26] Supported nanoparticles can be confined by porous materials,[27-29] polymeric networks,[30] carbon nanotubes,[31-33] or polyelectrolytes.[34-37] Confined nanoparticles benefit from this high colloidal stability and can be separated from the reaction medium on demand. By employing a core-shell structure it is possible to combine the properties of the core e.g. optical,[38] or magnetic properties,[39, 40] with the properties of the shell e.g. stimuli responsiveness,[30] or improved stabilization of nanoparticles. For example, if magnetic particles are used as core, they can be easily removed after the reaction by utilizing their magnetic properties.

The colloidal carrier systems used in this work are spherical polyelectrolyte brushes (SPB). These systems consist of a polystyrene core and a shell of polyelectrolyte chains which are

firmly attached to the core.[41-43] The counter ions are confined within the polyelectrolyte shell, thus the chains are stretched to nearly their full length due to the osmotic pressure built up by the counter ions. Metal ions can be immobilized into such a SPB by ion exchange. In case of a weak polyelectrolyte brush, the thickness of the brush layer decreases due to a partial crosslinking of the polyelectrolytes by the metal ions.[44]

1.2 Synthesis of Nanoparticles

Various synthetic routes for the preparation of monodisperse metal nanoparticles have been developed. The reduction of the metal salt by sodium borohydride is a commonly applied method to produce nanosized particles in the presence of stabilizers like microgels,[45, 46] dendrimers[47] or surfactants.[48, 49] In addition, hydrogen,[25] alcohols[50] and hydrides can be used as reducing agent.[25, 51] Furthermore it is also possible to reduce the metal salt by photons, ultrasound or X-rays.[25, 29, 49, 51, 52]

In this thesis, metal nanoparticles are synthesized by a wet chemical approach with sodium borohydride using spherical polyelectrolyte brushes (SPB) as carrier systems. Figure 1 shows the cryo-TEM micrographs of different metallic nanoparticles of an average size of approximately 2 - 4 nm embedded in SPBs. These metallic nanoparticles were tested by various catalytic reactions such as hydrogenations,[53] Heck and Suzuki cross coupling reactions,[54] and *p*-nitrophenol reduction.[44, 55-57]

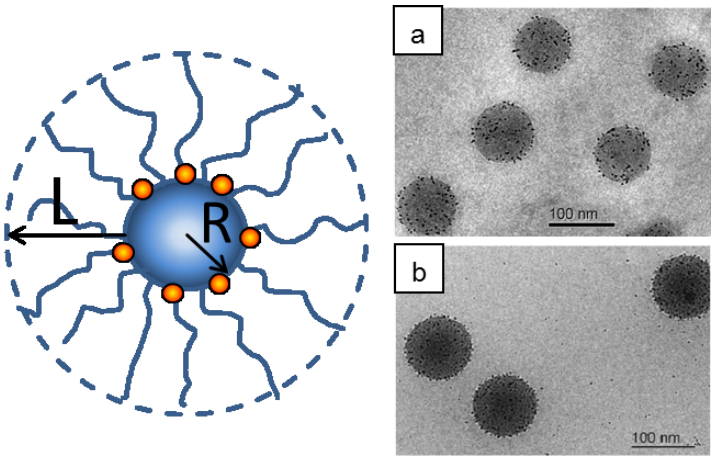

Figure 1: left: Schema of a spherical polyelectrolyte brush system with embedded nanoparticles; right: cryo-TEM micrographs of a) platinum nanoparticles, reprinted with permission from ref [58]. Copyright 2005, American Chemical Society. b) Gold nanoparticles immobilized inside the SPB. Reprinted with permission from ref [44]. Copyright 2007 WILEY-VCH Verlag.

Recently, not only metal particles but also bimetallic particles e.g. Pt-Au were immobilized in the polyelectrolyte layer of SPB.[59] In this case both metal salts acting as precursor for the synthesis were added before the reduction with sodium borohydride to form homogeneous bimetallic nanoparticles. Furthermore, by leaching of the gold with cyanide in Au-Pt particles, faceted Pt nanoparticles can be obtained.[60]

In addition, metal oxide nanoparticles can be synthesized inside the SPB as well. For example, titanium oxide[61] or manganese oxide nanoparticles[62] can be immobilized in these SPBs. Especially for Mn(IV) oxides there exists a wide variety of polymorphs such as α-, β-, γ- and δ-type MnO_2 that differ in their respective linkage of the basic structure, the $[MnO_6]$.[63] For layered manganese oxides, the total surface can be increased by exfoliation, which leads to an enhanced catalytic activity.[64, 65] In the case using SBPs as carriers, platelets of ultrathin K^+-birnessite exhibiting a high surface area can be achieved without an addition of reducing agent.[62] Manganese oxide nanostructures have become of interest as catalysts for oxidation reactions.[66-71] Additionally, these nanoparticles are good catalysts for the catalytic decomposition of hydrogen peroxide [72-74] and therefore for oxidation reactions where H_2O_2 or decomposition intermediates are involved.

Thus, SPB can not only stabilize catalytic active metal nanoparticles, but also oxidation catalysts as manganese oxides. Furthermore, SPBs can be easily prepared from commercially available educts and can be tailored to fit the needs of different catalysts.

1.3 Catalytic Model Reactions

To determine the catalytic activity of different metal nanoparticles or the influence of the carrier system on the catalytic reactions, a model reaction is necessary. This model reaction should proceed without side reactions in the presence of nanoparticles and should not continue without the catalyst. The reaction should be easy to monitor in order to obtain a complete kinetic analysis. Furthermore, the reaction should take place under mild conditions to ascertain that the particles keep their initial structure. It is crucial that no degradation or transformation of the nanoparticles occurs within the measured temperature range. Such a model reaction allows the direct comparison of the catalytic activity of various metallic nanoparticles and a wide range of different carrier systems.

1.3.1 Reduction of *p*-Nitrophenol

Such a model reaction is the reduction of *p*-nitrophenol by sodium borohydride in the presence of metal nanoparticles (Scheme 1). This reaction has attracted much attention over the last years. In 2002 Pradhan *et al.*[75] and Esumi *et al.*[76] reported the catalytic activity of their metallic nanoparticles with this reaction.

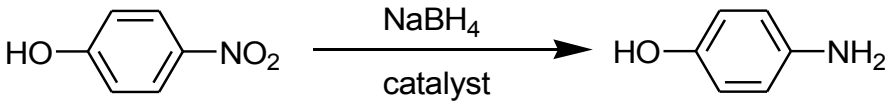

Scheme 1: Reaction scheme of the conversion of p-nitrophenol to p-aminophenol by sodium borohydride

Since then, this reaction has been used as a benchmark reaction for the activity of nanoparticles. This reaction is easily followed by UV-vis spectroscopy due to the fact that *p*-nitrophenol shows a distinctive absorption peak at 400 nm in alkaline solution. The product, *p*-aminophenol, exhibits a weak absorption peak at around 300 nm. In Figure 2 the UV-vis spectra of the reaction is shown. Several isosbestic points confirm that there are no side reactions and that only one product is formed.

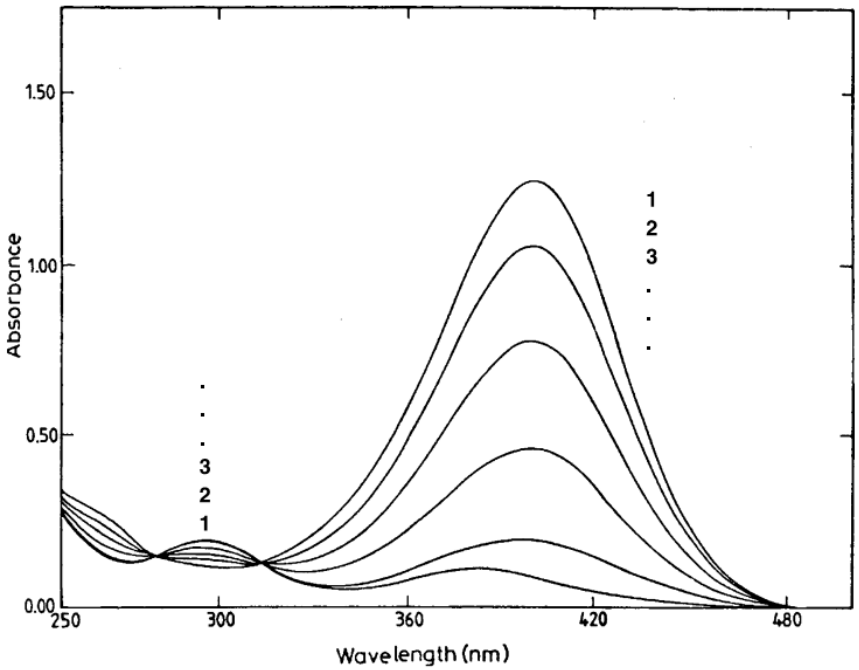

Figure 2: UV-vis spectra of the reduction of p-nitrophenol by sodium borohydride with silver nanoparticles. Reprinted from ref [75]. Copyright 2001, with permission from Elsevier.

Without the catalyst the reduction of *p*-nitrophenol does not proceed.[77] From the vanishing intensity of the absorption at 400 nm, the reaction rate can be calculated by a pseudo first order reaction, if an excess of sodium borohydride is used.[78, 79] This rate constant can be further analyzed to gain the activation energies of the reaction. Even though this reaction is often applied to verify and to compare the activity of different metal nanoparticles, the reaction mechanism has never been analyzed in detail. Zhang *et al.*[80] suggested that the borohydride transfers a surface hydrogen species which reacts with the *p*-nitrophenol to produce *p*-aminophenol, while Khalavka *et al.*[81] supposed that "hydrogen" adsorbs onto the surface, which reacts with the *p*-nitrophenol from solution. But neither of the authors provides any evidence for this suggestion. Thus a detailed mechanistic study of this model reaction is essential for a full understanding of the catalysis.

1.3.2 Oxidation of Flavonols

In addition to reductions, oxidation reactions can be catalyzed by nanoparticles. The oxidation of flavonol dyes, for example, can be applied to prove the catalytic activity of bleaching catalysts.[82] These compounds are present in tea, fruits and vegetables. Furthermore, the chromophores of these polyphenols are targets in the bleaching of laundry. Thus, this group of organic dyes can be used as a simple model of a bleaching stain.[83] As oxidizing agent for bleaching applications, H_2O_2 is most commonly applied in alkaline environments.[82]

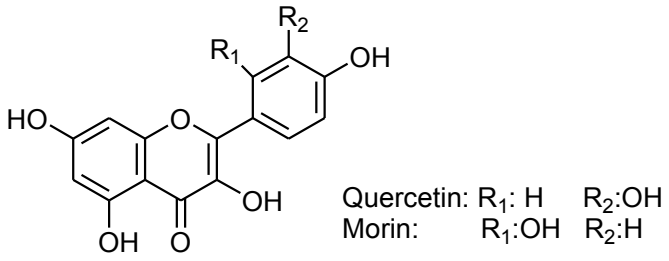

Scheme 2: Chemical formula of the flavonols quercetin and morin.

One of the flavonols that can be used as model for bleaching stains, is morin. Its two main oxidation products are 2,4-dihydroxybenzoic acid and 2,4,6-trihydroxybenzoic acid.[84, 85] The oxidation pathways of morin are not known as precisely as the oxidation pathways of quercetin,[86-89] which is used more often for oxidation studies. Unlike quercetin, morin

cannot dimerize due to the OH group R_1 in ortho-position (see Scheme 2). However, morin is better suited for catalytic oxidation studies as it shows a higher stability in alkaline media compared to quercetin.[90] The reaction mechanism of the oxidation of morin by manganese oxide catalysts is not determined yet. Thus, analyzing this mechanism may lead to an improvement of stable, low temperature bleaching catalysts, which may further increase the bleaching efficiency in laundry applications.

1.4 Objectives of this Thesis

The foremost objective of this thesis is the detailed study of the reaction mechanism of two model reactions: namely, the reduction of *p*-nitrophenol and the oxidation of morin. For both catalyzed reactions the mechanism on the surface of the catalyst is not known. In case of the *p*-nitrophenol reduction even two opposing mechanisms are postulated in the literature. By determination of the reaction mechanism, the catalysts could be altered to achieve better catalytic output. In case of the reduction of *p*-nitrophenol, noble metals (gold or platinum nanoparticles) are used as catalysts, whereas for the oxidation of morin manganese oxide nanoparticles are employed. For a better comparison, the same type of carrier system, namely, spherical polyelectrolyte brushes are applied.

Gold and platinum nanoparticles, embedded in the spherical polyelectrolyte brushes, are obtained by the reduction of the respective metal salt with sodium borohydride. The manganese oxide nanoparticles are obtained by reducing potassium permanganate inside the spherical polyelectrolyte brush.

In case of the reduction of *p*-nitrophenol by sodium borohydride on gold and platinum nanoparticles a systematic study of the reaction mechanism is performed. Furthermore, the temperature dependence of this reaction is studied. Additionally, the induction period of the reaction is examined in detail to reveal the origin of this frequently reported phenomenon.

As second model reaction, the oxidation of morin by H_2O_2 is analyzed in detail. A deeper understanding of the initial reaction step is attained by a detailed analysis of the reaction in dependence of the temperature. By employing the same analytical methods as in the previous study of *p*-nitrophenol the underlying reaction mechanism of this oxidation reaction is revealed.

2. Fundamentals

2.1 Polymer brushes

Anchoring one end of polymer chains to a surface is called grafting. If the number of chains per surface area (grafting density) is high, the chains are stretched to avoid segment-segment interactions within the system. Such a system is called a polymeric brush. However, this stretching reduces the entropy of the system. Therefore the brush height will be the result of equilibrating the stretching forces and the retraction due to entropy. If the grafting density is low, the polymer chains may behave like single chains. In this case other structures like "mushroom" (if the polymers have a weak or even repulsive interaction with the surface) or "pancake" (a strong interaction between surface and polymer chains) can be obtained.[91]

If these brushes bear charges, the term polyelectrolyte brushes (PE) is used. This is shown schematically in Scheme 3. If the PE is attached to a spherical particle, it is called a spherical polyelectrolyte brush (SPB). In this thesis SPB are used as carrier systems. The majority of the counter ions are confined within the brush layer.[57, 92] These counter ions build up a high osmotic pressure inside the brush, which leads to a stretching of the polyelectrolyte chains.

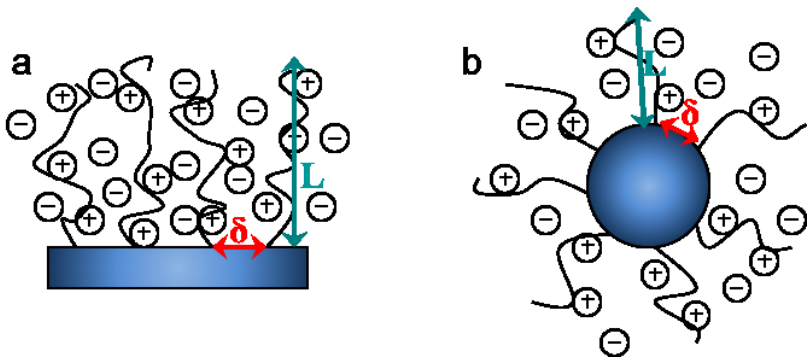

Scheme 3: Planar polyelectrolyte brushes (a) and spherical polyelectrolyte brushes (b). The thickness of the polyelectrolyte layer is marked with L and the grafting density by δ.

SPBs can be divided in two classes: annealed and quenched brushes. The overall charge of annealed polyelectrolytes is dependent on the pH-value of the solution. Examples are poly(acrylic acid) (PAA) or poly(2-aminoethyl methacrylate hydrochloride) (PAEMH). This is illustrated in Figure 3a where a PAA brush system from Ref [41] is shown with different

pH-values. The brush thickness *L* rises from around 20 nm at pH 2 to more than 200 nm at pH 8 in a 0.1 mM KCl solution. PAA becomes more charged at higher pH-values and therefore the polyelectrolyte chains are stretched due to the osmotic pressure and charge repulsion. In contrast to that, quenched polyelectrolytes have a permanent charge. Examples are poly(styrene sulfonate) (PSS) and poly(2-trimethylaminoethyl methacrylate chloride) (PTMAEMAC). The quenched brush system in Figure 3b shows no dependence on the pH-value but only on the ionic strength of the system. [41, 57]

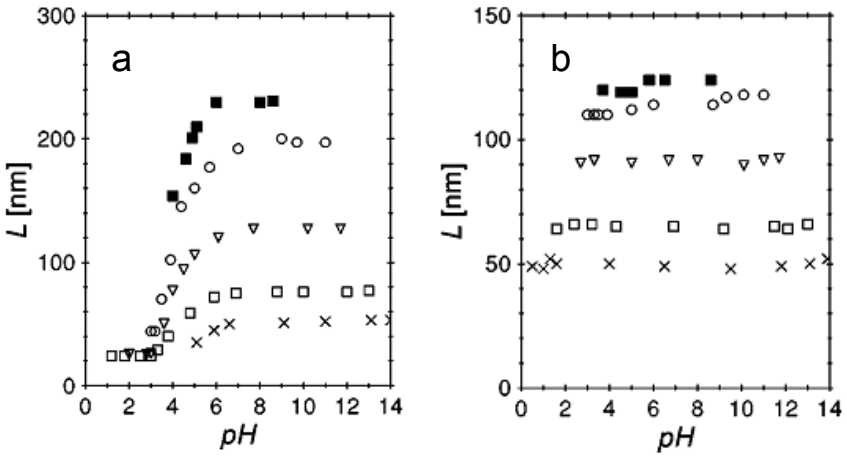

Figure 3: a) Dependence of brush thickness L on pH for annealed PAA brush. The parameter of the data is the ionic strength in the solution, which was adjusted by adding a KCl solution: crosses, 1M; open squares, 0.1M; triangles, 0.01M; open circles, 0.001M; filled squares, 0.0001M. b) Dependence of brush thickness L on pH in the solution for a quenched PSS brush. The parameter of the data is the ionic strength in the solution, which was adjusted by adding KCl. Crosses, 1M; open squares, 0.1M; triangles, 0.01M; open circles, 0.001M; filled squares, 0.0001M. Reprinted figures with permission from ref [41]. Copyright 2001 by the American Physical Society. (http://link.aps.org/doi/10.1103/PhysRevE.64.051406)

2.1.1 Spherical Polyelectrolyte Brushes (SPB)

The SPB are synthesized in a two-step polymerization. First the polystyrene core is synthesized with a thin layer of photo-initiator on the surface of the particle by emulsion polymerization. After cleaning of these core particles a suitable electrolyte monomer is chosen. The polyelectrolyte chains are grafted onto the core via photo emulsion polymerization.[41-43] In Scheme 4 different types of polyelectrolytes, which can be grafted on the poly(styrene) core of SPBs, are shown.

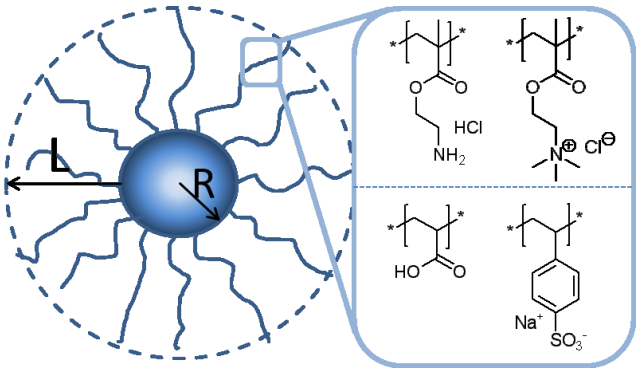

Scheme 4: Scheme of a spherical polyelectrolyte brush. The particles consist of a polystyrene core and a polyelectrolyte shell. The polyelectrolytes applied in this work are shown in the upper panel: the cationic polyelectrolytes (poly(2-aminoethyl methacrylate hydrochloride) PAEMH, poly(2-trimethylammonioethyl methacrylate chloride) PTMAEMAC), and anionic polyelectrolytes are shown in the lower panel (poly(acrylic acid) PAA, poly(styrene sulfonate) PSS).

By adding salt to the SPB, the brush collapses, which can be monitored by DLS,[93] cryo-TEM,[94] or SAXS.[95, 96] Adding multivalent counter ions leads to a more pronounced collapse because the charges of the polyelectrolyte chains are counter balanced by less counter ions.[41]

2.1.2 Synthesis of Nanoparticles inside Spherical Polyelectrolyte Brushes

Metal nanoparticles within the SPB are synthesized by a wet chemical approach as visualized in Scheme 5. Metal salt is added to a solution of the SPB. The metal salt will be confined inside the SBP by ion exchange. Metal ions which are not kept within the SPB can be washed off by an ultra-filtration step. Thereafter, sodium borohydride as a strong reducing agent is introduced and the metal salt is reduced to metal nanoparticles, which are embedded in the brush layer. In the end, these composite particles are cleaned once more via ultra-filtration.

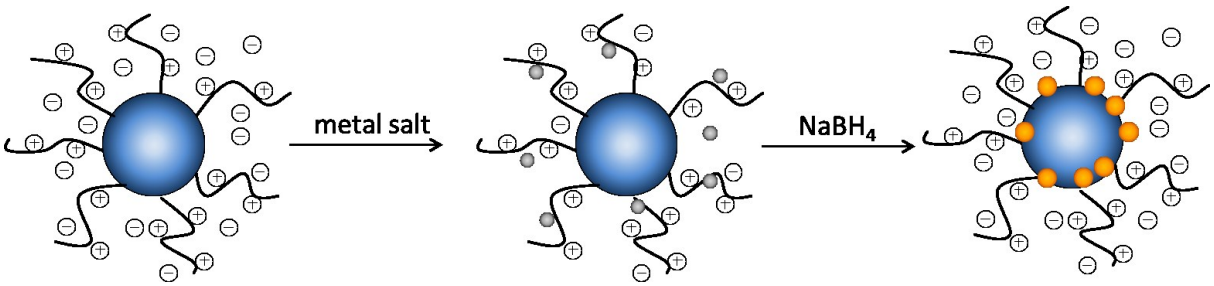

Scheme 5: Synthesis of metal nanoparticles inside the brush layer of SPB by sodium borohydride. First the metal salt is added to the SPB solution. Through an ion exchange the metal ions are confined within the brush layer. Unbound metal salt can be washed off by ultra-filtration. In a next step the metal salt is reduced to the metallic nanoparticles by adding sodium borohydride as reducing agent.

For the annealed brush the brush length will be reduced to a certain extent by adding the metal salt.[44] The thickness of the brush is reduced even further after the reduction of the metal salt to nanoparticles. This may be due to the cross-linking of the polyelectrolyte chains caused by the multiple negative surface charges of the nanoparticles. In case of the complete dissolving of the gold nanoparticles, the original length of the polyelectrolyte brush will be obtained again, which demonstrates that the brush is not chemically affected by the synthesis of the nanoparticles (NP). For quenched brushes, a constant layer thickness was observed during the synthesis of the nanoparticles. In Figure 4, cryo-TEM micrographs of different metallic nanoparticles inside SPB, are shown. The imaged nanoparticles have an average size of around 2 – 4 nm. The polyelectrolytes cannot be seen in the micrographs due to their low contrast.

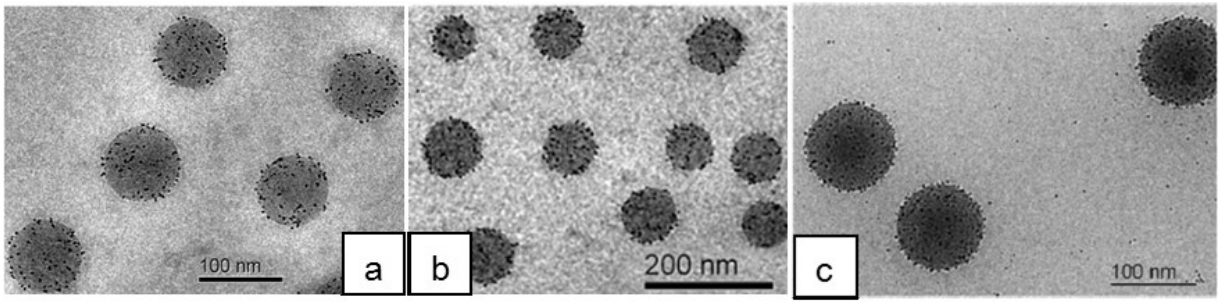

Figure 4: Cryo-transmission electron microscopy of nanoparticles a) platinum nanoparticles, reprinted with permission from ref [58]. Copyright 2005 American Chemical Society. b) Palladium nanoparticles, reprinted with permission from ref [56]. Copyright 2007 American Chemical Society. c) Gold nanoparticles. Reprinted with permission from ref [44]. Copyright 2007 WILEY-VCH Verlag.

Additionally, bimetallic particles e.g. Pt-Au could be immobilized in spherical polyelectrolyte brushes.[59] In this case both metal precursor salts are introduced before the

reduction of the metal salts with the sodium borohydride is performed. With this method, homogeneous bimetallic metal nanoparticles can be achieved. Faceted Pt nanoparticles can be obtained by leaching of the gold with cyanide from these Au-Pt nanoparticles.[60]

Moreover, metal oxide nanoparticles can be immobilized in suitable brush systems. In case of titanium dioxide, anantase nanoparticles with a size of approximately 10 nm can be synthesized within the SPB.[61] These composite particles can then further stabilize noble metal nanoparticles.[97] Another approach is the synthesis of manganese oxide nanoparticles inside the brush system.[62] The SPB used here consists of a strong polyelectrolyte brush (PTMAEMAC) and a polystyrene (PS) core. $KMnO_4$ is added to this system and incorporated into the brush by an ion exchange. This precursor is reduced in situ inside the brush without further reducing agent. Thus the size of the nanoparticles is limited by the brush extension.[62] Here, ultrathin manganese oxide platelets were obtained. Studies with cryo-TEM, powder diffraction, and energy dispersive X-ray spectroscopy proved that these nanoparticles are of c* disordered K^+-birnessite structure. This modification of MnO_2 consists of lamellas of edge-sharing manganese oxide octahedras. Potassium ions balanced most of the charges of these thin nanostructures. Strong electrostatic interactions of the manganese oxide platelets and the polyelectrolyte chains lead to an excellent colloidal stability. Measuring the nanoparticles in cryo-TEM, the length of the nanoparticles is 20 nm and the breadth approximately 1.6 nm.[62] The fine nanostructure will collapse in case of "normal" TEM micrographs due to the drying process. Figure 5 show cryo-TEM micrographs of these manganese oxide nanoparticles immobilized inside the polyelectrolyte shell of the SPB.

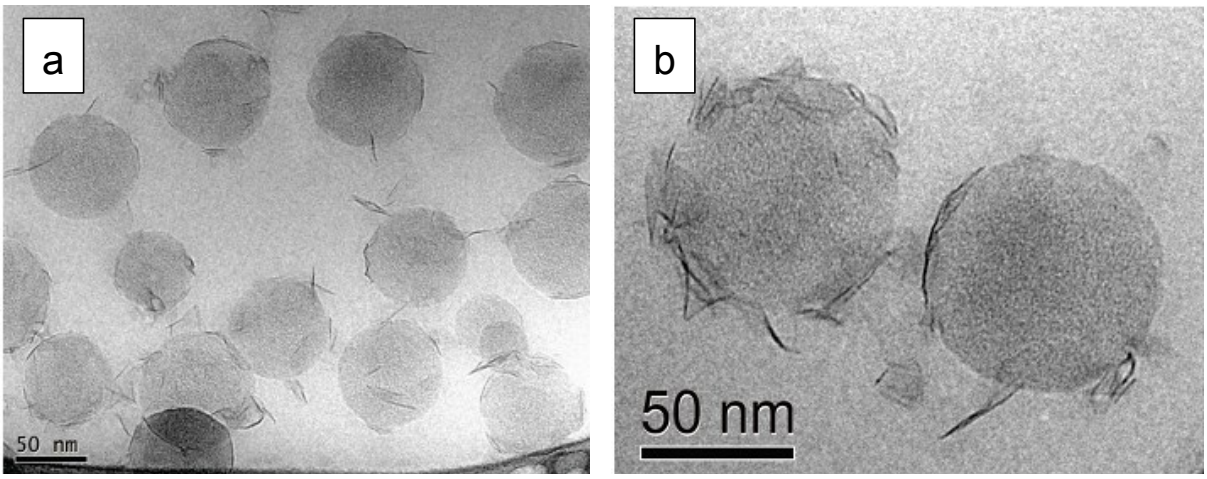

Figure 5: a) Cryo-TEM of the composite system SPB-MnO2 and b) the MnOx nanoparticles in a higher magnification. Reprinted with permission from ref [62]. Copyright 2010 American Chemical Society.

2.2 Heterogeneous catalysis

In contrast to homogeneous catalysts, the heterogeneous catalysts are in a different phase as the reaction mixture, e.g. a solid catalyst and a fluid or gaseous reaction mixture. Thus, to effectively catalyze the reaction the reactant has to adsorb onto the surface. This adsorption processes can be described by adsorption isotherms as Langmuir, Freundlich, or BET isotherms.

2.2.1 Adsorption Isotherms

2.2.1.1 Adsorption Process

The first step in the heterogeneous catalysis is the adsorption. The rate of adsorption r_{ad} is proportional to the collision frequency F of the adsorbate with the surface, and the probability of the adsorption s:[98]

$$r_{\mathrm{ad}} \propto F \cdot s \tag{2.1}$$

The collision rate F is proportional to c, the concentration of the molecules and v, their velocity. The mean velocity of the molecules is $(8 \cdot k_B \cdot T/\pi \cdot m)^{1/2}$ where k_B is the Boltzman's constant, T the absolute temperature, and m the mass of the molecule. By considering the ideal gas law the collision rate can be rewritten as:[98]

$$F = \frac{p}{(2 \cdot \pi \cdot m \cdot k_{\mathrm{B}} \cdot T)^{\frac{1}{2}}} \tag{2.2}$$

In case of an activated adsorption, the sticking probability s is dependent on the probability of the collision with a free adsorption site $f(\theta)$, with θ being the surface coverage, σ represents the probability that the molecule has the right adsorption energy E_{ad} for the adsorption:[98]

$$s = \sigma \cdot f(\theta) \cdot e^{-E_{\mathrm{ad}}/RT} \tag{2.3}$$

The adsorption rate can therefore be rewritten as:[98]

$$r_{\mathrm{ad}} = \frac{p \cdot \sigma \cdot f(\theta)}{(2 \cdot \pi \cdot m \cdot k_{\mathrm{B}} \cdot T)^{\frac{1}{2}}} \cdot e^{-E_{\mathrm{ad}}/RT} \tag{2.4}$$

2.2.1.2 Desorption Process

In contrary to the adsorption, the desorption is always an activated process. The rate of desorption r_{des} can be written as:[98]

$$r_{\mathrm{des}} = k_{\mathrm{des}} \cdot f'(\theta) \cdot e^{-E_{\mathrm{des}}/RT} \qquad 2.5$$

where k_{des} is the rate of desorption, $f'(\theta)$ the occupied sites on the surface, and E_{des} the activation energy of desorption. $E_{\mathrm{des}} = Q_{\mathrm{ad}} + E_{\mathrm{ad}}$. This energy is equal to the sum of the heat of adsorption, Q_{ad}, and the activation energy of the adsorption E_{ad}. On a uniform surface both, the rate constant k_{des} as well as the energy of desorption E_{des} are dependent on the surface coverage θ.[98]

$$r_{\mathrm{des}} = k_{\mathrm{des}}(\theta) \cdot f'(\theta) \cdot e^{-E_{\mathrm{des}}(\theta)/RT} \qquad 2.6$$

2.2.1.3 Langmuir Isotherm

One of the fundamental adsorption isotherms is the Langmuir adsorption isotherm. Here it is assumed that adsorption and desorption is in an equilibrium ($r_{\mathrm{ad}} = r_{\mathrm{des}}$). The adsorption on uniform, ideal surfaces can be described with a Langmuir isotherm if the following assumptions apply:

- all adsorption sites are equal,
- the adsorption can only occur at free adsorption sites,
- there can be only one single occupation of a free adsorption sites, therefore only a monolayer adsorption is possible,
- the adsorption is not dependent on the coverage of the surface and no interactions of the adsorbed molecules occur.

A single, reversible adsorption can be described with: * + $A_{(g)}$ $\rightleftharpoons$ A*, where * is a vacant adsorption site on the surface, $A_{(g)}$ is a molecule in the gas phase, and A* a adsorbed molecule. At equilibrium conditions, the adsorption and desorption process is equal. Therefore setting eq. 2.4 and eq. 2.6 equal and rearranging, the following equation can be derived:[98]

$$p = \frac{(2 \cdot \pi \cdot m \cdot k_B \cdot T)^{1/2} \cdot k_{des}}{\sigma} \cdot \frac{f'(\theta)}{f(\theta)} \cdot e^{\left((E_{des} - E_{ad})/RT\right)} = \frac{1}{K} \cdot \frac{f'(\theta)}{f(\theta)} \qquad 2.7$$

With this equation different adsorption and desorption processes can be described when appropriate functions for *f(θ)* and *f'(θ)* are found. This equation implies that the adsorption constant *K* is only dependent on the temperature.

By considering the adsorption on a single adsorption site the probability of a free adsorption site can be described as *f(θ) = (1-θ)* and for the occupied adsorption site as *f'(θ) = θ*. Therefore, the pressure *p* can be rewritten as:[98]

$$p = \frac{1}{K} \cdot \frac{\theta}{(1-\theta)} \qquad 2.8$$

Combination of eq. 2.7 and the pressure leads to the Langmuir isotherm:[98]

$$\theta = \frac{K \cdot p}{(1 + K \cdot p)} = \frac{K' \cdot [A]}{(1 + K' \cdot [A])} \qquad 2.9$$

2.2.1.4 Competitive Adsorption

In case of adsorption of more than one species of molecules, the Langmuir isotherm must be modified. If species A and B can adsorb on the same adsorption sites S and the rate determining step (rds) is the surface reaction, the following shall apply:

$$A_{(g)} \rightleftharpoons A^*$$

$$B_{(g)} \rightleftharpoons B^*$$

This leads to:

$$1 = \theta_A + \theta_B + \theta_f \qquad 2.10$$

where θ_f is the concentration of the free adsorption sites , θ_A the concentration of the sites covered with A, and θ_B the concentration of sites covered with B on the surface.[98] Therefore the adsorption constants K_A und K_B can be rewritten as follows:

$$K_A = \frac{\theta_A}{p_A \cdot \theta_f} = \frac{\theta_A}{p_A (1 - \theta_A - \theta_B)} \qquad 2.11$$

So

$$K_B = \frac{\theta_B}{p_B \cdot \theta_f} = \frac{\theta_B}{p_B(1-\theta_A-\theta_B)} \quad 2.12$$

lving

these equations to the surface coverage θ_A and θ_B leads to:[98]

$$\theta_A = \frac{K_A \cdot p_A}{(1 + K_A \cdot p_A + K_B \cdot p_B)} \quad 2.13$$

$$\theta_B = \frac{K_B \cdot p_B}{(1 + K_A \cdot p_A + K_B \cdot p_B)} \quad 2.14$$

For a non-dissociative adsorption the surface coverage of a species x can be described as:

$$\theta_x = \frac{K_x \cdot p_x}{1 + \sum_{i=1}^{n} K_i \cdot p_i} \quad 2.15$$

2.2.1.5 Freundlich Isotherm

The Freundlich isotherm is a strictly empirical model. It takes into account that at higher coverages the adsorption slows down and a complete coverage is not reached.[99] The coverage is proportional to a power law of the pressure, thus the Freundlich isotherm is similar to the Langmuir isotherm at moderate coverages.[99]

$$\theta = K_i \cdot p_i^{\frac{1}{m}} \quad 2.16$$

where *m* is the Freundlich exponent.

2.2.1.6 Langmuir-Freundlich Isotherm or Sips Isotherm

The Langmuir-Freundlich ansatz combines the Langmuir and the Freundlich adsorption isotherms. This ansatz was developed by Sips in 1984.[100] This equation (2.17) is similar to the Langmuir isotherm and differs only in the factor *m*. In case of *m* = 1 the Langmuir-Freundlich is reduced to the Langmuir ansatz. At low concentrations it reduces to the

Freundlich isotherm. The parameter *m* is a measure for the "non-ideal" of the system, mainly due to the heterogeneity of the sorbent.

$$\theta_i = \frac{(K_i \cdot p_i)^{m_i}}{1+(K_i \cdot p_i)^{m_i}} \qquad 2.17$$

This adsorption isotherm describes a monolayer adsorption showing a quasi-Gaussian distribution of adsorption energies.[101, 102] For a multi component system equation 2.17 can be expanded to:[103]

$$\theta_x = \frac{(K_x \cdot p_x)^{m_x}}{1+\sum_{i=1}^{n}(K_i \cdot p_i)^{m_i}} \qquad 2.18$$

2.2.2 Eley-Rideal Mechanism

These adsorption isotherms can be applied for modeling the reaction on the surface of the catalyst. In case of an Eley-Rideal mechanism, only one of the reactants, e.g. reactant A adsorbs (ad) on the surface of the catalyst. Reactant B is still in the surrounding media (g). The adsorbed and the unbound species react to the product C when both collide. This reaction is the rate determining step. Product C then desorbs from the catalyst surface.

$$A_g + * \longrightarrow A_{ad}$$
$$A_{ad} + B_g \longrightarrow C_{ad}$$
$$C_{ad} \longrightarrow C_g + *$$

The adsorption is modeled in terms of a Langmuir isotherm (eq. 2.15) where the surface coverage of the components *i* is dependent on the adsorption constant and the concentration. The reaction rate is then dependents on the concentration, the surface coverage and the available surface:

$$r = S \cdot k \cdot \theta_A \cdot [B] \qquad 2.19$$

where r is the reaction rate; S the surface of the nanoparticles. The whole surface is used for the modeling, as the number of active sites on surface cannot be determined accurately; k the intrinsic rate constant; θ_i surface coverage of i; and K_i: adsorption constant of i.

Inserting the coverage from the Langmuir isotherm in equation 2.15 the following reaction rate is obtained:

$$r = \frac{S \cdot k \cdot K_A \cdot [A] \cdot [B]}{1 + K_A \cdot [A]} \qquad 2.20$$

Alternatively the species B can also adsorb onto the surface. In this case the adsorbed B is seen as an inactive species in the reaction. The influence of the concentration of B shows a linear dependency. The reaction rate r is therefore dependent on the concentration of A as shown in Figure 6.

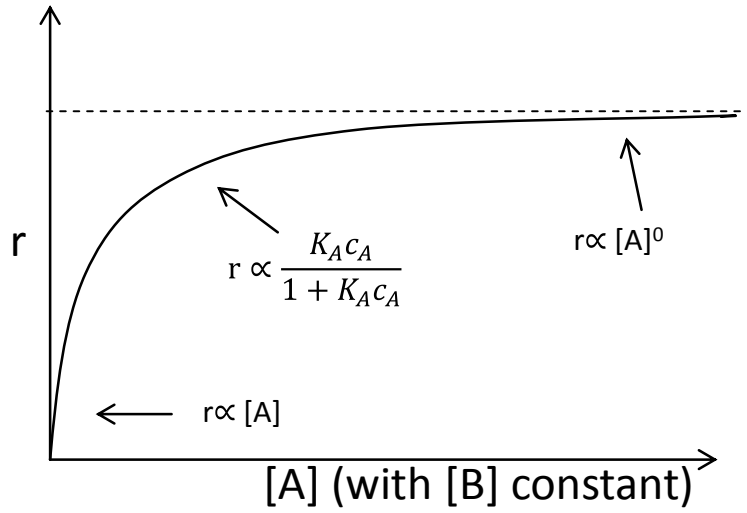

Figure 6: Reaction scheme of a Eley-Rideal mechanism for a varying the concentrations of A by a constant concentration of B.

2.2.3 Langmuir-Hinshelwood Mechanism

In comparison with the Eley-Rideal model, in the Langmuir-Hinshelwood (LH) model both reactants adsorb. The reaction steps are the following:

$$A_g + * \longrightarrow A_{ad}$$

$$B_g + * \longrightarrow B_{ad}$$

$$A_{ad} + B_{ad} \longrightarrow C_{ad}$$

$$C_{ad} \longrightarrow C_g + *$$

The rate determining step is the surface supported reaction. The product then desorbs afterwards. Both reactants compete for active sites. Thus, if one reactant has a higher affinity toward the surface, an increase in this concentration leads to a decreasing reaction rate. On the other hand, a decrease of this concentration might lead to an increasing rate, if the ratio of both reactants is not in the optimum. If a back reaction does not occur, the rate is given by:[98]

$$r = S \cdot k \cdot \theta_A \cdot \theta_B \qquad 2.21$$

The rate r is therefore proportional to the intrinsic rate k, and the surface coverages of A and B. After insertion of the coverages from the Langmuir isotherm the rate can be rewritten as:

$$r = \frac{k \cdot S \cdot K_A \cdot [A] \cdot K_B \cdot [B]}{(1 + K_A \cdot [A] + K_B \cdot [B])^2} \qquad 2.22$$

This r is visualized in Figure 7 for a constant concentration of B. For a high adsorption constant of A, the rate increases at very small concentrations of A, then reaching a narrow maximum before the rate drops dramatically and levels off in a plateau phase for high concentrations of A. In contrast to this, for small adsorption constants of A, a broader maximum is visible and the decrease of the rate at even higher concentrations is less pronounced.

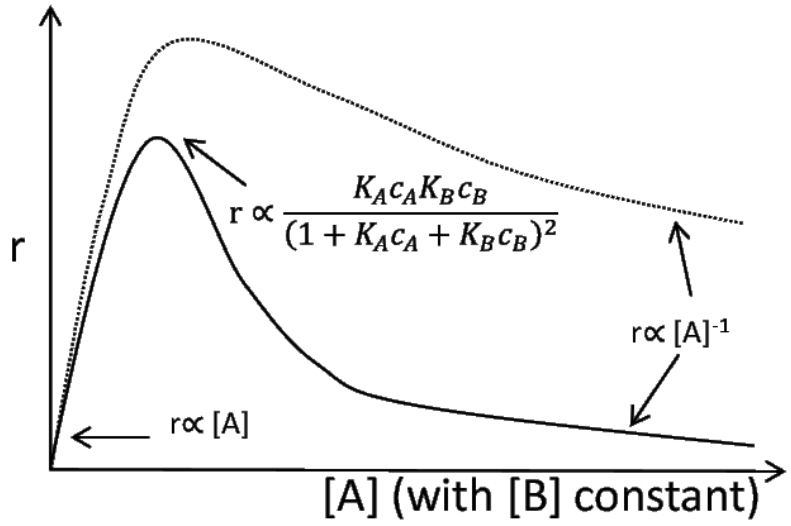

Figure 7:Dependence of the reaction rate of the reaction on variation of concentration A at a constant concentration B according to Ref [98].

If one of the reactants is in great excess available (e.g. [B]), the rate for the actual experiments can be calculated with a pseudo first order reaction $\left(\frac{d[A]}{dt} = -k_{app}\cdot[A]\right)$, inserting this into eq. 2.22 leads to:

$$r = \frac{k\cdot S\cdot K_A\cdot[A]\cdot K_B\cdot[B]}{(1+K_A\cdot[A]+K_B\cdot[B])^2} = k_{app}[A] \qquad 2.23$$

where k_{app} is the apparent rate constant from a pseudo first order reaction. Rearranging to the apparent reaction rate k_{app} leads to equation 2.24:

$$k_{app} = \frac{k\cdot S\cdot K_A\cdot K_B\cdot[B]}{(1+K_A\cdot[A]+K_B\cdot[B])^2} \qquad 2.24$$

2.2.4 Rate controlled or diffusion controlled

Both reaction models use the assumption that the diffusion is rather fast in comparison to the reaction. One possibility to estimate if the reaction is diffusion controlled, or if the reaction is controlled by the chemical reaction on the surface, is the so-called second Damköhler number (*DaII*): [98]

$$DaII = \frac{kc^{n-1}}{\beta a} \qquad 2.25$$

where k is the reaction rate constant, c is the concentration, n is the reaction order, which is n = 1 by a first order reaction, β is the mass transport coefficient, and a the total area of the interface. Hence, by the Damköhler number II, the ratio between chemical conversion and transport by diffusion is compared. Values above unity ($DaII >> 1$) designate a diffusion controlled reaction, because the reaction is faster than the diffusion of the educts. *DaII* numbers below unity ($DaII << 1$) point to a reaction rate controlled system, where the diffusion is much faster compared to the reaction rate.

2.2.5 Surface Reconstruction and Restructuring

The adsorption of the educts on solid surfaces during catalysis can lead to a restructuring process of this surface. One example is the CO oxidation by platinum catalysts. In this special case the reaction is oscillating. This process can be followed via photoemission electron microscopy (PEEM). Here ionizing radiation results in emitted electrons, which are detected. The emitted electron signal exhibits oscillatory characteristics, which represents the oscillatory behavior of the reaction.

The reason for this oscillating reaction is the reconstruction of the platinum surface.[104] A schematic overview of the different non-reconstructed surfaces and the respective restructured surfaces are shown in Figure 8. The clean (100) surface of platinum reconstructs to a hexagonal over-layer, whereas the (110) surface reconstructs to a missing-row structure. The (111) surface however does not reconstruct at all. The reconstruction is caused by a relaxation of the topmost atom layer which can result in a complete different structure of the surface atoms in comparison with the bulk structure.[105] The reconstructed surface of Pt, for the (100) as well as the (110) can be lifted by the adsorption of certain adsorbates as CO, or NO. The adsorbate induced phase transition is also known as surface restructuring and is controlled by a critical adsorbate coverage.[106]

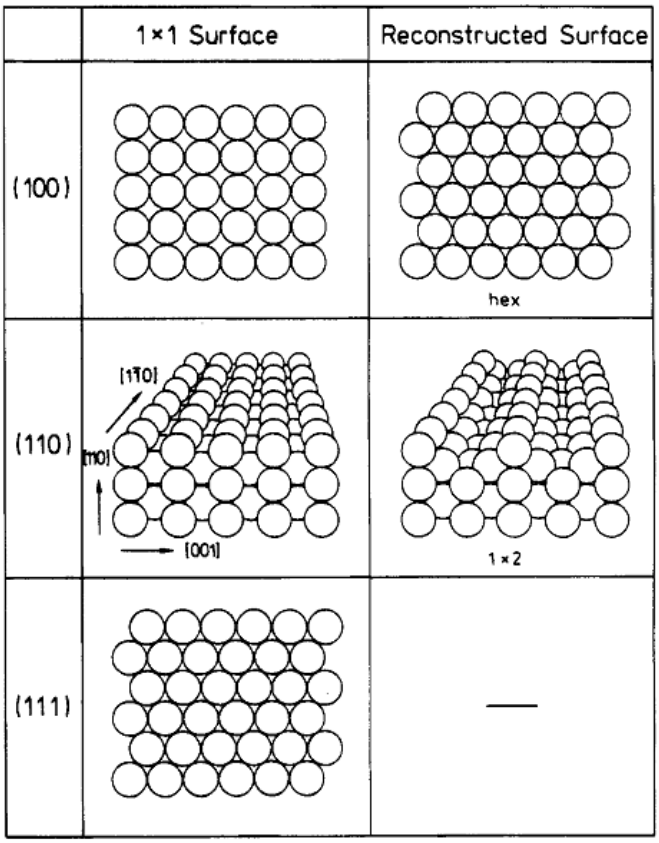

Figure 8: Pure and reconstructed surfaces of the three low index planes of platinum. The 1x1 surface of the Pt(100) is reconstructed to a hexagonal pattern, the Pt (110) surface to a missing row structure. Reprinted with permission from ref [106]. Copyright 1995 American Chemical Society.

These different over-structures on the surface can be directly correlated with the oscillatory kinetics. This phenomenon is caused by the different sticking probability of oxygen. It is very low at the reconstructed surface (see Figure 9 right side). CO adsorption leads to a local lifting of the reconstruction. Therefore, the sticking coefficient for oxygen is much higher on this bulk-like structured surface as can be seen in Figure 9 on the left side.

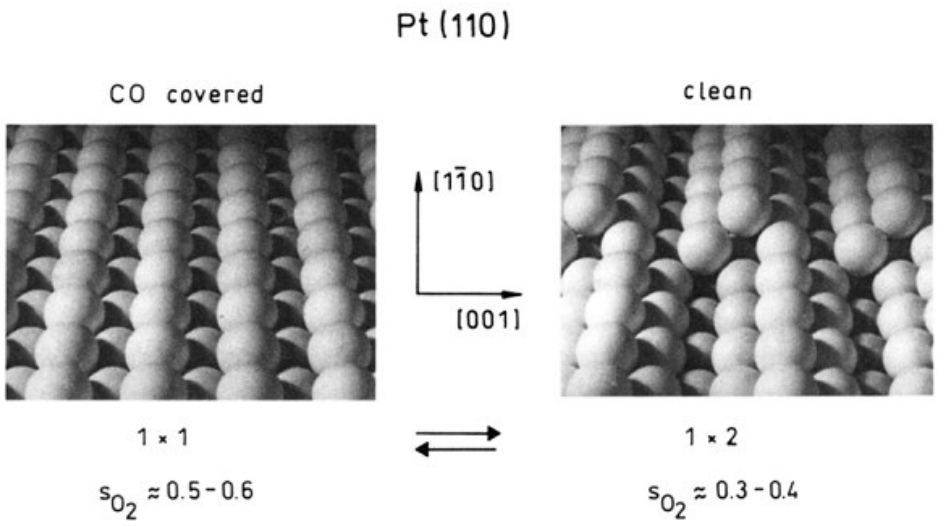

Figure 9: Model of the CO-induced 1 x 1 and 1 x 2 surface phase transition of Pt (110). On the left side is the restructured of the platinum surface by adsorption of CO, on the right side is the reconstructed surface of the Pt (110) shown. The different sticking coefficients of oxygen, s_{o2}, of the two phases are responsible for rate oscillations during the catalytic CO oxidation. The model also demonstrates how the mass transport of Pt atoms creates an atomic step on the surface. Reprinted with permission from ref [106].Copyright 1995 American Chemical Society.

Therefore, the reaction propagates if oxygen can adsorb onto this surface, but this requires two free neighboring adsorption sites due to dissociation of the O_2 molecule. Once the surface is depleted of CO molecules after their oxidation, the reactivity decreases again, because the surface reconstructs without adsorbed CO. On a Pt(110) surface the oscillation of the reaction will form spirals, standing waves and rings depending on the reaction parameters. This is caused by the small difference in the sticking coefficient of oxygen, which leads to an oscillating surface structure of the Pt-surface depending on the state of the reaction cycle. In detail these states are: adsorption of CO, restructuring, O_2 adsorption, oxidation, and reconstruction. The oxygen sticking coefficient differs in the factor of two between the reconstructed surface and the restructured surface in case of Pt(110).[107] On Pt(100) however, the sticking coefficient differs drastically between the restructured 1 x 1 surface ($s_{o2} = 0.3$) and the reconstructed hexagonal phase (s_{o2} in the order of 10^{-4} - 10^{-3}).[106]

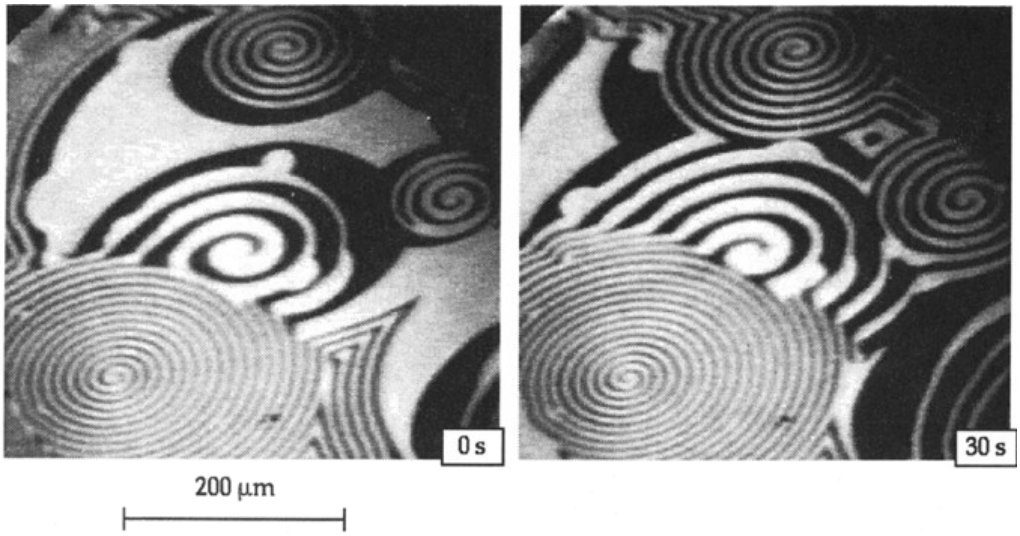

Figure 10: Oscillating waves on a Pt(110) surface during the oxidation of CO. The PEEM (photoemission electron microscope) images demonstrating the temporal evolution of spirals with strongly different rotation periods and wavelengths: T = 448 K, p_{co} = 4.3 x 10^{-5} mbar, and p_{o2} = 4 x 10^{-4} mbar. The spiral with the largest wavelength rotates around a core of 25 x 14 pm^2, while the size of the core region is only 5 x 3 $pm^2$for the fast rotating spiral visible in the foreground. Reprinted with permission from ref [106].Copyright 1995 American Chemical Society.

Furthermore, the group of King could show by analyzing the surface restructuring of the adsorption of hydrogen [108] or CO[109] on platinum that the rate of the surface reconstruction follows a power rate law. Later, the group of van Beurden verified this finding by computer simulations.[110, 111]

3. Results and Discussion

3.1 Reduction of *p*-Nitrophenol – Literature Survey

As already mentioned in the introduction, the reduction of *p*-nitrophenol is a common reaction to test the catalytic activity of metallic nanoparticles. It was used quite frequently to demonstrate the activity of various metallic nanoparticles as Au (relevant data in Table 23, in Appendix), Ag (Appendix, Table 24), Pt (Appendix, Table 25), Pd (Appendix, Table 26), or bimetallic nanoparticles (Appendix, Table 27) on different carrier systems, e.g. dendrimers, [76, 112-114] hydrogels, [56, 115-121] micellar systems, [122-125] or polymer brushes.[58, 126-129] A direct comparison of the different systems is difficult because in these studies different concentrations of educts, temperatures, and normalizations have been applied. Most authors describe only the apparent rate constant which depends strongly on the parameters like concentrations of educts, temperature, and the concentration of catalyst as mentioned above and does not allow a direct comparison of the catalytic activities.

Pradhan *et al*.[75] studied the growth of silver nanoparticles and found that these particles are able to catalyze the reduction of *p*-nitrohenol (Nip). Furthermore, this reaction does not proceed without metallic nanoparticles and is therefore an ideal model reaction to study the activity of different metallic nanoparticles on different stabilizers. Due to the strong absorption peak of *p*-nitrophenolate at 400 nm, the reaction can be easily followed with UV-vis spectroscopy. In Figure 11 the absorbance at 400 nm for different reaction conditions is shown.

The authors concluded that the reaction has an order of zero with respect to *p*-nitrophenol in case of an instantaneous addition (Figure 11 line (a)). Line (a') of Figure 11 is the result of adding a fresh batch of *p*-nitrophenol directly after the reaction is complete. An addition of a fresh batch of *p*-nitrophenol after completion of the reaction (see Figure 11, line (b) 5 minutes after the completion of the reaction and (c) 15 minutes after the completion of the reaction) results in a first order reaction indicating a change in the reaction mechanism.

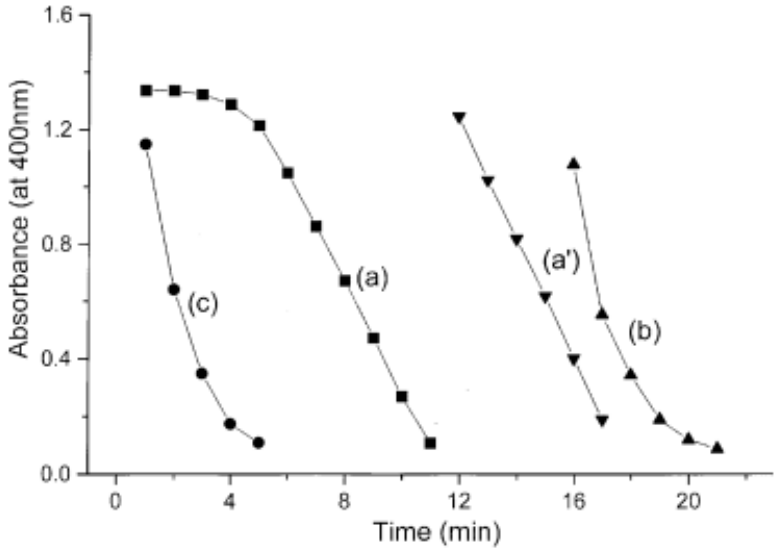

Figure 11: Absorbance curves of p-nitrophenol at 400 nm at different reaction conditions. (a) Instantaneous addition. (a') Introduction of a fresh batch of substrate Nip to the same reaction mixture just before completion of the reduction, (b) 5 min and (c) 15 min after the completion of the reduction. Reprinted from ref [75]. Copyright 2001 with permission from Elsevier.

Regarding line (a) of Figure 11, an induction time is visible. The authors claim, that this time is due to an oxide layer of the nanoparticle surface.[75] Reusing these nanoparticles leads to disappearance of the induction period (Figure 11 line (a')).

Esumi *et al*.[76, 112] applied this model reaction to test the activity of gold nanoparticles stabilized by dendrimers. In Scheme 6 such a stabilized nanoparticle is shown for better imagination. The rate of the reaction was calculated to be pseudo-first order, as indicated in eq. 3.1. By adding an excess of borohydride the reaction rate is dependent solely on the concentration of *p*-nitrophenol:[76]

$$\frac{dc_{Nip}}{dt} = -k_{app} \cdot c_{Nip} \cdot c_{BH4} = -k_{app} \cdot c_{Nip} \qquad 3.1$$

where c_{Nip} is the concentration of *p*-nitrophenol, c_{BH4} the concentration of borohydride, and k_{app} is the apparent rate constant.

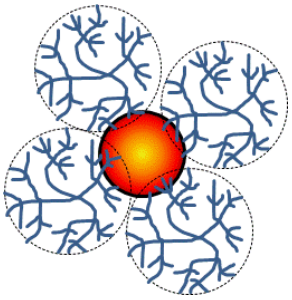

Scheme 6: Scheme of a dendrimer stabilized gold nanoparticle. The blue dendrimers stabilize the nanoparticles by adsorbing onto the surface of the nanoparticles by electrostatic as well as steric forces.

The authors found a dependence of the dendrimer concentration on the rate constant: a higher concentration of dendrimers leads to a lower rate constant for the low generation dendrimers. A high amount is necessary to stabilize the nanoparticles due to the fact that this low generation dendrimers are not spherical. Moreover, for a higher generation, less dendrimer has to be used to stabilize the nanoparticles, thus leading to a higher rate constant.

This was taken as an indicator for the influence of the diffusion of the reactant through the dense layer of dendrimer. The authors used the equation 3.2 which was suggested by Grätzel *et al*..[130] Here the reaction rate is divided into the rate of electron transfer (k_{et}) and the diffusion:[112]

$$\frac{1}{k_{app}} = \left[\frac{1}{4\pi R^2}\right] \cdot \left[\left(\frac{1}{k_{et}}\right) + \left(\frac{R}{D}\right)\right] \qquad 3.2$$

where R is the radius of the particle and D is the diffusion constant.

If $k_{et} << D/R$, the rate is limited by the surface electron transfer reaction, if $k_{et} >> D/R$, then the rate is diffusion controlled and the rate follows the Smoluchowski expression[112]:

$$k_{app} = 4\pi DR \qquad 3.3$$

The authors assume that the electron transfer is fast due to the highly electron donating species such as borohydride ions. Thus, the rate of the reduction is mainly controlled by the diffusion of *p*-nitrophenol and the particle size. Due to the fact that the dendrimers adsorb onto the surface, the diffusion of *p*-nitrophenol is hindered. Therefore, a higher concentration of dendrimers leads to a more covered surface, and thus reduces the reaction rate. Furthermore, by comparison of two different dendrimers, the reaction with the small

dendrimer poly(propyleneimine) (PPI) exhibits a higher rate constant than that of the larger poly(amidoamine) (PAMAM) dendrimer at the same generation. This is attributed to the faster diffusion of *p*-nitrophenol through this smaller PPI dendrimer. In summary, the diffusion of the educts seems to play a major role in the catalytic activity in case of the dendrimer-stabilized nanoparticles.

3.1.1 Reaction Rate Constant

The apparent rate constant is commonly used to compare the catalytic activity, but the influence of the concentration of the catalyst is ignored in this context. The apparent rate constant is dependent on the amount of applied catalyst, thus a comparison of the apparent rate constants of different catalysts is not possible. Therefore, the reaction rate has to be normalized to be comparable. Some authors use the weight of the catalyst (mg L^{-1}), or the molar amount of catalyst (mol L^{-1}) to normalize the apparent rate constant. A better possibility is to calculate the surface of the nanoparticles and normalize the reaction rate with the available surface of the nanoparticles in solution (m^2 L^{-1}). The reduction of *p*-nitrophenol does not proceed without nanoparticles and it was frequently stated that one or both educts adsorb onto the surface. Therefore, the surface area *S* plays a major role. Hence, only the surface normalized reaction rate k_1 will be discussed further.[56, 58, 131]

$$\frac{dc_{Nip}}{dt} = - k_{app} \cdot c_{Nip} = - k_1 \cdot S \cdot c_{Nip} \qquad 3.4$$

In the following table the surface normalized rate constants are summarized, sorted by the metal used for the nanoparticles. For a better comprehension the carrier system, the temperature and the size of the nanoparticles are listed as well.

Table 1: Catalytic activity of metal nanoparticles for the reduction of p-nitrophenol taken or recalculated (*) from literature.

Reference	Carrier system	Metal	*d* [nm]	*T* [°C]	k_1 [$s^{-1}\,m^{-2}L$]
Esumi *et al*. [112]	PAMAM dendrimer	Pd	1.8 ± 0.42	15	3.07×10^{-3} *
	PPI dendrimer	Pd	2 ± 0.41	15	0.776 *
Harish *et al*. [132]	PEDOT	Pd	1 - 9	25	0.022 *
Behrens *et al*. [133]	Protein	Pd	2.85 ± 0.5	22	0.048 *
Bhandari *et al*.[134]	Peptide	Pd	2.6 ± 0.5	20	0.0167*
Halder *et al*.[135]	palladium clusters	Pd	4-5		1.33×10^{-4}
Arora *et al*. [136]	Al_2O_3	Pd	6 ± 0.5	25	0.136 *
Yuan *et al*. [137]	Organo-silica hybrid nanowires	Pt	3 ± 0.5	20	0.31
Wang *et al*. [122]	PNIPAM-P4VP micelles	Au	3.3 ± 0.2	25	3.72×10^{-3} *
Murugadoss *et al*. [138]	acetanilide	Au	5 ± 1.7	RT	0.653
Han *et al*. [139]	PANI nanofiber	Au	2	RT	1.91×10^{-5}
Lu *et al*. [118]	PS-PNIPAM core-shell microgel	Au nanorods	width: 6.6 ± 0.3; length: 34.5 ± 5.2	20	0.14
	PS-PNIPAM core-shell microgel	Au–Pt nanorods	width: 7.4 ± 0.8; length: 39.5 ± 6.5	20	0.21
Liu *et al*. [140]	β-D-Glucosidase	Au	8.2 ± 2.3	25	0.044 *
Zhang *et al*. [128]	PDMAEMA	Au	4.2 ± 1.2		5.03×10^{-4} *
Panigrahi *et al*. [131]	Citrate ligand	Au	20	25	5.23×10^{-6} *
Kuroda *et al*. [141]	PMMA	Au	6.9 ± 5.5	25	0.48-0.53
Wu *et al.* [142]	SiO_2 nanorattle	Au	2.8 ± 0.7	25	5.49×10^{-3}
Wu *et al.* [143]	Collagen fiber	Au	5.2 ± 1.6	25	6.02×10^{-3}
Zhang *et al*. [120]	poly[NIPAM-(maleatedcarboxy methylchitosan)]	Ag	2.81 ± 0.62		0.124
	cross-linked poly[NIPAM-(maleatedcarboxy methylchitosan)]		3.45 ± 0.65		0.196

Lu *et al*. [129]	Anionic SPB	Ag	3 ± 1.2	20	0.078
Lu *et al*. [55]	PS-PNIPAM core-shell microgel	Ag	8.5 ± 1.5	20	0.052
Signori *et al*. [144]	PEI (octane side chain)	Ag	24.5± 4.1	25	0.57
	PEI (butane side chain)	Ag	19.5 ± 9.2	25	$81 \cdot 10^{-3}$
Zhang *et al*. [80]	Titanoxide	Ag	~13	21	0.078
Eising *et al*. [145]	Dextran	Ag	6.1 ± 1.3		1.41
Lu *et al*.[146]	poly(PVA)	Ag	45 ± 5	20	$7.31 \cdot 10^{-5}$
	poly(PVA)/PS-poly(ethyleneglycol) methacrylate	Ag	35 ± 5	20	$7.8 \cdot 10^{-5}$

Subsequently, different examples for the surface normalized rate constant in literature for various systems will be discussed:

In case of gold nanoparticles immobilized on poly(methylmethacrylate) beads, Kuroda *et al*. [141] found a normalized rate constant of $k_1 = 51.0 \cdot 10^{-2}$ L m^{-2} s^{-1}, whereas a chainlike arrangement of gold nanoparticles resulted in a normalized rate constant of $k_1 = 65.32 \cdot 10^{-2}$ L m^{-2} s^{-1}.[138] Here citrate-stabilized gold nanoparticles arrange in linear assembly by acetanilide in an aqueous medium. In contrast, gold nanoparticles fixed on a mesoporous organic gel have a normalized rate constant of $k_1 = 7.4 \cdot 10^{-2}$ L m^{-2} s^{-1}.[117]

Silver nanoparticles inside thermo-responsive hydrogels were analyzed by Zhang *et al*..[120] Two different microgels were used for the immobilization of the nanoparticles, one without cross-linker, and one with the cross-linker N,N'-methylenebisacrylamide. The respective surface normalized rate constants were $k_1 = 12.4 \cdot 10^{-2}$ L m^{-2} s^{-1} and $k_1 = 19.6 \cdot 10^{-2}$ L m^{-2} s^{-1}. Both microgels have nearly the same catalytic properties. For chitosan-silver nanocomposites the normalized rate constant was calculated with $k_1 = 15.0 \cdot 10^{-2}$ L m^{-2} s^{-1}.[147] Signori *et al*.[144] studied the catalytic activity of silver nanoparticles embedded inside branched poly(ethyleneimide) derivates (PEI) with hydrophobic side chains of different length. For the two different systems the normalized rate constants were $k_1 = 57.0 \cdot 10^{-2}$ L m^{-2} s^{-1} for the longer hydrophobic side chain, and $k_1 = 0.8 \cdot 10^{-2}$ L m^{-2} s^{-1} for the shorter. The difference was explained by the different hydrophobic side chains. Those hydrophobic side chains of PEI are furthermore known to be responsible for micellar structures.[144] PEI with the shorter side chains build less compact

micelles and the authors claim that this slows down the diffusion of the reactants. The activity of silver nanoparticles in hydrogels was measured by Lu *et al*..[146] The silver nanoparticles were embedded in a poly(vinylalcohol) (PVA) hydrogel and PVA composite hydrogels with polymer brushes consisting of PS-poly(ethyleneglycol) methacrylate. The respective normalized rate constants were $7.31 \cdot 10^{-5}$ L m^{-2} s^{-1} and $7.8 \cdot 10^{-5}$ L m^{-2} s^{-1}. Zhang *et al*. [80] studied silver nanoparticles embedded on titanium oxide. Thereby a normalized rate constant of $k_1 = 78 \cdot 10^{-2}$ L m^{-2} s^{-1} was obtained. In summary, the catalytic activity of silver nanoparticles varies with the different carrier systems. A high activity was found in case of Zhang *et al*.,[80] where the particles are stabilized at titanium oxide, whereas the activity is very low in case of the compact hydrogels of Lu *et al*.,[146] pointing to an influence of the diffusion of the reactants to the surface of the nanoparticles. Here, the particle size may also influence the catalytic activity due to the fact that smaller nanoparticles exhibit more defects, which promotes the catalytic activity.

In case of platinum functionalized organo-silica hybrid-nanowires, Yuan *et al*. [137] found the surface normalized rate constant to be $k_1 = 31 \cdot 10^{-2}$ L m^{-2} s^{-1}. Lu *et al*. [118] studied gold nanorods and gold nanorods with platinum tips embedded inside microgel particles. As comparison platinum nanoparticles were also measured for their catalytic activity. The normalized rate constants were $k_1 = 14.0 \cdot 10^{-2}$ L m^{-2} s^{-1} (pure gold nanorods), $k_1 = 21.0 \cdot 10^{-2}$ L m^{-2} s^{-1} (Pt NP covered gold nanorods), and $k_1 = 8.6 \cdot 10^{-2}$ L m^{-2} s^{-1} (pure Pt NP), respectively. Therefore the platinum nanoparticles were least catalytic active; the gold-platinum composites were the most active catalysts. This shows a significant enhancement of the bimetallic composites in comparison to the monometallic nanoparticles.

Table 2: Catalytic activity of metal nanoparticles embedded inside of SPB for the reduction of p-nitrophenol.

Reference	Metal	d [nm]	T [°C]	k_1 [$s^{-1}m^{-2}L$]
Mei *et al*. [58]	Pt	2.1 ± 0.4	15	0.56
Mei *et al*. [56]	Pd	2.4 ± 0.5	15	1.10
Schrinner *et al*. [44]	Au	1.3 ± 0.25	20	0.51
Yu *et al*. [148]	Pt	2.1 ± 0.4	20	0.55
	Pd	2.4 ± 0.5	20	1.50
	Au	1.25 ± 0.25	20	0.31
Lu *et al*. [149]	Ag	3 ± 1.2	20	0.078

By comparison of the values above, it is obvious that the surface normalized rate constant varies regarding the different stabilizers. In the following metallic nanoparticles in spherical polyelectrolyte brushes are listed. For this purpose, the influence of the carrier system could be negligible. In spherical polyelectrolyte systems the normalized rate constant follows the order: Pd > Pt > Au > Ag (see Table 1). This effect of the different metallic nanoparticles immobilized in SPB and in microgels is shown in Figure 12.

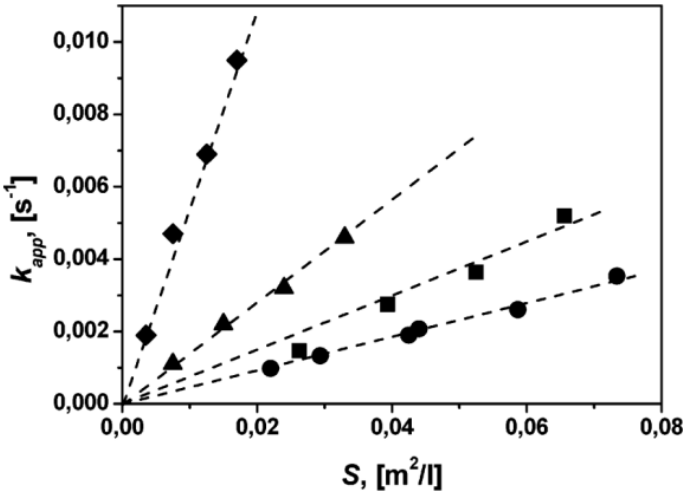

Figure 12: Dependence of the surface area of the nanoparticles (S) on the apparent rate of the reaction. (squares: Ag@SPB, circles: Ag@PNIPAM, triangle: Pd@PNIPAM, diamonds: Pt@SPB). Reprinted with permission from ref [149]. Copyright 2007 American Chemical Society.

Lu *et al*. analyzed silver nanoparticles in various carrier systems. Silver nanoparticles embedded in poly(acrylic acid)-SPB [149] have a normalized rate constant of $k_1 = 7.81 \cdot 10^{-2}$ L m^{-2} s^{-1}, while inside a microgel [150] the normalized rate constant was slightly lower ($k_1 = 5.2 \cdot 10^{-2}$ L m^{-2} s^{-1}). In a SPB with a nanotree-like brush structure, [126] the normalized rate constant was $k_1 = 7.27 \cdot 10^{-2}$ L m^{-2} s^{-1}. Mei *et al*.[56] studied the influence of the carrier system. Here, the Pd NP embedded in a thermo-responsive microgel have a normalized rate constant of $k_1 = 10.1 \cdot 10^{-2}$ L m^{-2} s^{-1} while Pd NP embedded inside a SPB have a normalized rate constant of $k_1 = 110.0 \cdot 10^{-2}$ L m^{-2} s^{-1}. This leads to the conclusion that the influence of the stabilization of the nanoparticles is not negligible. NPs embedded inside SPB, which have a relative open structure, have in all cases the higher surface normalized rate constants than NP embedded inside a microgel. The latter consists of a dense network of cross-linked polymer chains, which hinders the diffusion of the reactants noticeably.

Considering the different rate constants listed above, it is obvious that nanoparticles embedded inside a dense layer of polymer, like a microgel or hydrogel have a considerably lower normalized rate constant than nanoparticles in open structures like on the surface of titanium oxide, SPB or attached to nanowires. In contrast to the open brush structure, this slowing down of the reaction in dense polymeric networks points to a diffusional barrier.

For a detailed analysis of this reaction, the point of diffusion limitation has to be addressed. One possible way for the determination was introduced by Esumi *et al.*[112] by comparing the velocities of the electron relay and the diffusion. They concluded that the reaction in their case is faster than the diffusion through the dendrimer shell. The second Damköhler number (see chapter 2.2.4) is another possibility to calculate whether the reaction is diffusion controlled or rate controlled. Here, the ratio of mass transport and chemical reaction is calculated. If $DaII \ll 1$ the reaction is rate controlled, therefore the diffusion is much faster than the chemical reaction. In case of $DaII \gg 1$ the reaction is diffusion controlled.[98]

3.1.2 Activation Energy

In many cases the apparent reaction rate is employed to compare the activity of these nanoparticles. Furthermore, the activation energy is calculated in special cases to show the agreement of the measured results with literature values. The activation energy can be calculated by:

$$k_{app} = k_0 \cdot exp\left[-\frac{E_A}{RT}\right] \qquad 3.5$$

where k_{app} is the apparent rate constant derived from eq. 3.1, k_0 is the pre-exponential factor, E_A the activation energy, R the gas constant, and T the temperature.

In the following the activation energies for the reduction of *p*-nitrophenol from different research groups are listed according to the used metal:

a) Silver nanoparticles:

Pradhan *et al.*[75] measured an activation energy of $E_A = 41$ kJ mol^{-1} for silver nanoparticles, while Jana *et al.*[151] measured an activation energy of $E_A = 24.1$ kJ mol^{-1} for

silver coated polystyrene beads. Saha *et al*. [152] synthesized silver nanoparticles which exhibits E_A = 12.1 kJ mol^{-1}. In comparison, Manesh *et al*. [153] analyzed silver nanoparticles deposited into polyaniline bridged silica networks. The activation energy was claimed to be E_A = 192 kJ mol^{-1}.[153] In contrast, calculating the activation energy from the given values of k_{app} in the same manuscript, the activation energy of E_A = 24.6 kJ mol^{-1} was obtained.

Table 3: Activation energies for the p-nitrophenol reduction inclusive the carrier systems, sizes and concentrations of the educts.

Reference	Metal (carrier system)	c_{Nip} [M]	c_{BH4} [M]	d_{NP} [nm]	E_A [kJ mol^{-1}]
Pradhan *et al*. [75]	Ag NP (-)	6.00x10^{-5}	2.5x10^{-3}	7-15	41
Jana *et al.* [151]	Ag NP (silver coated PS bead)	1.00x10^{-4}	1.0x10^{-1}	shell thickness 30 ± 5	24.1
Saha *et al*. [152]	Ag NP (calcium alginate stabilized)	1.00x10^{-4}	1.0x10^{-1}	7 ± 2	12.1
Manesh *et al*. [153]	Ag NP (silica network)	1.00x10^{-4}	1.0x10^{-2}	10	192
Shin *et al*. [154]	Ag NP (Fe_2O_3 carrier)	1.03x10^{-4}	1.05x10^{-2}	~28	45

b) Gold nanoparticles:

Saha *et al*. [152] stabilized gold nanoparticles by calcium alginate. Here, the activation energy was E_A = 20.5 kJ mol^{-1}. Furthermore, it was found that in this case the reaction follows a zero order with respect to *p*-nitrophenol. This was extracted from a plot of the reaction time vs. the concentration of *p*-nitrophenol. For magnetically recoverable gold nanoparticles an activation energy of E_A = 51.2 kJ mol^{-1} was determined.[155] An activation energy of E_A = 38 kJ mol^{-1} was found by Kuroda *et al*.[141] for gold nanoparticles on poly(methyl methacrylate) beads. Gold nanoparticles stabilized by self-assembling micellar systems were analyzed by Chen *et al*..[123] They analyzed the activity at different temperatures and observed a linear dependence of the inverse temperature and the rate constant, yet the value of the activation energy was not mentioned in the text.[123] Panigrahi *et al*. [131] compared gold nanoparticles immobilized by commercial anion exchanger and gold sol to distinguish the effect of the carrier system. The activation energy for the immobilized nanoparticles was

E_A = 31 kJ mol^{-1} for 20 nm gold particles.[131] The authors explained that the activation energy decreases with a decreasing particle size, which was attributed to the increased surface roughness by smaller particles. Smaller nanoparticles are composed of more unsaturated surface atoms, which increase the surface roughness. This promotes the adsorption of the *p*-nitrophenolate ions and therefore the reduction of *p*-nitrophenol. While larger particles consist mostly of low index, high-coordinated surface atoms which lower the surface roughness of the nanoparticle.[131] Zeng *et al*. [156] tested the catalytic activity of gold particles with different shapes, namely nanocages, nanoboxes, and partially hollow nanoboxes. The activation energy they derived was 28.0 ± 1.4 kJ mol^{-1}, 44.3 ± 2.62 kJ mol^{-1}, and 55.4 ± 3.2 kJ mol^{-1}, respectively.

Table 4: Activation energies for the p-nitrophenol reduction inclusive the carrier systems, sizes and concentrations of the educts.

Reference	Metal (carrier system)	c_{Nip} [M]	c_{BH4} [M]	d_{NP} [nm]	E_A [kJ mol^{-1}]
Panigrahni *et al*. [131]	Au NP (citrate-stabilized)	1.00x10^{-4}	6.67x10^{-3}	20	31
Chang *et al*. [155]	Au NP (chitosan-coated ironoxide carrier)	2.00x10^{-4}	6.67x10^{-4}	3.1	51
Kuroda *et al*. [141]	Au NP (PMMA beads)	4.94x10^{-5}	7.22x10^{-2}	6.9	38
Saha *et al*. [152]	Au NP (calcium alginate stabilized)	1.00x10^{-4}	1.0x10^{-1}	5 ± 2	20.5
Zeng *et al*. [156]	Au nanocage	1.40x10^{-4}	4.20x10^{-2}	50	28
	Au nanobox	1.40x10^{-4}	4.20x10^{-2}	50	44
	Au hollow nanobox	1.40x10^{-4}	4.20x10^{-2}	50	55

c) Platinum, palladium and bimetallic nanoparticles:

Mahmoud *et al*. [157] compared free platinum nanocubes and platinum nanocubes embedded on poly(styrene) beads. The apparent reaction rate of the stabilized nanocubes was approximately 7 times lower. This could arise from a) differences in the surface area, b) different diffusion barriers or c) differences in the effective concentration of the nanocubes. The poly(styrene) spheres were considered as an inert stabilizer, because both systems have

nearly the same activation energy with 13.8 ± 1.6 kJ mol^{-1} and 12.1 ± 1.6 kJ mol^{-1}, respectively. The apparent reaction rate was here calculated from the slope of ln(A) which was not normalized to A_0 at t = 0 s. A compensation effect by studying hollow nanocages with different compositions was discovered by Mahmoud *et al.*.[158] Beside pure platinum and palladium nanocages, a platinum-palladium alloy nanocage, and core shell particles from platinum-palladium and palladium-platinum nanocages were synthesized. The activation energies are $E_A = 68$ kJ mol^{-1}, $E_A = 95$ kJ mol^{-1}, $E_A = 109$ kJ mol^{-1}, $E_A = 78$ kJ mol^{-1}, and $E_A = 87$ kJ mol^{-1}, respectively. Arora *et al.*[136] studied palladium nanoparticles embedded on alumina with an activation energy of $E_A = 43$ kJ mol^{-1}. Ghosh *et al*.[78] studied the reduction of *p*-nitrophenol with bimetallic platinum-nickel nanoparticles. From the slope of ln(A_t) for different temperatures the activation energy was derived with $E_A = 30.9$ kJ mol^{-1}. Sahiner *et al*. [119, 121] synthesized nanoparticles inside hydrogels. In case of cobalt nanoparticles an activation energy of $E_A = 27.8$ kJ mol^{-1} and in case of nickel nanoparticles an activation energy of $E_A = 25.7$ kJ mol^{-1} was found.

Table 5: Activation energies for the p-nitrophenol reduction inclusive the carrier systems, sizes and concentrations of the educts.

Reference	Metal (carrier system)	c_{Nip} [M]	c_{BH4} [M]	d_{NP} [nm]	E_A [kJ mol^{-1}]
Mahmoud *et al*. [157]	Pt-cubes (PS)	1.95×10^{-5}	3.16×10^{-2}	20	13.8
	Pt-cubes (colloidal)			20	12
Mahmoud *et al*. [158]	Pt Pd Alloy nanocubes	2.60×10^{-2}	3.12×10^{-2}	cavity:49	110
	Pd nanocubes			cavity:53	95
	Pt Pd nanocubes			cavity:57	78
	Pd Pt nanocubes			cavity:51	87
	Pt nanocubes			cavity:52	68
Arora *et al.* [136]	Pd NP (Al_2O_3)	1.0×10^{-4}	1.3×10^{-2}	6±0.5	43
Ghosh *et al*. [78]	Pt-Ni Alloy (CTAB)	8.5×10^{-5}	1.2×10^{-2}	19 ± 3	31
Sahiner *et al*. [121]	Ni NP (hydrogel network)	1.44×10^{-2}	2.88×10^{-1}	100	26
Sahiner *et al*. [119]	Co NP (hydrogel network)	1.44x10-^{2}	2.88×10^{-1}	50-100	28

d) Nanoparticles inside of SPB:

Spherical polyelectrolyte brush systems can act as carriers for different metallic nanoparticles. Mei *et al*. [56, 58] synthesized platinum nanoparticles with an activation energy of $E_A = 43.7$ kJ mol^{-1}[58] and palladium nanoparticles with $E_A = 44$ kJ mol^{-1}.[56] Schrinner *et al*.[44] used SPB as carrier systems for gold nanoparticles and measured the activation energy with $E_A = 43$ kJ mol^{-1}. Lu *et al*.[126] synthesized silver nanoparticles in a tree-like brush system with an activation energy of $E_A = 62$ kJ mol^{-1}.

By studying the activation energies above, it is obvious that the values differ a lot. For example, the activation energies for gold nanoparticles vary between $E_A = 20$ kJ mol^{-1} and $E_A = 50$ kJ mol^{-1}, for silver nanoparticles they vary between 12 and 40 kJ mol^{-1}. Considering the findings of Zeng *et al*.[156], the structure of the nanoparticles may have an influence on the activation energy. The results from Mahmoud *et al*. [158] points in a similar direction. In contrast, activation energies from metallic nanoparticles inside the spherical polyelectrolyte brushes are very similar. All activation energies are around $E_A = 45$ kJ mol^{-1} except for silver nanoparticles. Here, the activation energy is higher, but in this case the brush system is distinctively different. A bottle brush polyelectrolyte was used instead of a linear polyelectrolyte.

In summary, the activation energies vary with regard to different stabilizing systems and metals used in the kinetic analysis. The compensation plot, mentioned by Zeng *et al*.,[156] may be an explanation for this behavior. They found a linear dependence of the pre-exponential factor k_o and the activation energy [156](see Figure 13) and explained this compensation effect by switching of the kinetic regime. This switching takes place from an activation-rate dominated regime, in this case *p*-nitrophenol, to a regime where the rate was dominated by the stability of the adsorbed reaction product *p*-aminophenol on the surface.

Mahmoud *et al*.[158] found a linearity of the pre-exponential factor k_o and the activation energy, as well. They attributed this to a similar reaction mechanism independent of the metal used in the catalysis.

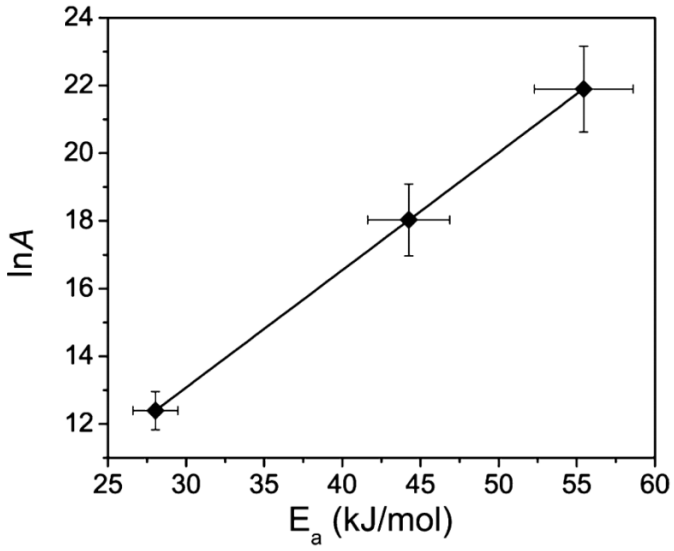

Figure 13: Compensation plot of the pre-exponential factors (ln A)and the activation energies (E_a) of the Arrhenius equation for catalysts based on Au nanocages or nanoboxe. Reprinted with permission from ref [156]. Copyright 2010 American Chemical Society.

The compensation can be described by a linear dependence of the activation energy on the rate with:[159]

$$\ln k_0 = p \cdot E_A + q \qquad 3.6$$

where

$$p = \frac{1}{RT_{iso}}$$

and

$$q = \ln k_{iso}$$

where T_{iso} and k_{iso} are the isokinetic temperature and isokinetic rate constant, respectively. At isokinetic conditions the slopes should cross in one point. At T_{iso} all reactions have the same reaction rate k_{app}. Above this temperature reactions with higher activation energy are more active, below this temperature, reactions with a lower activation energy are more preferred. Such a kind of compensation plot has been reported for different catalytic reactions.[159] Some explanations for this behavior were given with: a) An inhomogeneous surface was assumed with a Gaussian distribution of active sites on the surface. Highly active centers due to their low E_A are rare compared to the low active centers with a high E_A. This ansatz leads to a connection of $\ln k_0$ and E_A in which the proportionality constant p appeared as a distribution constant. [159] b) A quasi-equilibrium between reactants and a transition

state or an activated complex [159, 160] c) The use of the apparent activation energy, which is dependent on the surface coverage [159, 161, 162] d) Or a switching of kinetic regimes.[163]

3.1.3 Induction Time

Additionally to the information which can be gained from the apparent rate constant, an induction time is visible in several experiments. This was found by Pradhan *et al*.[75] for silver nanoparticles. In Pradhans case the induction time was explained by an oxide layer on the surface of the silver nanoparticles. Moreover, the induction time is diminishing by applying a nitrogen atmosphere instead of air. For silver nanoparticles the explanation of an oxide shell is commonly used.[120, 164, 165] Another possible reason for the induction period was dissolved oxygen in the reaction solution.[126, 131, 166, 167] The induction time is occasionally explained with the diffusion of the educts,[168] *p*-nitrophenol [139, 156, 169, 170] or borohydride.[144]

In several publications the induction time is simply described as time expended for activation of the nanoparticles.[58, 138, 144, 147, 150, 171, 172] This induction time diminishes upon a reuse of the catalyst, which is similar to the observation of Pradhan *et al*.[75] as mentioned above. Plotting the inverse induction time vs. the inverse temperature, the activation energy of the inverse induction time is nearly the same as the activation energy for the reaction rate.[44, 56, 58, 126]

The observation of an induction time is also influenced by the analysis of the reduction of *p*-nitrophenol. If the measurements are conducted every few minutes as done for example in references [136, 173, 174] a short induction time of a few tens of seconds may be not recorded.

Zhou *et al.*[175] found fluctuations in turn-over frequencies for the reduction of resazurin to resorufin by hydroxylamine over a single gold nanoparticle with single-molecule fluorescence microscopy. These fluctuations correlate with the activity of the respective nanoparticles and have a similar time frame as the induction time in case of the *p*-nitrophenol reduction. They suppose that this fluctuations were attributed to the surface restructuring of these nanaparticles.

3.2 Reduction of *p*-Nitrophenol Using Metal Nanoparticles inside SPB as Catalysts

In this thesis, metallic nanoparticles are synthesized in order to analyze their catalytic activity and the mechanism of the reduction of *p*-nitrophenol. Thereby, the SPB are synthesized in a two-step polymerization. First the polystyrene core is polymerized in a radical emulsion polymerization with a thin layer of the photo initiator 2-[*p*-(2-hydroxy-2-methylpropiophenon)]-ethylenglycol methacrylat (HMEM) on the particle surface. The core particles exhibit a hydrodynamic radius of 40.7 nm as measured by DLS after cleaning by ultra-filtration. Thereafter, a shell of polyelectrolyte brushes is grown on the surface of the core via photo-emulsion polymerization by choosing a suitable monomer for stabilization of the nanoparticles.[41-43] For example, the monomer stabilizing gold is in this work 2-aminoethyl methacrylate hydrochloride (AEMH) and for platinum it is 2-[(methacryloyloxy) ethyl] trimethylammonium chloride (TMAEMAC), respectively. DLS measurements confirmed the growth of the polyelectrolyte shell. The brush thickness is 96 nm in case of poly(TMAEMAC) and 60 nm for poly(AEMH).

The metallic nanoparticles are synthesized as described in chapter 2.1.2. The metal salt is added into the SPB-brush solution and then reduced to their respective nanoparticles by sodium borohydride. Figure 14 shows the TEM images of the metal nanoparticles synthesized by using SPBs as carrier systems. Platinum nanoparticles with a size of 2.3 ± 0.4 nm and gold nanoparticles with the sizes of 1.5 ± 0.5 nm and 2.2 ± 0.4 nm are employed for the catalytic studies. The HR-TEM micrographs of gold nanoparticles, synthesized after the same recipe, reveal that the nanoparticles are facetted. This is shown in the Figure 14 in the magnifications at the bottom.

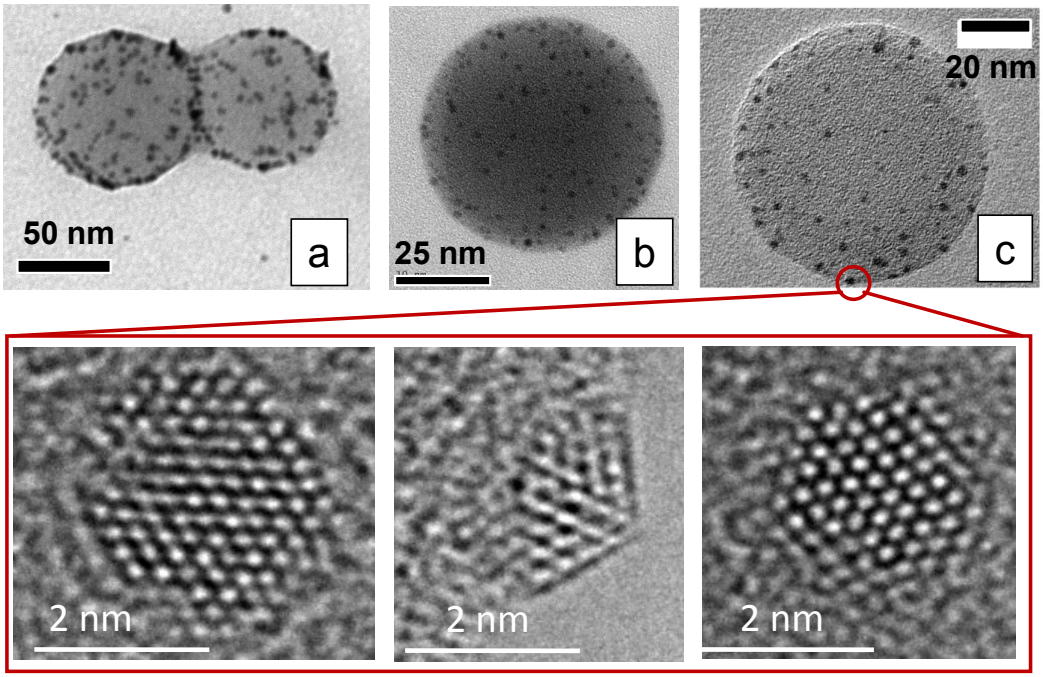

Figure 14: TEM micrographs of the platinum nanoparticles with a diameter of 2.3 nm (a), gold nanoparticles with a size of 1.5 nm (b), and gold nanoparticles with a size of 2.2 nm. Enlarged by the use of the HR-TEM, it can be seen that the gold nanoparticles are facetted.

These nanoparticles, synthesized as above, are applied as catalyst for the reduction of *p*-nitrophenol. The reaction can be analyzed by a first order rate law due to the fact that an excess of borohydride is used. In Figure 15a, the absorption of *p*-nitrophenol and the following decrease of the peak at 400 nm is shown. From this plot, Figure 15b can be obtained by normalizing with the absorption at 400 nm at a given time (A) by the absorption at 400 nm at $t = 0$ s (A_0). In Figure 15b a short time frame is visible, where the absorption does not change. This is the induction time (t_0). From the subsequent slope of the absorbance in Figure 15b (marked with blue) the apparent rate constant (k_{app}) is calculated by a pseudo first order reaction (eq. 3.1). Based on this apparent reaction rate, further aspects are investigated.

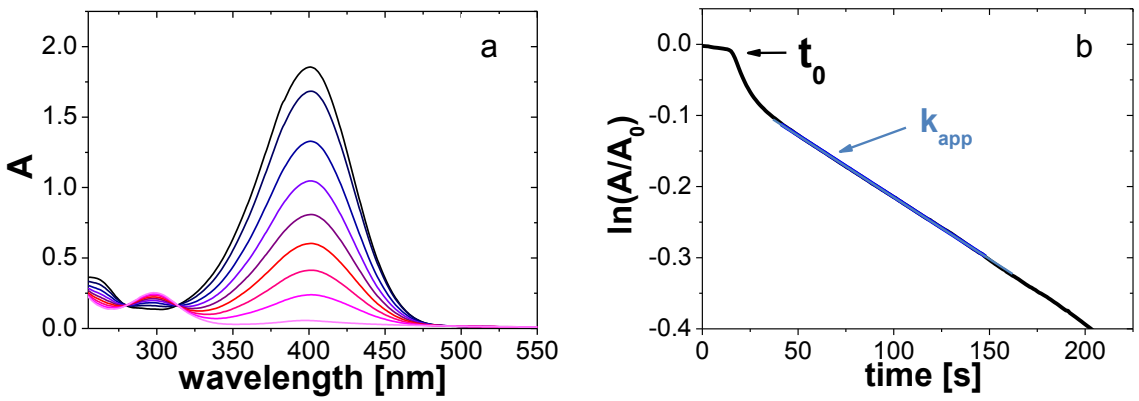

Figure 15: a) UV-vis Spectra of the reduction of p-nitrophenol and b) dependence of the absorption peak of p-nitrophenol at 400 nm with the reaction time.

In case of the nanoparticles used in this work, the apparent rate constant (k_{app}) has a linear dependence on the surface of the metallic nanoparticles as shown in Figure 16 for gold nanoparticles with a size of 2.2 ± 0.4 nm. The surface normalized rate constant is $k_1 = 0.26 \pm 0.01$ L m^{-2} s^{-1}, which is in good agreement with the measurements of Yu *et al.* [148] (see chapter 3.1.1, Table 2) and slightly lower than that measured by Schrinner *et al.*.[44] This demonstrates that the apparent rate constant is related to the amount of catalyst in the system.

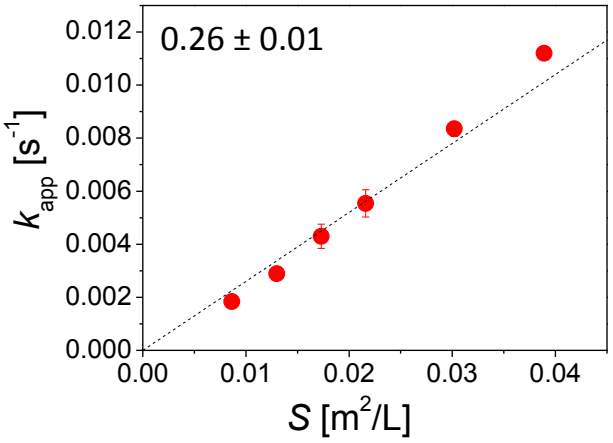

Figure 16: Dependence of the apparent rate constant on the surface of the added nanoparticles, in this case Au NP with a size of 2.2 ± 0.4 nm at constant concentrations of 0.1 mM Nip and 10 mM BH_4^-.

3.2.1 Investigation of the Reaction Mechanism

As mentioned above, two reaction mechanisms are possible for a surface reaction. One is the Eley-Rideal model, where one of the educts adsorbs to the surface and reacts with the educt in solution. Another mechanism is the Langmuir-Hinshelwood model, where both educts adsorb onto the surface and react on the surface.

Zhang *et al.*[80] suggested that borohydride transfers a surface hydrogen species, which reacts with the *p*-nitrophenol to produce *p*-aminophenol. This would imply a Langmuir-Hinshelwood mechanism. Meanwhile, Khalavka *et al.*[81] suggested that hydrogen adsorbs onto the surface, which reacts with the *p*-nitrophenol from solution. This was assigned to the fact that, with a higher concentration of catalyst, a linear growth in the reaction rate could be achieved. In both works the proposed reaction mechanism was given without a reason for this conclusion. To get precise information which reaction model is valid, two sets of experiments are performed as shown in Figure 17.

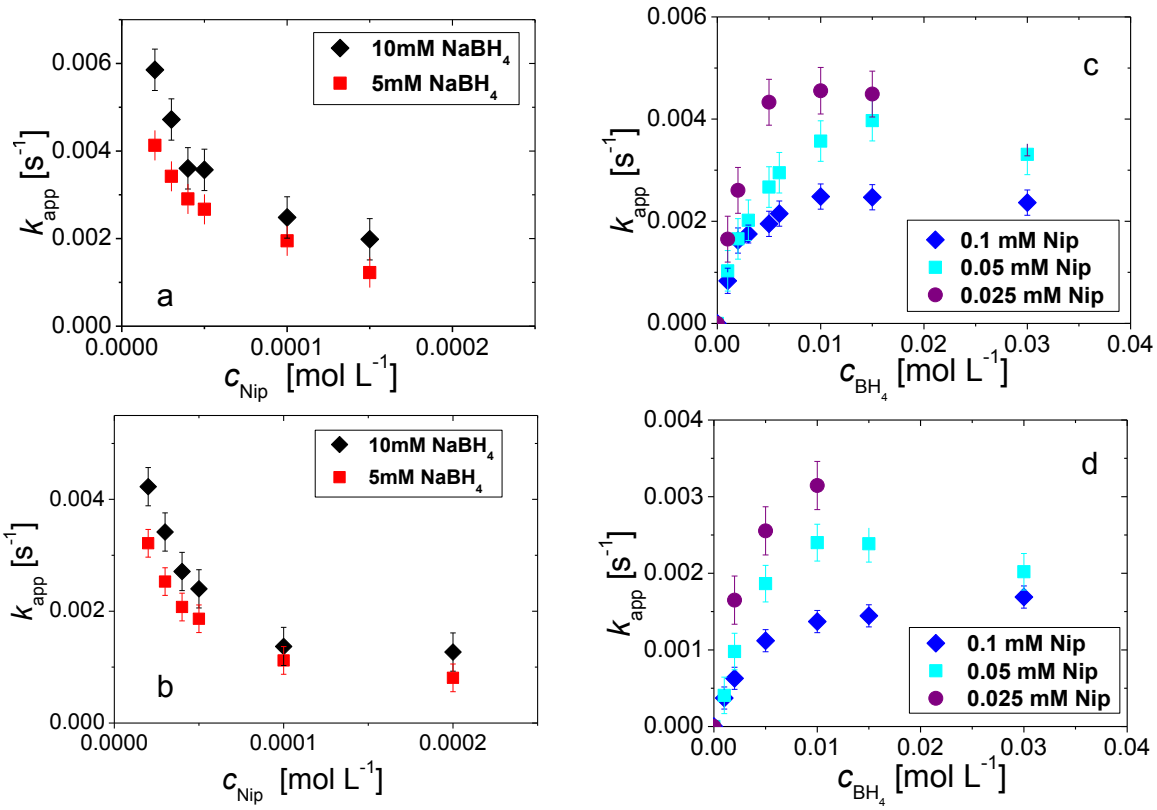

Figure 17: Apparent rate constant k_{app} vs. the concentration of Nip (c_{Nip}, left) and BH_4^- (c_{BH4}, right): The surface area of Pt nanoparticles is S = 0.00687 $m^2 L^{-1}$ for panels (a) and (c). The Panels (b) and (d) describe the kinetic data taken for Pt-nanoparticles with a surface area of S = 0.00481 $m^2 L^{-1}$.

At first, a wide concentration regime of *p*-nitrophenol is tested with a constant concentration of sodium borohydride. Secondly, various concentrations of sodium borohydride are investigated with constant concentrations of *p*-nitrophenol. These concentration variations are shown in Figure 17. On the left side, the concentration variation of *p*-nitrophenol and on the right side, the variations of the concentration of sodium borohydride is presented.

By studying the rate constant dependence on the concentration of *p*-nitrophenol and sodium borohydride in Figure 17, it becomes evident that this reaction follows a Langmuir-Hinshelwood mechanism because of the following fact: The rate constant is decreasing with an increasing concentration of *p*-nitrophenol, whereas for an increasing concentration of borohydride the rate is reaching a maximum. In case of an Eley-Rideal reaction mechanism, the rate should be increasing linearly with the concentration of the reactant, which is not adsorbed onto the surface. The experiments shown in Figure 17 reveal definitely a non-linear dependence for both concentration variations, which indicates that the Eley-Rideal mechanism does not apply. This work will focus on the detailed analysis of the Langmuir-Hinshelwood mechanism of nanoparticle catalyzed reactions.

3.2.2 Langmuir-Hinshelwood Reaction Mechanism

A possible reaction scheme for the Langmuir-Hinshelwood mechanism is shown in Scheme 7. Both reactants, borohydride as well as *p*-nitrophenol, adsorb onto the surface. The borohydride adsorption leads to a surface-hydrogen species. Concomitantly, *p*-nitrophenol adsorbs on the surface. Both adsorptions are reversible and can be modeled with a Langmuir isotherm. Furthermore, the diffusion of the reactants to the nanoparticles and the adsorption/desorption equilibrium are assumed to be fast. In a rate determining step, the surface hydrogen-species and the *p*-nitrophenol react with each other and the product *p*-aminophenol desorbs from the surface of the catalyst.

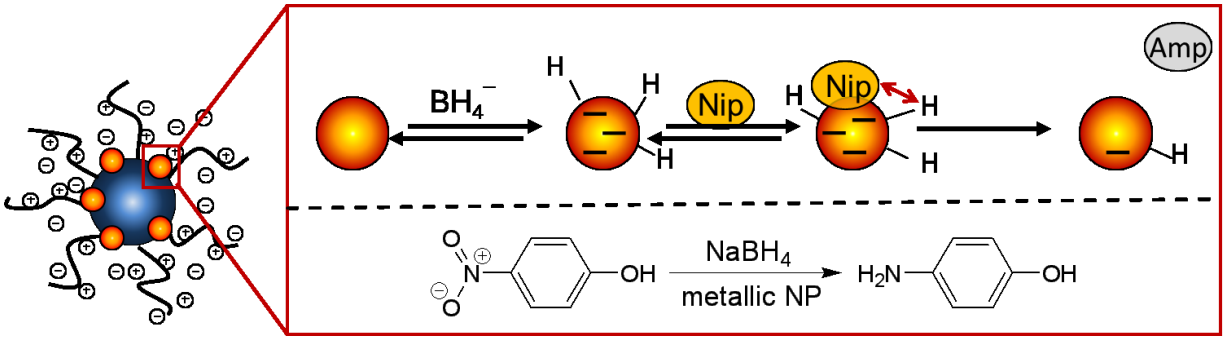

Scheme 7: Reaction pathway of the reduction of p-nitrophenol by the Langmuir-Hinshelwood mechanism. First the educts p-nitrophenol (Nip) and borohydride (BH_4^-) adsorb onto the surface. In case of the borohydride a surface hydrogen species is transferred to the surface. Then both adsorbed species react to the p-aminophenol (Amp) which then desorbs from the nanoparticle surface.

One requirement of the Langmuir-Hinshelwood mechanism is that the rate determining step is the surface reaction. Therefore, the diffusion of the educts to the nanoparticle surface and the diffusion of the products from the surface should be faster than the reaction step itself. One possibility to estimate this is the second Damköhler number (*DaII*, chapter 2.2.4, eq. 2.25).[98] Values above unity (*DaII* >> 1) designate a diffusion controlled reaction, because the reaction is faster than the diffusion of the educts. *DaII* numbers below unity (*DaII* << 1) point to a reaction rate controlled system, where the diffusion is much faster compared to the reaction rate. In the following the *DAII* is calculated for SPB systems:

The mass transport coefficient β is given by $\beta = \frac{D}{\delta}$ with the diffusion coefficient D and the characteristic length scale δ over which mass transport takes place. The brush thickness of the SPB is approximately 40 nm, which is used as this characteristic length scale. The diffusion coefficient of *p*-nitrophenol in water at 20 °C is $6.92 \cdot 10^{-10}$ m^2 s^{-1}.[176] Therefore, β is given as $1.73\ 10^{-2}$ m s^{-1}. The interfacial area of the nanoparticles is S = 10.78 m^{-1} in case of the gold nanoparticles. At the concentration of c_{BH4} = 10 mM and c_{Nip} = 0.1 mM the rate constant is $k_{app} = 1.49 \cdot 10^{-2}$ s^{-1}. With these parameters the *DaII* is calculated to be *DaII* = $8 \cdot 10^{-3}$, which is far below unity and therefore the reaction is not diffusion controlled.

As mentioned in chapter 3.1, another ansatz to distinguish between a rate controlled and a diffusion controlled reaction is given by eq. 3.2. Here the electron transfer and the diffusion is compared. This would reduce the reduction of *p*-nitrophenol solely to the electron transfer from the metal to the nitro-group. However, the overall reaction on the surface is more complex. The reduction includes the transfer of protons to the nitro group, beside the transfer of electrons.

3.2.3 Adsorption Isotherms

The kinetic data in Figure 17 was first modeled by a Langmuir-Hinshelwood mechanism. The back reaction is excluded due to simplification of the model, as already mentioned in chapter 2.2. For the adsorption of the educts the simplest isotherm, the Langmuir isotherm is used:

$$\theta_i = \frac{K_i c_i}{1 + \sum_{j=1}^{N} (K_j c_j)} \qquad 3.7$$

where θ_i is the surface coverage of the educt i; K_i the adsorption constant of i, and c_i the concentration of i. The kinetic data can be modeled with:

$$k_{app} = \frac{k \cdot S \cdot K_{Nip} \cdot K_{BH_4^-} \cdot c_{BH_4^-}}{\left(1 + K_{Nip} \cdot c_{Nip} + K_{BH_4^-} \cdot c_{BH_4^-}\right)^2} \qquad 3.8$$

K_{Nip} and K_{BH4} are the adsorption constants for *p*-nitrophenol and borohydride, k is the intrinsic rate constant, S the surface of the nanoparticles and c_{Nip} and c_{BH4} are the concentrations for *p*-nitrophenol and borohydride.

The whole surface (S) is assumed to be active, since the total amount of active sites is very difficult to obtain for metal nanoparticles. S can be calculated by the metal content and the diameter of the nanoparticles, assuming spherical particles. The metal fraction is obtained by the TGA-measurements, while the diameter is determined by TEM micrographs. Assuming the same density of the metal in the form of nanoparticles or of the respective bulk metal, the surface of the nanoparticles can be gained. With these parameters the other variables in equation 3.8 can be obtained. Two concentrations of platinum nanoparticles are measured for the Langmuir-Hinshelwood mechanism as shown in Figure 18. Measurements with both catalyst concentrations can be modeled with the same set of parameters for the adsorption constants and the intrinsic rate constant. This proves that the influence of the surface of the nanoparticles is solely described with the parameter S and therefore the validity of our approach of the Langmuir-Hinshelwood ansatz is confirmed.

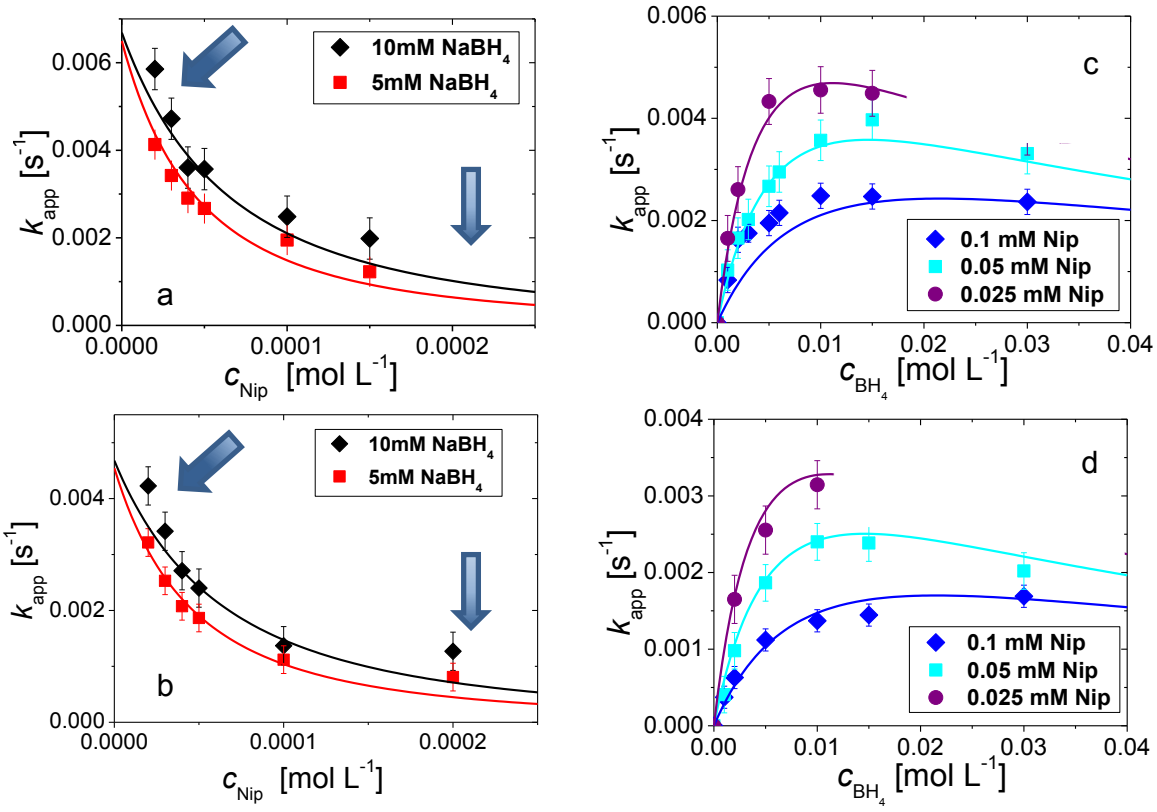

Figure 18: Apparent rate constant k_{app} vs. the concentration Nip (c_{Nip}, left) and BH_4^- (c_{BH4}, right): The solid lines show the results of the Langmuir-Hinshelwood-model with a Langmuir isotherm. The surface area of Pt nanoparticles is S = 0.00687 $m^2 L^{-1}$ for panels a and c and S = 0.00481 $m^2 L^{-1}$ for panels b and d. The arrows mark the strong deviation of the predicted rate constants from the Langmuir-Hinshelwood model.

Figure 18 shows the experimental data modeled with the Langmuir-Hinshelwood model under assumption of a Langmuir isotherm (eq. 3.7). The model fits the concentration variations of borohydride quite well, but the variation of the concentration of *p*-nitrophenol is not captured (see blue arrows). The smallest and highest concentrations cannot be described by the Langmuir-Hinshelwood model.

The modification of the Langmuir isotherm to a Langmuir-Freundlich (LF) isotherm (eq. 2.18) leads to a better agreement with the kinetic data. The LF isotherm takes into account that the surface is not homogeneous and the adsorption energy of the active sites is diverging. The distribution of the adsorption energy is described by a Gaussian distribution. The Freundlich exponent *n* decreases with increasing surface heterogeneity which is described by the width of the Gaussian distribution.

$$\theta_i = \frac{(K_i c_i)^{n_i}}{1 + \sum_{j=1}^{N} (K_j c_j)^{n_j}} \qquad 3.9$$

Further rearrangement of equation 3.10 leads to equation 3.11, which is used to model the catalytic activity. The solid lines in Figure 19 represent the best fit of the modified Langmuir-Hinshelwood model.

$$-\frac{dc_{nip}}{dt} = \frac{k \cdot S \cdot \left(\cdot K_{Nip} . c_{Nip}\right)^{n} \cdot \left(K_{BH_4^-} \cdot c_{BH_4^-}\right)^{m}}{(1 + \left(K_{Nip} . c_{Nip}\right)^{n} + \left(K_{BH_4^-} \cdot c_{BH_4^-}\right)^{m})^2} = k_{app} \cdot c_{nip} \qquad 3.10$$

$$k_{app} = \frac{k \cdot S \cdot K_{Nip}^{n} \cdot c_{Nip}^{n-1} \cdot \left(K_{BH_4^-} \cdot c_{BH_4^-}\right)^{m}}{(1 + \left(K_{Nip} . c_{Nip}\right)^{n} + \left(K_{BH_4^-} \cdot c_{BH_4^-}\right)^{m})^2} \qquad 3.11$$

In Table 6 the determined parameters are listed. The adsorption constant for *p*-nitrophenol is two orders of magnitude higher than that of borohydride. This explains the different dependence of the rate constant on the concentrations of *p*-nitrophenol and borohydride on the rate constant.

A higher concentration of *p*-nitrophenol leads to a decreasing rate constant because the surface is blocked with the *p*-nitrophenol and therefore less borohydride can adsorb. In contrast, an increasing concentration of borohydride leads to an increasing rate constant, because it supplants the *p*-nitrophenol. Further increase of the borohydride concentration leads to a decrease of the rate constant due to saturation of borohydride on the catalyst surface.

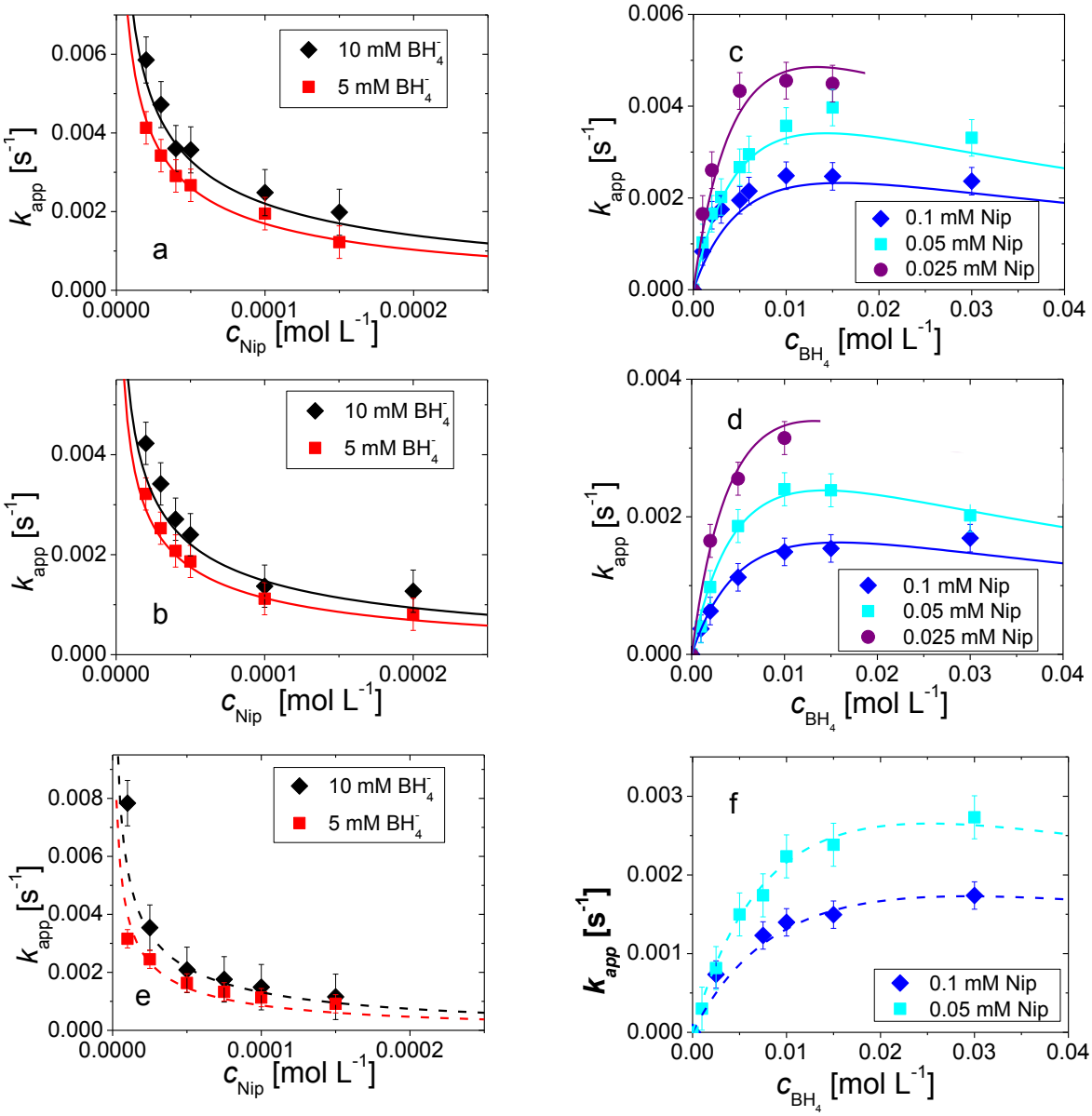

Figure 19: Apparent rate constant k_{app} vs. the concentration Nip (c_{Nip}, left) and BH_4^- (c_{BH4}, right): The lines represent the results of the modified Langmuir-Hinshelwood model. The surface area of Pt nanoparticles is $S = 0.00687\ m^2\ L^{-1}$ for panels a and c and $S = 0.00481\ m^2\ L^{-1}$ for panels b and d. Panels e and f describe the kinetic data obtained for Au nanoparticles. The dashed lines display the calculated results of the modified Langmuir-Hinshelwood model for the gold nanoparticles. The surface area in the case of Au is $S = 0.01078\ m^2\ L^{-1}$. The calculated results of the modified Langmuir-Hinshelwood-model are listed in Table 6.

Table 6: Summary of the rate constants, and the adsorption constants of Nip and BH_4^- according to eq. 3.11.

Metal	k [mol m^{-1} s^{-1}]	K_{Nip} [L mol^{-1}]	K_{BH4} [L mol^{-1}]	n	m
Pt	$4.6 \pm 0.6 \cdot 10^{-4}$	2300 ± 500	89 ± 10	0.6 ± 0.1	1 ± 0.1
Au	$1.6 \pm 0.6 \cdot 10^{-4}$	5500 ± 1000	58 ± 5	0.6 ± 0.1	1 ± 0.1

Another proof of the proposed reaction model is the linear dependence when plotting $k_{app} \cdot c_{Nip}$ versus $\theta_{Nip} \cdot \theta_{BH4}$. According to equation 3.10 the slope represents the surface of the nanoparticles multiplied by the intrinsic rate constant, which is symbolized by the lines in Figure 20. The various data points show clearly this linear dependency for the platinum nanoparticles at two different concentrations and the gold nanoparticles. Thus, the Langmuir-Hinshelwood ansatz with the Langmuir Freundlich isotherm as adsorption isotherm describes the kinetic data in the limit of errors and therefore is a valid description of the reduction reaction.

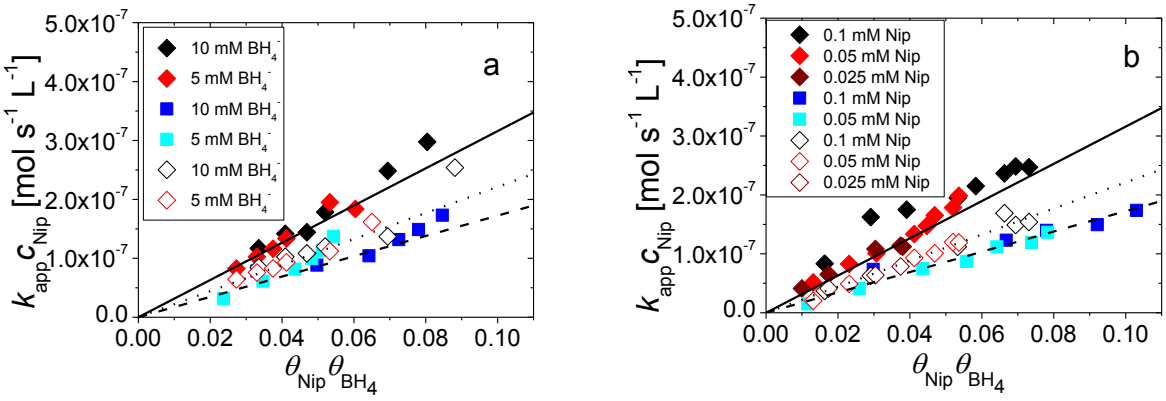

Figure 20: Dependence of the rate constant times the concentration of p-nitrophenol ($k_{app} \cdot c_{Nip}$) on the surface coverage of the nanoparticles ($\theta_{Nip} \cdot \theta_{BH4}$). The solid diamonds stand for the platinum nanoparticles with $S = 0.00687$ $m^2 L^{-1}$, while the hollow diamonds depict the platinum nanoparticles with $S = 0.00481$ $m^2 L^{-1}$, and the blue squares symbolize the gold nanoparticles with $S = 0.01078$ $m^2 L^{-1}$.

3.2.4 Temperature dependence of the apparent rate constant

By testing the catalytic activity at different temperatures the apparent activation energy can be obtained via the Arrhenius equation (eq. 3.5).

$$k_{app}=k_0 \cdot exp\left[-\frac{E_A}{RT}\right] \qquad 3.5$$

In the case of platinum particles with a diameter of 2.3 nm, deposited on spherical polyelectrolyte brushes, the activation energy E_A is calculated by the data shown in Figure 21. The activation energy of the reciprocal induction period ($1/t_0$) of these nanoparticles is determined to be 42 kJ mol^{-1} (red diamonds in Figure 21) and the activation energy of k_1 is 40 kJ mol^{-1} (black dots). These energies are very similar, a phenomenon found as well in previous work with SPB stabilized nanoparticles.[44, 56, 58] Therefore, a connection between the catalyzed reaction and the induction time can be assumed. For further information on the induction time see chapter 3.2.7.

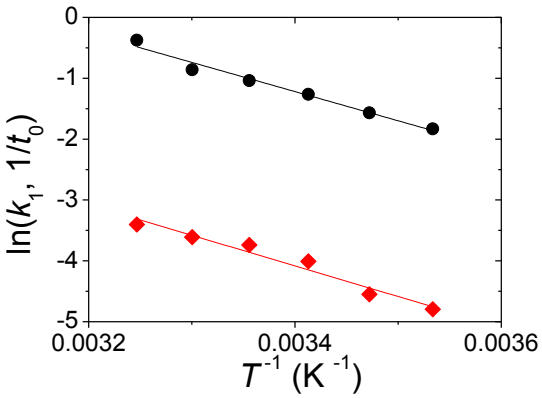

Figure 21: Arrhenius plot of the apparent rate constant k_1 (black dots) and the inverse induction time t_0 (red diamonds) for platinum nanoparticles with a diameter of 2.3 nm embedded inside spherical polyelectrolyte brushes.

In order to analyze the kinetic study of the reduction of *p*-nitrophenol in more detail, the temperature dependence of the Langmuir-Hinshelwood mechanism is measured for gold nanoparticles with a diameter of d = 2.2 ± 0.4 nm. Four temperatures (10, 20, 25, and 30 °C) are chosen to compare the results of the Langmuir-Hinshelwood model as shown in Figure 22. As expected, the rate constant k_{app} is steadily increasing with an increasing temperature. The activation energy for these gold nanoparticles is calculated to be E_A = 50 kJ mol^{-1} at standard concentrations (0.1 mM Nip, 10 mM BH_4^-).

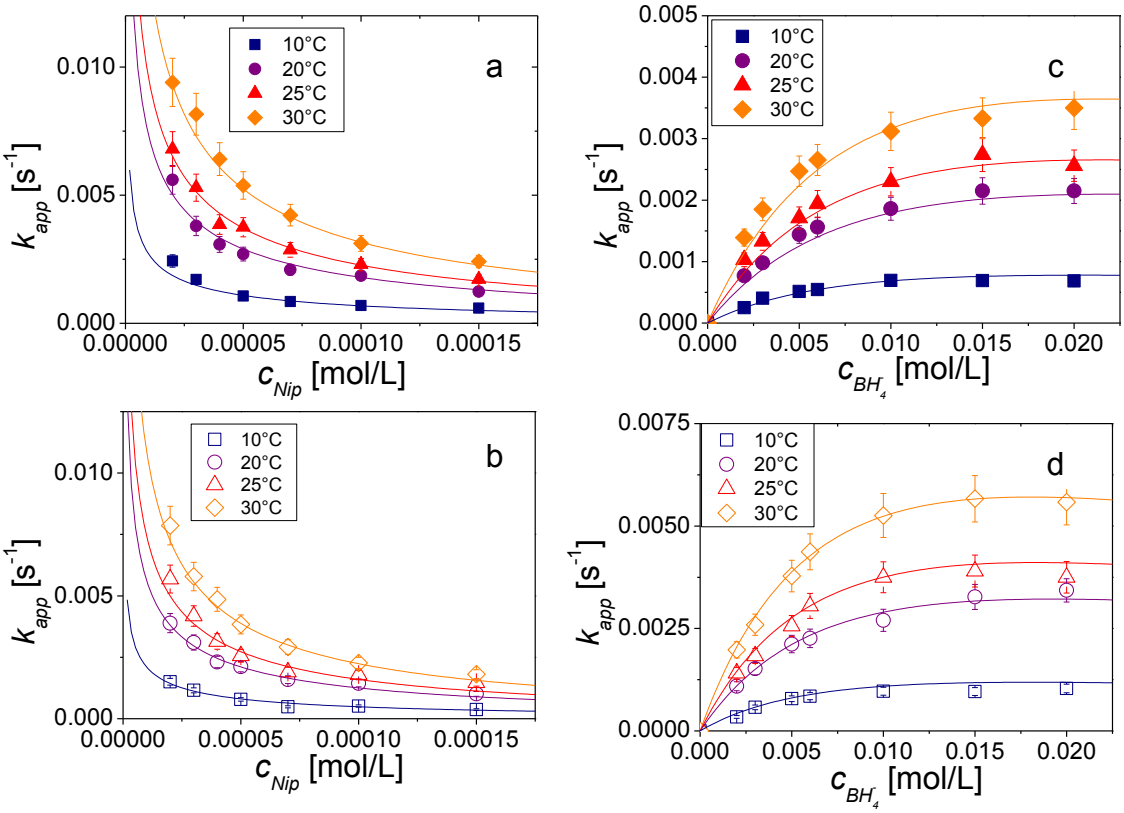

Figure 22: Dependence of the temperature on the rate constant at different concentrations of p-nitrophenol (a and b) and different concentrations of borohydride (c and d) for gold nanoparticles ($S = 0.0108\ m^2\ L^{-1}$). The temperatures are marked with 10 °C = blue squares; 20 °C = violet dots; 25 °C = red triangles; 30 °C = orange diamonds. The solid lines are the fits for the modified Langmuir-Hinshelwood model.

According to the Langmuir-Hinshelwood model the intrinsic rate constant k and the adsorption constants K_{Nip} and K_{BH4} can be determined for the different temperatures as shown in Figure 22. See Table 7 for a summary of the resulting parameters.

Table 7: Parameters of the modified Langmuir-Hinshelwood model for the gold nanoparticles in dependency of the temperature T of the intrinsic rate constant k, the adsorption constants K_{nip} and K_{BH4} and the Langmuir Freundlich constants n and m.

T [°C]	10	20	25	30
k [mol m^{-2} s^{-1}]	$(0.73 \pm 0.10)\cdot10^{-4}$	$(1.89 \pm 0.28)\cdot10^{-4}$	$(2.27 \pm 0.34)\cdot10^{-4}$	$(2.92 \pm 0.44)\cdot10^{-4}$
K_{Nip} [L mol^{-1}]	5300 ± 800	5900 ± 900	6400 ± 1000	7800 ± 1200
K_{BH4} [L mol^{-1}]	79 ± 12	76 ± 11	82 ± 12	87 ± 13
n	0.6 ± 0.1	0.6 ± 0.1	0.6 ± 0.1	0.6 ± 0.1
m	1 ± 0.1	1 ± 0.1	1 ± 0.1	1 ± 0.1

As a major tendency the intrinsic rate constant shall be mentioned, which is increasing with rising temperature. Another important result of the measurements is the increase of the adsorption constant of *p*-nitrophenol with temperature, whereas the adsorption constant of BH_4 is nearly independent of the temperature.

3.2.5 Thermodynamic Parameters

By analyzing the temperature dependence of the adsorption constants, the entropy and enthalpy of the adsorption process can be obtained applying the Van't Hoff equation (eq. 3.12).

$$\frac{d\ln K_i}{d\left(\frac{1}{T}\right)} = -\frac{\Delta H_i}{R} \qquad 3.12$$

$$\ln K_i = -\frac{\Delta G_i}{RT} = -\frac{\Delta H_i}{RT} + \frac{\Delta S_i}{R} \qquad 3.13$$

The respective Van't Hoff diagrams are shown in Figure 23 and the results are summarized in Table 8. Evaluating the obtained data, it has to be pointed out that the temperature dependence of *p*-nitrophenol reflects an endothermic adsorption process (Figure 23a). Furthermore, the adsorption entropy is positive, which implies an entropy-driven adsorption process. Here, the adsorption of *p*-nitrophenolate may displace adsorbed water molecules or other surface bound species from the nanoparticle surface, which is the reason for this positive adsorption entropy. In contrast, the adsorption of borohydride is nearly independent of the temperature. Nevertheless, the adsorption process of borohydride on metallic surfaces is a complicated process which involves several steps.[177, 178]

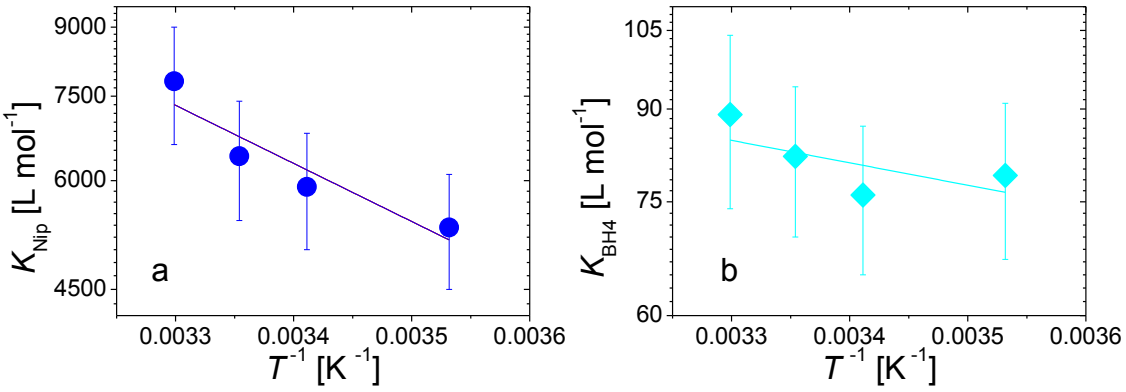

Figure 23: Dependence of the adsorption constant K_{Nip} of Nip (a) and the adsorption constant K_{BH4} of borohydride (b) on the inverse temperature. The enthalpies and entropies of the adsorption process were calculated using van't Hoff's equation (eq. 3.12, solid lines) and the results are listed in Table 8.

Table 8: Adsorption enthalpy and entropy derived calculated by equation 3.12 and 3.13 with the data shown in Figure 23.

	K_{Nip} [L mol^{-1}]	K_{BH4} [L mol^{-1}]
ΔH [kJ mol^{-1}]	13 ± 4	3.3 ± 2.6
ΔS [J mol^{-1} K^{-1}]	116 ± 11	46 ± 9

3.2.6 Compensation Plot

The intrinsic rate constant k is increasing with the temperature (see Table 7). Evaluation by the Arrhenius equation leads to the true activation energy of $E_{A,t}$ = 49 kJ mol^{-1}. The apparent rate constant k_{app} of gold nanoparticles at standard concentrations (c_{Nip} = 0.1 mM and c_{BH4} = 10 mM) exhibit approximately the same temperature dependence as k (with $E_{A,app}$ = 50 kJ mol^{-1}). However, the activation energy of k_{app} depends not only of the activation energy of the intrinsic rate but contains the temperature dependence of the adsorption constants, as well.

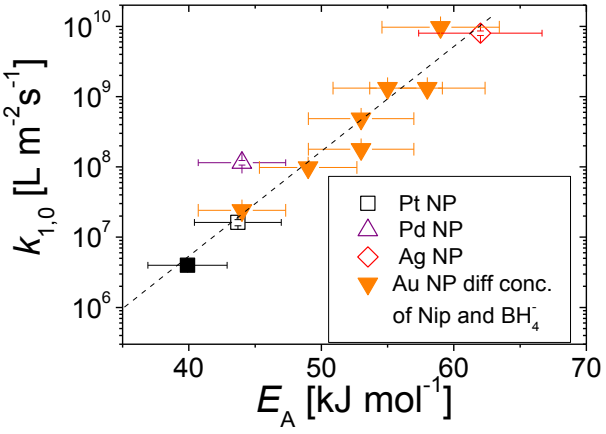

Figure 24: Compensation plot of different metallic nanoparticles confined in SPB carrier systems from literature (squares: Pt NP from Ref [58] (hollow) and Pt NP from Figure 21 (filled); up triangle: Pd NP;[56] diamond: Ag NP[126]) and from the results of some representative concentrations of p-nitrophenol and sodium borohydride for the Au NP, summarized in Table 9 (orange inverted triangles).

By analyzing the temperature dependence of different concentrations of *p*-nitrophenol and borohydride the dependence of the adsorption constants can be studied in more detail. In Table 9, the respective values of the activation energies and the pre-exponential factors k_0 of representative concentrations from the Langmuir-Hinshelwood analysis are listed. These apparent activation energies $E_{A,app}$ vary between 44 and 59 kJ mol^{-1}. A linear relation between the activation energies E_A and the pre-exponential factors k_0 is called a compensation plot. These values are shown in Figure 24 as orange inverted triangles. For different metallic nanoparticles embedded in SPB carriers, the activation energies fit to this linear dependency as seen in Figure 24. This leads to the conclusion that a similar process is responsible for all metal nanoparticles.

Table 9: Activation energies E_A of the surface normalized rate constants k_1 and the pre-exponential factor k_0 for different concentrations of Nip and BH_4^-.

c_{Nip} [mmo L^{-1}]	c_{BH4} [mmol L^{-1}]	E_A [kJ mol^{-1}]	$k_{1,0}$ [L m^{-2} s^{-1}]
0.02	5	55	$2.0 \cdot 10^9$
0.02	10	44	$1.5 \cdot 10^8$
0.05	2	58	$5.9 \cdot 10^9$
0.05	5	53	$1.5 \cdot 10^9$
0.05	10	59	$9.7 \cdot 10^9$
0.1	2	53	$5.4 \cdot 10^8$
0.1	10	49	$1.0 \cdot 10^8$

The activation energies available in the literature for this reaction are recalculated to obtain the pre-exponential factors. The recalculated values are listed in Table 28 in the appendix. A compensation plot is found, as well, in literature for different carrier systems as shown in Figure 25.

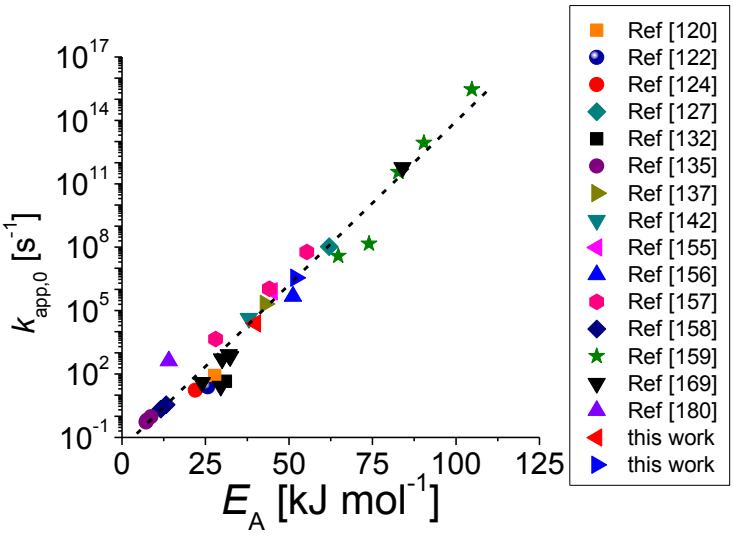

Figure 25: Compensation plot of the activation energy E_A and the pre-exponential factor $k_{app,o}$ as recalculated from literature values.[119, 121, 123, 126, 131, 134, 136, 141, 154-158, 168, 179]

Mahmoud *et al.*[158] suggested that the linearity of the compensation plot may be attributed to the reaction mechanism. He proposed that the reaction follows the same pathway independent of the applied metal surface. Zeng *et al.*[156] suggested a switching of the kinetic regime by studying different Au nanocubes. For Au nanocages with a high amount of active sites, the adsorption of the reduction product is more stable while the activation energy is relatively small. In contrast, for a nanostructure with less active sites (in this case a partially hollow structure) the adsorption of the reduction product is less favored, while the activation energy is higher. An overview of the reported systems is summarized in Figure 25 as a compensation plot.

As already described in chapter 3.1 the linear dependence of the activation energy on the rate can be described with:[159]

$$\ln k_0 = p \cdot E_A + q \qquad 3.6$$

This kind of compensation has been reported for different catalytic reactions. There are different explanations for such kind of phenomena. It has been suggested that the reaction must share certain features if the data points can be combined to a single compensation line.[159] They might share the same mechanism or use the same type of active centers or have the same fraction of surface atoms.

A more theoretical approach is the enthalpy-entropy relation.[159, 160] It is based on the fact that the equilibrium constant can be divided in the temperature-dependent part ($\Delta H°$) and the temperature-independent part ($\Delta S°$). This is applied to a quasi-equilibrium between reactants and a transition state or an activated complex as postulated by the transient state theory. By employing the corresponding parameters of activation (e.g. $\Delta H^{\ddagger}$, $\Delta S^{\ddagger}$, and $\Delta G^{\ddagger}$), the rate constant is given by:

$$k = \frac{k_B T}{h} K^{\ddagger} \tag{3.14}$$

$$K^{\ddagger} = exp\left(\frac{\Delta S^{\ddagger}}{R}\right) exp\left(-\frac{\Delta H^{\ddagger}}{RT}\right) \tag{3.15}$$

$$k = \left(\frac{k_B T}{h}\right) exp\left(\frac{\Delta S^{\ddagger}}{R}\right) exp\left(-\frac{\Delta H^{\ddagger}}{RT}\right) \tag{3.16}$$

where $K^{\ddagger}$ is the equilibrium constant, $\Delta H^{\ddagger}$ equals the zero-point energy change. Therefore the pre-exponential factor is influenced by $\Delta S^{\ddagger}$ whereas the activation energy is dependent on $\Delta H^{\ddagger}$. This concept is hard to prove and in this work it cannot be confirmed by the analysis of the experimental data.

Another ansatz is the switching of kinetic regimes as Zeng *et al*.[156] suggested for the gold nanostructures. According to Bligaard *et al*. [163] the finding of a compensation can be attributed to a correlation between the activation energy of the rate limiting step and the stability of the reaction intermediates. Here, the switching of a regime, where the rate is dominated by the activation of the reactant, to a regime where the rate is dominated by the stability of the reaction intermediates on the surface might be another explanation for the finding of a compensation plot.

A further explanation is the concept of apparent and true activation energies.[159, 161, 162] Here, the surface coverage is the reason for the found compensation plot: the compensation is a result from employing the apparent rate for the calculation of the activation energy ($E_{A,app}$). The true activation energy ($E_{A,t}$) varies from the apparent one because of the

varying concentrations of the reactants on the surface. At a complete coverage of the surface, E_{app} is equal to $E_{A,t}$, at a low coverage both should deviate according to:

$$E_{A,t} = E_{A,app} - \sum b_i \Delta H_i \qquad 3.17$$

with the reaction order b_i and ΔH_i the adsorption enthalpy.

The attempts to explain the reason behind the compensation plots differ a lot. To figure out which of the listed reasons are appropriate for the reduction of *p*-nitrophenol, the influence of surface coverage was tested. Therefore, the rate constants k_1 for different temperatures at constant coverage of *p*-nitrophenol are calculated. Here, the concentration is slightly varied, so that the coverage for all temperatures is the same. In case of the borohydride, the coverage hardly changes with the temperature. Therefore the concentration is not aligned. In Figure 26, these calculated values are shown together with the intrinsic rate constant k from the Langmuir-Hinshelwood analysis.

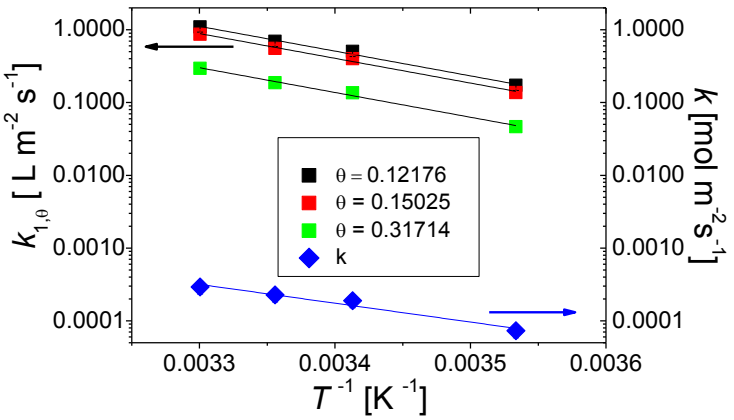

Figure 26: Dependence of the intrinsic reaction rate k (blue diamonds) and the calculated rate constants with a constant coverage of p-nitrophenol (squares) on inverse temperature.

The activation energies for these calculated coverages are lying all within the same range of approximately $E_A = 60$ kJ mol^{-1}, but the pre-exponential factors deviate. The intrinsic rate constant has an activation energy of $E_A = 49$ kJ mol^{-1}. The adsorption enthalpy of the *p*-nitrophenol is 13 kJ mol^{-1}. Considering equation 3.17, the apparent activation energy of approximately 60 kJ mol^{-1} is expected for the different coverages of *p*-nitrophenol. Thus, the

varying coverages at different temperatures are accountable for the compensation behavior of this reaction.

Regarding the results shown in Figure 24, a compensation plot is obtained for the same nanoparticles at the same reaction conditions only with different concentrations of the educts. Therefore, using the same nanoparticles, the active sites of the nanoparticles are expected to be the same. The switching of the kinetic regime is mostly used for comparison of different catalysts. Thus the application of the apparent activation energy is most likely the reason for the found compensation effect in this work.

Considering the adsorption of the educts on the surface, there appear two limiting cases for this analysis: Firstly, high concentrations of both educts lead to a saturation of the surface of the nanoparticles and the influence of the adsorption terms will be negligible. The activation energy is then dominated by the intrinsic activation energy of k. Secondly, at very low concentrations, the adsorption of the educts must be taken into account. Hence, the measured activation energy is altered by the adsorption enthalpy and the pre-exponential factor by the adsorption entropy of the educts. In the present case, the values for the enthalpy and entropy are both positive. Therefore, the apparent activation energy and the pre-exponential factor should increase if the surface is not completely covered. The relation between the true and the apparent activation energy by the heat of adsorption as discussed by Bond [134, 135, 162] seems to be a good explanation in this case.

3.2.7 Induction Time

Another observation of interest in this reaction is the induction time, which can take up to several minutes. The induction time observed by different authors (see chapter 3.1.3) was sometimes attributed to the time the educts require to diffuse to the nanoparticles or to the adsorption time.[169-171, 180] But by calculating the Damköhler number II (see equation 2.25, chapter 2.2.4 and 3.2.2), it appears impossible that the diffusion of small educts through the polyelectrolyte brush system should take minutes.

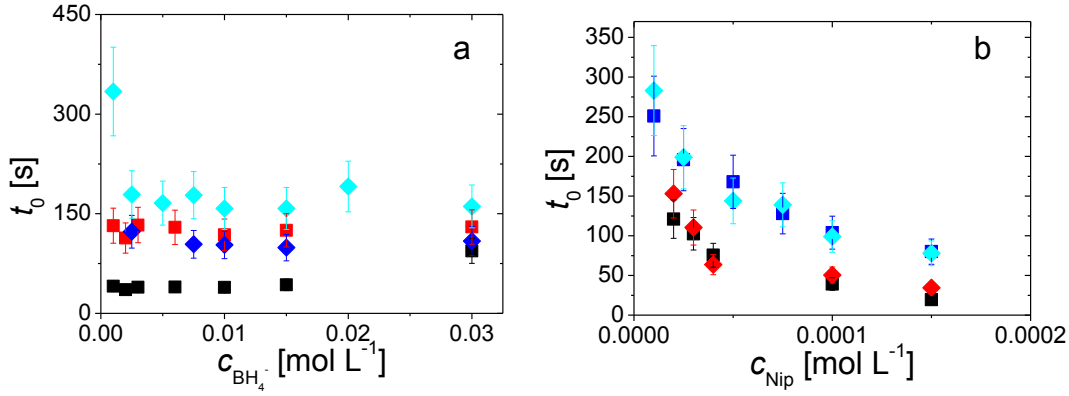

Figure 27: Dependence of the induction time on the concentration of borohydride (a) squares: 0.1 mM Nip, diamonds: 0.05 mM Nip; black/red for platinum nanoparticles, dark/light blue for gold nanoparticles and dependence on p-nitrophenol (b) squares: 10 mM BH_4^-, diamonds: 5 mM BH_4^-; black/red for platinum nanoparticles, dark/light blue for gold nanoparticles.

The induction times for the different concentrations of borohydride and *p*-nitrophenol are summarized in Figure 27. Noticeably, the induction time is nearly independent of the concentration of borohydride (Figure 27a). This excludes that the induction time is related to any reaction involving borohydride, e.g. the transfer of a surface hydrogen species to the surface. In contrast, the induction time is dependent on the concentration of *p*-nitrophenol (Figure 27b). Moreover, the type of metal migth be of influence since the induction times extents when using Au instead of Pt.

As mentioned above, the inverse induction time has approximatly the same activation energy as the rate constant, which is in good agreement with previous works.[44, 56, 58, 126] A similar behavior was found by Zhan *et al.*[181] for the catalytic hydrolysis of borohydride on ruthenium catalysts. Consequently, the inverse induction time will be treated as a reaction rate. By normalizing this "rate" $1/t_o$ with the total surface area and the intrinsic rate constant from the Langmuir-Hinshelwood model, a linear behaviour is obtained when plotted versus the concentration of *p*-nitrophneol as shown in Figure 28. Here, a master curve is achieved, which leads to the conclusion that the induction time is coupled with the *p*-nitrophenol reduction. This suggests that the inverse induction time is related to a slow surface reconstruction which is related to the rate of the stationary surface reaction.

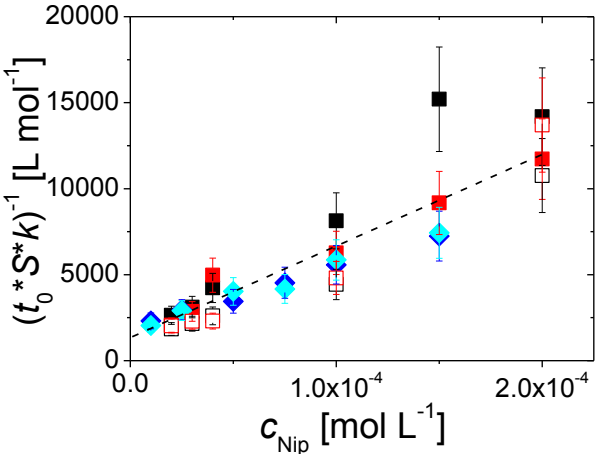

Figure 28: Dependence of the inverse normalized rate constant on the concentration of Nip (black and dark blue for 10 mM borohydride, red and light blue for 5 mM borohydride; with two different concentration of Pt NP: S = 0.00687m²L⁻¹ (filled squares) open squares for Pt NP with S = 0.00481 m² L⁻¹ (open squares); diamonds for gold nanoparticles S = 0.01078 m² L⁻¹.

A relation of the reaction rate and a surface reconstruction was found by Zhou *et al.*[175] for the reduction of resazurin to resorufin by hydroxylamine over single gold nanoparticle via single-molecule fluorescence microscopy. By calculating the turnover trajectories of this catalytic reaction, they found that the activity of one single nanoparticle fluctuated with time. This was attributed to catalysis-induced surface restructuring, which takes place in a time scale in the order of minutes. Furthermore, the restructuring can be different for individual nanoparticles. The authors could show that this restructuring is directly related to the rate of the surface reaction. Additionally, by correlating the rate of surface restructuring with the catalytic turnover, they found a possitive intercept. This was attributed to a spontaneous surface restructuring, corresponding to a time in the range of ten to hundreds of seconds. Noticeably, this spontaneous process was more pronounced for smaller nanoparticles, indicating a faster spontaneous dynamic surface restructuring. These findings can be directly compared to Figure 28 and Figure 29b. Here, a small but noticeable intercept is visible in the absence of *p*-nitrophenol. Therefore, a surface restructuring appears to be a plausible explanation for the induction period and the relation of t_0 to the reaction rate of the reduction. The nature of this restructuring is not yet clear. It may be a shift of single atoms or a concerted rearrangment of surface atoms due to the adsorption of *p*-nitrophenol.

3.2.8 Kinetic of the Surface Restructuring

By analyzing the temperature dependence of the induction time for gold nanoparticles with a size of 2.2 nm, it is evident that this time is shorter for higher temperatures. In Figure 29 the dependence of the induction time on the concentration of BH_4^- (a) and Nip (b) are shown for different temperatures. It is found that the induction time is independent of the concentration of borohydride as shown previously, but the inverse induction time has a nearly linear dependence on the concentration of *p*-nitrophenol for all temperatures. As discussed above, this can be interpreted as a surface restructuring due to adsorption of Nip which is a necessary step to activate the surface. Furthermore, there is an intercept visible at $c_{Nip} = 0$ mM, which can be attributed to a spontaneous surface reconstruction.

Surface reconstruction is a phenomenon which occurs at crystal surfaces (see chapter 2.2.5). The topmost layer of atoms rearranges to reduce the surface tension which then varies from the bulk structure. The lifting of the reconstruction or restructuring is the return to the bulk-like structure due to adsorption of adsorbates.[105]

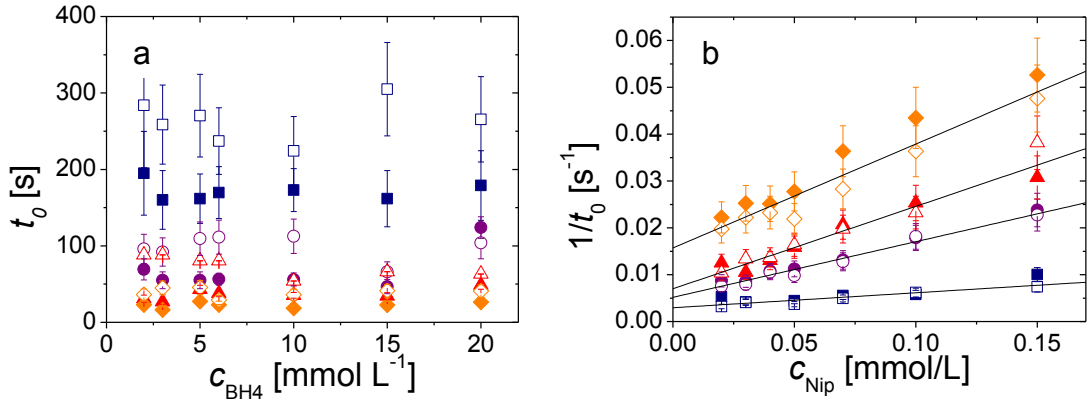

Figure 29: Dependence of the induction time on the concentration of the initial concentration of BH_4 at 0.1 mM (closed symbols) and 0.05 mM Nip (open symbols) (a) and of p-nitrophenol at 10 mM (closed symbols) and 5 mM BH_4^- (open symbols) (b) at four different temperatures. The temperatures are symbolized as following: 10 °C = blue squares; 20 °C = violet dots; 25 °C = red triangles; 30 °C = orange diamonds for gold nanoparticles with 2.2 nm size.

Measuring at different temperatures allows the calculation of the activation energy of this spontaneous surface reconstruction derived from the intercept in Figure 29b. The value of the activation energy obtained by Figure 30 is $E_A = 55$ kJ mol^{-1}.

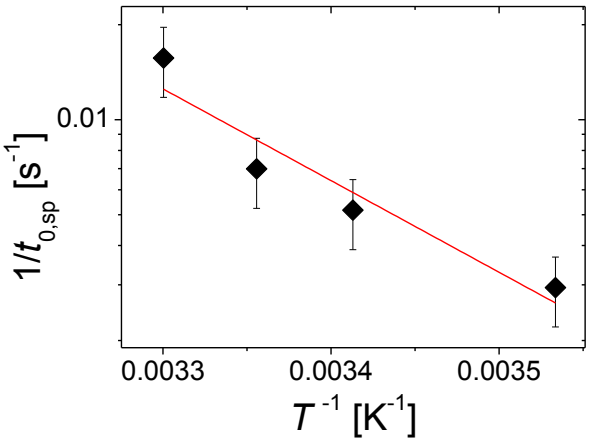

Figure 30: Temperature dependence of the inverse spontaneous induction time for gold nanoparticles at c_{Nip} = 0 mol L^{-1} derived from the intercept in Figure 29b.

By subtracting the intercept, representing the spontaneous surface reconstruction from the inverse induction time, the substrate induced surface restructuring is obtained. As the surface restructuring clearly depends solely on the concentration of *p*-nitrophenol (Figure 29), in the next step the dependency of the surface coverage of *p*-nitrophenol is studied as shown in Figure 31. In this double logarithmic plot, a power law coefficient of approximately 2 is found for all different concentrations of BH_4^- and temperatures.

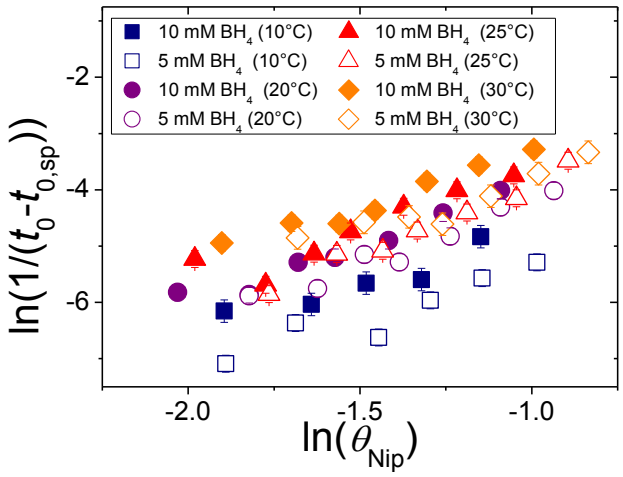

Figure 31: Double logarithmic plot of the surface restructuring rate and the surface coverage of p-nitrophenol. Filled symbols represent 10 mM and open symbols 5 mM borohydride. The different temperatures are marked as follows: blue squares: 10 °C; violet dots: 20 °C; red triangles: 25 °C, and orange diamonds: 30 °C for gold nanoparticles with 2.2 nm size.

This is additionally visualized in Figure 32. Here, the restructuring rate is normalized with the intrinsic rate constant from the Langmuir-Hinshelwood kinetic. Thereby, a master curve for the concentration of 10 mM (Figure 32a) and 5 mM of borohydride (Figure 32b) is obtained as well. This implies the same temperature behavior for the induction time and the intrinsic rate constant.

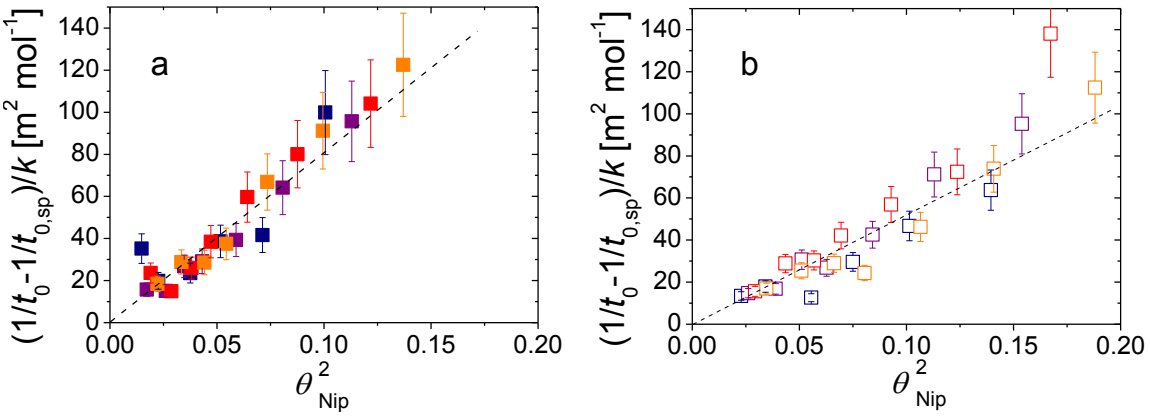

Figure 32: Relation of the substrate induced surface restructuring of the p-nitrophenol covered surface at a) 10 mM and b) 5 mM borohydride. The temperatures are marked with: blue: 10 °C; violet: 20 °C; red 25 °C, and orange: 30 °C for gold nanoparticles with 2.2 nm.

This confirms that the surface restructuring is solely related to the concentration of *p*-nitrophenol on the surface of the nanoparticles. Due to the quadratic dependence on the surface coverage of *p*-nitrophenol as shown in Figure 32 it can be suggested that two or more molecules must act concerted to start this surface restructuring. This behavior is well-known in catalysis (chapter 2.2.5). A thoroughly study provided by King and coworkers showed that the reconstruction of the platinum (100) surface can be lifted by CO and H_2 adsorption. This lifting of the reconstruction follows a nonlinear power law with a reaction order of approximately 4.5. Therefore, four till five adsorbed molecules are involved in the restructuring step leading to the nonlinear growth dependence of the restructured surface.[108, 109]

Later van Beurden and coworkers [110, 111] used atomistic simulations (density functional theory and molecular dynamics simulation) to determine both the surface reconstruction of the Pt (100) surface and the restructuring by adsorbed CO molecules. They conclude that the surface reconstruction is predominantly homogenously nucleated. The restructuring process starts heterogeneously at linear defects and exhibit an effective activation energy of

$E_A = 42.4 \pm 9.6$ kJ mol^{-1}. A homogeneously nucleated process is also possible but requires a higher activation energy. Furthermore, a nonlinear growth rate of the restructured surface depending on the surface coverage is found in the simulated restructuring process. Here, the reaction order was $\nu = 7.5 \pm 2.5$ but no local clustering of CO molecules were found. The adsorbed CO molecules initiate a surface relaxation and shear tension between the topmost layers of Pt atoms. Thereby, the entire concentration of CO molecules in the vicinity of the critical area is involved.[110, 111]

The reconstruction of gold surfaces can be lifted by adsorbates as well. Driver *et al.* found a massively cooperating restructuring process for the lifting of the reconstruction which involves adsorbed NO. Once the adsorbed NO islands reaches a certain size, the restructuring occurs in a domino-like fashion.[182] Another example is the lifting of the reconstruction of gold surfaces by adsorbed CO molecules as shown by Pierce *et al.*.[183] It was suggested that the restructuring rate is dependent on the amount of adsorbed CO molecules. They assumed that the restructuring of the Au surface progressed in a similar fashion to the restructuring of Pt(100), and that this is a result of two processes: I) the CO adsorption and II) the adsorption initiated reconstruction of the surface.[183]

As mentioned before, in the study of Zhou *et al*. [175], the reactivity of gold nanoparticles fluctuates which was explained by dynamic surface restructuring. The restructuring rate showed a strong dependency on the nanoparticle size and the turnover rate.[175]

This data confirms that surface restructuring is a common incidence on catalyst surfaces. The induction time can be interpreted as the time for a surface restructuring process which activates the metallic nanoparticles. The reduction of *p*-nitrophenol does not proceed without this restructuring step. Furthermore, the surface restructuring can be traced back solely to the adsorption of *p*-nitrophenol onto the surface of the nanoparticles. In addition the restructuring appears to be a cooperative process involving several *p*-nitrophenol molecules. Most likely the adsorption of several *p*-nitrophenol molecules in close vicinity allows the surface of the nanoparticles to overcome the disadvantage of a non-reconstructed surface. Hence, this restructured surface is thermodynamically favored with the adsorbed *p*-nitrophenol. In analogy to the reaction of CO with O_2 on the restructured platinum surface (see chapter 2.2.5), the reduction of *p*-nitrophenol with borohydride can only proceed on the restructured surface. In contrary to the reaction Ertl *et al*.[106] measured in high vacuum, the reaction in the

present case takes place in water. Therefore the nanoparticles have a different surrounding, a shell of water and the SPB, which may have an influence on the restructuring process.

In summary, the reduction of *p*-nitrophenol follows a Langmuir-Hinshelwood-type kinetic, where both educts adsorb onto the surface of the nanoparticles. By measuring at different temperatures the adsorption enthalpy and entropy as well as the activation energies could be obtained. Furthermore a reason for the induction time is found, which is mainly caused by the surface restructuring of the nanoparticles.

3.3 Catalysis by Manganese Oxides

Another class of reactions is studied in this work, namely, the oxidation of organic dyes. Contrary to the already studied reduction reaction, the kinetics of an oxidation is investigated to determine, if the Langmuir-Hinshelwood ansatz is furthermore valid for oxidation reactions. An important group of oxidation catalysts are manganese oxides. Manganese oxide nanoparticles are chosen very often as a general oxidation catalyst due to the fact that they can be applied for various oxidation reactions.[67, 184-188] In order to verify the activity of different oxidation catalysts, flavonoid-systems are frequently used as model substances.[83] Thereby, a detailed kinetic study of the oxidation process is important for the comparison of different catalysts and possible improvements of these catalyst systems.

3.4 Literature Survey for the Oxidation of Morin

The oxidation of flavonols, e.g. morin or quercetin, can be applied as a model for catalytic bleaching test due to the fact that their chromophores are often targets in the bleaching of laundry.[82] A frequently analyzed flavonol is quercetin.[86-89] Quercetin can be oxidized by oxidases,[88] enzymes, radicals, or electrochemical reactions.[87] The products are varying for the different reactions as shown in the comparative study of Zhou *et al.*[87] It is worth noting that two main products of quercetin in all oxidation reactions are 3,4-dihydroxy benzoic acid and 2,4,6-trihydroxy benzoic acid. However, a side reaction is possible as well: the dimerization of quercetin. Here, the OH groups at the 3' and 4' position interact with the C-atoms in 2 and 3 position.[87, 88]

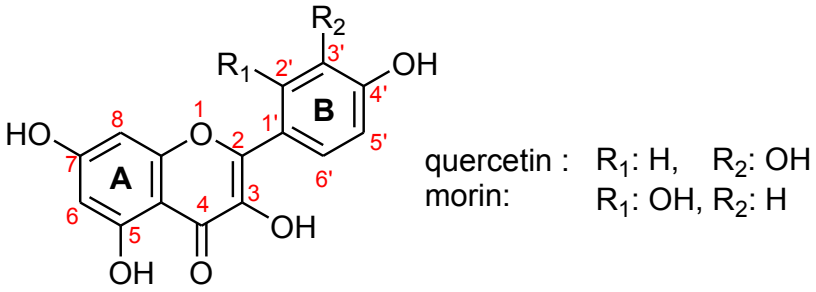

Scheme 8: Chemical formula of quercetin and morin.

The knowledge of the oxidation pathways of morin, used in this work, is not as detailed as these of quercetin. Osman *et al.*[85] described the reaction mechanism of the oxidation of

morin with an onion peroxidase. It bears similar reaction pathways as the oxidation of quercetin.[88] Unlike quercetin, morin cannot dimerize due to the ortho-position of the OH group R_1 (Scheme 8), which makes morin more suitable for kinetic studies. Furthermore, the two final products are 2,4-dihydroxy benzoic acid and 2,4,6-trihydroxy benzoic acid.[84, 85] Colombini *et al*.[84] suggested a degradation pathway of morin by manganese ions as shown in Figure 33.

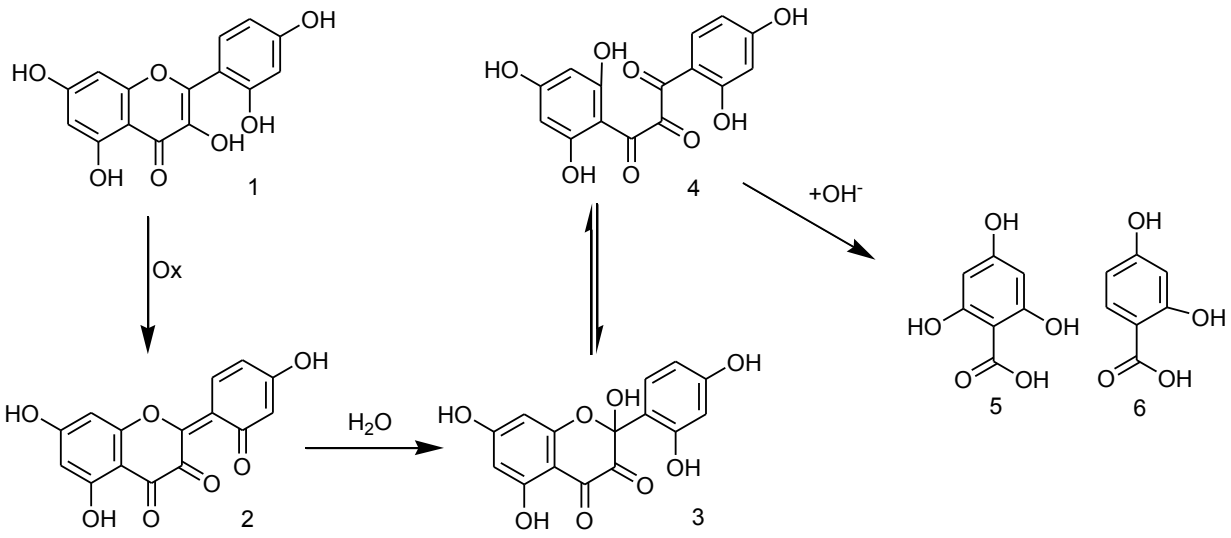

Figure 33: Decomposition of morin to 2,4-dihydroxy benzoic acid and 2,4,6-trihydroxy benzoic acid by a nucleophilic attack in 2-position and ring opening as proposed by Colombini et al..[84]

Topalovic [189] studied the oxidation of morin by air oxygen with manganese complexes containing 1,4,7-trimethyl-1,4,7-triazacyclononane (TMTACN). The main reaction product is 2-(hydroxybenzoyl)-2-hydroxybenzofuran-3(2H)-on as shown in Figure 34. This compound can be derived from the reaction intermediate **4** from Figure 33 by ring closure.

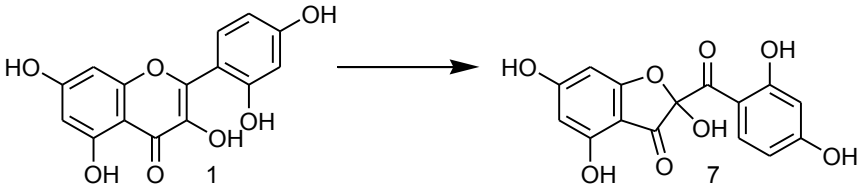

Figure 34: Proposed reaction product of the oxidation of morin by Topalovic [189].

By comparing morin with other flavones, Topalovic *et al*.[190] ascertained that the hydroxyl-group at the C3-position has a main influence on the reactivity of morin. They concluded that this OH-group anchors the B-ring of morin. Therefore, the angle of torsion

between the two rings is 0°. Without a OH-group, the angle of torsion is 20° and the oxidation is slower.[190]

Manganese-II-complexes derived from the ligand TMTACN or 2,2';6',2"-terpyridine are good catalysts for oxidations.[82, 190] They show a high catalytic activity for various substrates e.g. oxidation of phenols and azo-dyes, epoxidation and dihydroxylation of alkenes.[82] Moreover, these systems are active in bleaching reactions, as commonly known, which are used in detergent applications. Thereby, a pH-value between 9 and 11 is often applied and the employed oxidizing reactant is commonly hydrogen peroxide.[82]

Furthermore, the catalytic properties of Mn-(II)-complexes were investigated by the group of van Eldik.[191, 192] The oxidations of different dye systems, including morin, were studied with H_2O_2 and the influence of pH-values and buffer concentrations were analyzed. They found that an increase of the carbonate buffer concentration leads to a remarkable increase in the reaction rate as shown in Figure 35.[192]

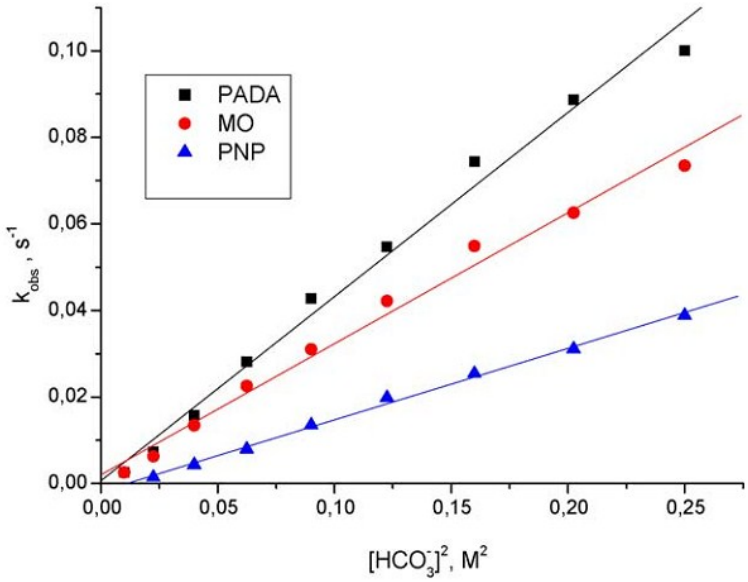

Figure 35: Second-order bicarbonate dependence on the oxidation of different dyes (PADA: trans-pyridine-azo-p-dimethylanilin, MO: morin, PNP: p-nitrophenol). Experimental conditions: $Mn(NO_3)_2$: 0.02 mmol L^{-1}, dye: 0.05 mmol L^{-1}, H_2O_2: 0.01 mol L^{-1}at a pH-value of 8.5 at 25 °C. Repinted from ref [192]. Copyright 2010 with permission from Elsevier.

This was explained by the formation of peroxocarbonate ions, which are far more reactive than the hydrogen peroxide itself and by the formation of a complex of the manganese (II) and the carbonate. Furthermore, the optimal pH-value was approximately 8.5. An increase in the pH leads to a decrease in the catalytic activity due to the fact that the equilibrium of

bicarbonate and carbonate in solution is pH dependent. At a higher pH-value less bicarbonate is in solution.

3.4.1 Decomposition of H_2O_2 Catalyzed by Manganese Oxides

Besides the homogeneous catalysis, manganese oxide particles can be used in heterogeneous catalysis as well. For example, manganese oxides are able to decompose H_2O_2.[73, 74, 193] In the study of Zhou *et al.*[193] the decomposition of H_2O_2 was modeled with a Langmuir-Hinshelwood kinetics assuming a Langmuir adsorption isotherm on the Lewis acid sites of manganese oxide inside octahedral molecular sieves. It was assumed that hydrogen peroxide adsorbs onto the surface of the octahedral molecular sieves, and decomposes to water and a surface oxygen species. Subsequently, two of these surface oxides can combine to form oxygen. A more detailed study of the decomposition of H_2O_2 was done by Do *et al.*[74] in order to analyze the formation of oxygen. The authors claim that H_2O_2 decomposes on the surface in various ways, leading to the formation of surface hydroxides and surface bound peroxides. These intermediates can further react with H_2O_2 or hydroperoxides to form water and oxygen. The reaction pathways of the H_2O_2 decomposition on manganese oxide ([≡Mn-O]) are shown in the following:

$$[\equiv Mn\text{-}O] + H_2O_2 \rightarrow [\equiv Mn\text{-}O]H + OOH^- \quad 3.18$$

$$[\equiv Mn\text{-}O]H + H_2O_2 \rightarrow [\equiv Mn\text{-}O]OH + H_2O \quad 3.19$$

$$[\equiv Mn\text{-}O] + H_2O_2 \rightarrow [\equiv Mn\text{-}O]O + H_2O \quad 3.20$$

$$2[\equiv Mn\text{-}O]O \rightarrow 2[\equiv Mn\text{-}O] + O_2 \quad 3.21$$

$$[\equiv Mn\text{-}O]O + H_2O_2 \rightarrow [\equiv Mn\text{-}O]OH + OOH^- \quad 3.22$$

$$[\equiv Mn\text{-}O]OH + H_2O_2 \rightarrow [\equiv Mn\text{-}O] + H_2O + {}^{\bullet}O_2^- \quad 3.23$$

$$[\equiv Mn\text{-}O]OH + H_2O_2 \rightarrow [\equiv Mn\text{-}O]OH\text{-}\ H_2O_2 \rightarrow [\equiv Mn\text{-}O] + {}^{\bullet}OOH + H_2O \quad 3.24$$

First H_2O_2 adsorbs onto the manganese oxide surface before it decomposes. For oxidation reactions, the surface bound oxide species peroxide (eq. 3.20) or hydroperoxides (eq. 3.19) may play a major role. Both can be reduced to water by accepting electrons and protons. The consumed electrons can be transferred from the substance which is oxidized, the necessary protons may be transferred from there via surrounding water.

Furthermore, the authors analyzed the pH dependence of this reaction. At a pH-value of 3 or 7 the decomposition of H_2O_2 is very slow. At a pH-value of 9 the decomposition of H_2O_2 is increased. Noticeably, the overall production of oxygen is nearly constant independent of the pH-value. The leaching of manganese is 5 ppm at a pH 7 and only 1 ppm at a pH 9.[74]

3.4.2 Oxidation Reactions Catalyzed by Manganese Oxides

The surface bound oxygen, which is generated from H_2O_2, can be utilized for oxidation reactions. As shown by Qui *et al*.,[187] manganese oxides are active in epoxidation reactions of various alkenes like styrene, α-methylstyrene, indene, or 1-phenylcyclohexene. Remarkable is the fact that the activity of the oxidizing reagent arises from the peroxocarbonate rather than H_2O_2 (see Figure 36). The leaching of manganese in solution was measured by inductively coupled plasma-atomic emission spectrometry (ICP-AES) to be 1.7 ppm. Furthermore, reuse studies show only a small decrease in the catalytic activity. The authors claim that the recovered catalyst was unchanged after the reactions.

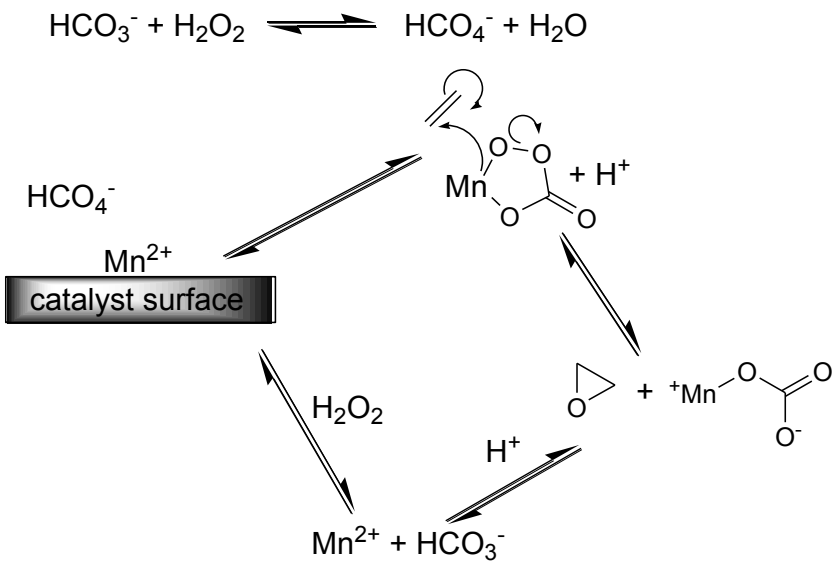

Figure 36: Proposed reaction pathway of the selective epoxidation of alkenes redrawn according to Ref [187]. Mn^{2+} exists on the surface of the MnO-catalysts, which can be coordinated by HCO_4^- on the surface of the catalyst. This intermediate can transfer active atomic oxygen to the C-C-double bond of the alkene and decompose to Mn^{2+} on the surface of the catalyst and CO_3^-.[187]

Styrene epoxidation was analyzed by Espinal *et al.*[188] with octahedral layered manganese oxide (OL) on a carbon electrode. The authors proposed the following reaction mechanism for this catalyst:

$$OL + H_2O_2 \rightarrow O\text{-}OL + H_2O \quad 3.25$$

$$OL + H_2O_2 \rightarrow 1/2\ O_2 + OL + H_2O \quad 3.26$$

$$O\text{-}OL + 1e^- + ArHC{=}CH_2 \rightarrow OL^* + ArHC^{\text{-O-}}CH_2 \quad 3.27$$

$$2\ OL^* + O_2 \rightarrow 2\ O\text{-}OL \quad 3.28$$

They could show that the oxidation of styrene is promoted by adding H_2O_2 to the solution. At high concentrations of H_2O_2 the oxygen is transferred from the hydrogen peroxide, whereas at low concentrations the oxygen is transferred from both O_2 and H_2O_2. Furthermore, the involvement of a superoxide anion in the epoxidation step can be excluded due to the fact that adding superoxide dismutase did not influence the amount of produced styrene oxide.

Manganese oxide catalysts could also oxidize dye systems like methylene blue as shown by Zhang *et al.*[184] The authors propose a reaction mechanism which involves the adsorption of the dye and H_2O_2. The stability of the catalyst was proven by reusing the catalyst after centrifugation. After five runs no noticeably change in the activity was found.

3.5 Oxidation of Morin using SPB-MnO_x as Catalyst

In this study, manganese oxide nanoparticles were used as catalyst for the oxidation of morin. Spherical polyelectrolyte brushes can be employed as carrier systems for manganese oxide nanoparticles as depicted in Figure 37. The manganese oxide is formed inside of these carriers as a thin platelet-like form. The synthesis of this composite catalyst system consists of an *in situ* reduction of $KMnO_4$ in the presence of polymeric brushes to the manganese oxide platelets (MnO_x), which have been confirmed to be of the c-disordered K^+-birnessite type.[62]

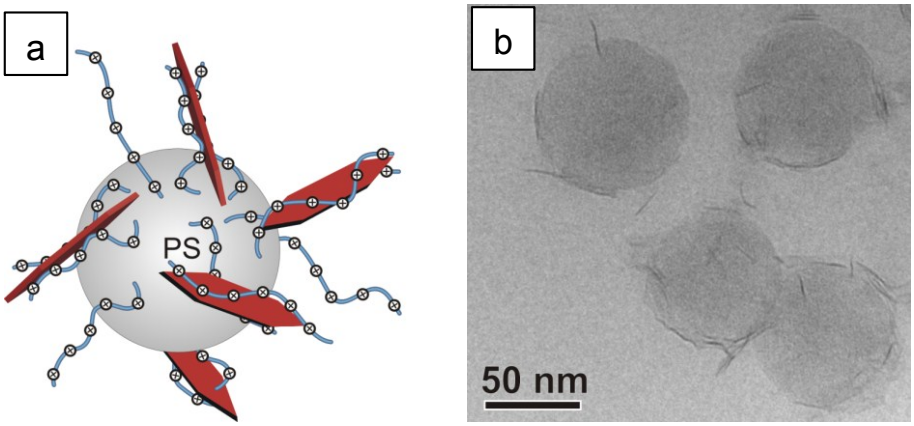

Figure 37: a) Scheme of the manganese oxide containing SPB, the red hexagons symbolizes the platelets of MnO_x NP embedded inside the polyelectrolyte layer. b) Cryo-TEM image of these composite particles, where the platelets of MnO_x NP are wrapped around the dark grey PS core of the SPB.[194]

3.5.1 The UV-vis Spectrum of Morin

The catalytic oxidation reactions are carried out in a carbonate buffered solution with a pH-value of 10. The spectra of the oxidation of morin can be easily followed by UV-vis measurements as shown in Figure 38. There are three distinctive peaks visible at 275 nm, 310 nm and 410 nm. In general, two major absorption bands are observed in flavonoid systems: One can be attributed to the cinamoyl moiety (300 - 400 nm) and the other can be assigned to the benzoyl moiety (around 270 nm).[90] In a basic environment, these absorption bands shift and the band around 270 nm splits into two separate peaks. Therefore, in the present case, peak I and peak II correspond to the benzoyl moiety, peak III to the cinamoyl moiety.[90] By addition of H_2O_2 to morin without the catalyst no visible change in the spectra is observed over time. Thus, no oxidation of morin occurs. Only after adding a certain amount of MnO_x containing SPBs (MnO_x@SPB) to this solution, the oxidation of morin can be detected. During the catalytic oxidation, the peaks I and III are decreasing, peak II is first increasing and after some time decreasing (Figure 38b). This behavior points to a further decomposition of the first oxidation product of morin. Nevertheless, isosbestic points are visible in the early stage of the oxidation while peak II is increasing. Therefore, only the first few minutes are taken into account in order to evaluate the rate constant of the reaction und only the first oxidation step of the decomposition of morin is analyzed.

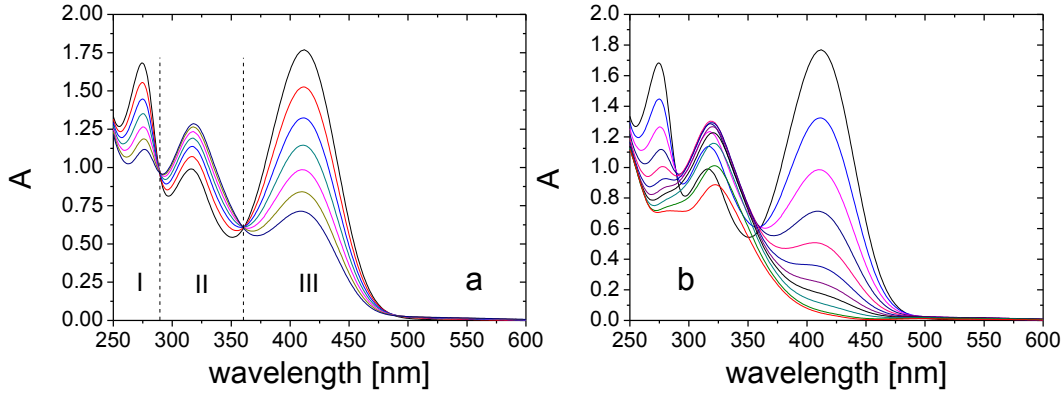

Figure 38: a) Spectra of the first 12 minutes of the oxidation of morin by H_2O_2 on K^+-birnessite nanoparticles, where the isosbestic points are clearly visible. These points are marked by dashed lines. The time between the spectra is two minutes. b) Spectra over the whole reaction time of about one hour; the spectra are taken each 4 minutes. The reaction conditions are: 10 mg L^{-1} MnO_x@SPB, 10 mM H_2O_2, 0.1 mM morin in 50 mM carbonate buffer solution.

As shown in Figure 38 the baseline increases at lower wavelength, which makes difficulties for the kinetic analysis of the three peaks, even when applying MnO_x and H_2O_2 in carbonate buffer for calibration. Thus, the UV-vis spectrum at a reaction time of 58 min is used for background subtraction as the main peak at 410 nm has already vanished at this time. The resulting spectra are shown in Figure 39a. Normalizing the absorption (Figure 39c and d) it is obvious that the decrease of the peaks I and III is in the same time scale, but peak II increases and decreases in a different rate. Peak II at approximately 310 nm is difficult to evaluate because the maximum shifts to higher wavelengths during the reaction. This leads to the conclusion that the oxidation of morin could be evaluated after this normalization with peaks I and III.

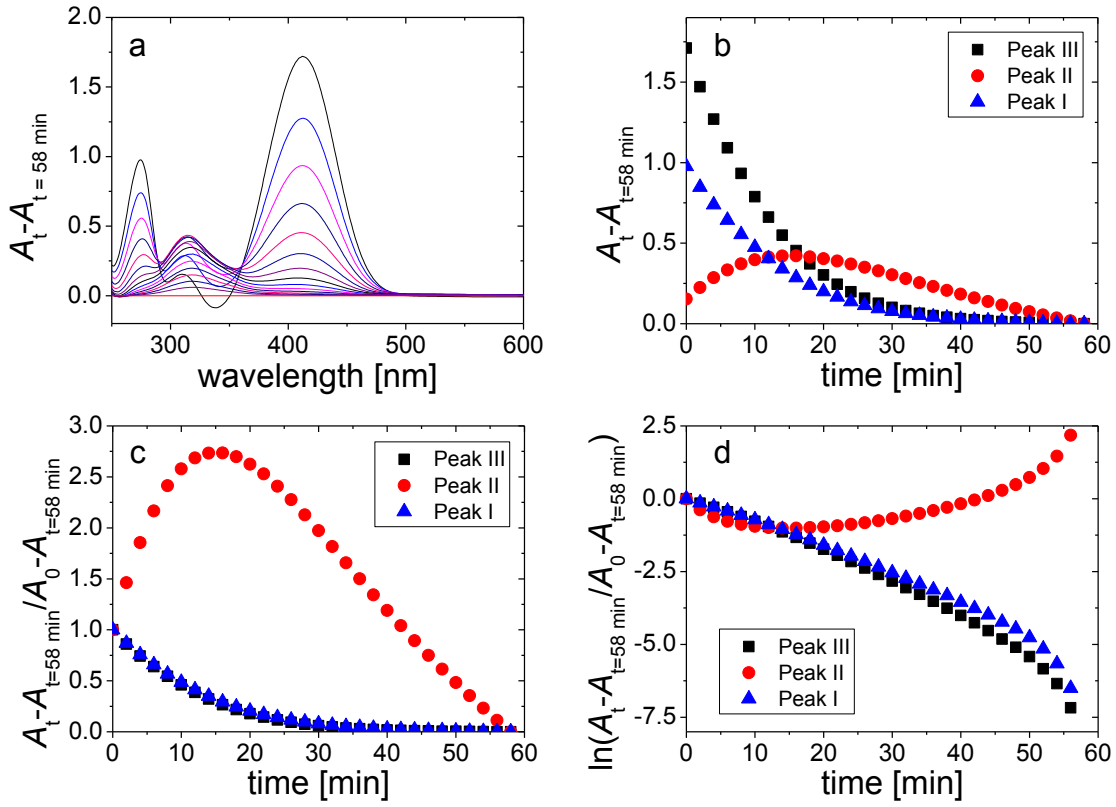

Figure 39: a) Spectra of the oxidation of morin normalized by the spectra at 58 minutes, where the main absorption peak at 410 nm is diminished. b) Peak development using the normalized spectra at 58 minutes. The analyzing of peak II (310 nm) is difficult, due to the fact, that the peak maximum shifts to higher wavelengths with propagating reaction time, c) normalized absorption of the peaks at t = 0 to a value of 1, d) logarithmic plot of the peak development with time. For a better comparison the peak at 310 nm is multiplied by -1.

3.5.2 The Role of Oxygen in the Oxidation of Morin

Further experiments are performed to discover the role of oxygen from air. As shown in Figure 40, the oxidation of morin without H_2O_2 in the presence of the catalyst is observable in the UV-vis measurements. Here, peak II increases slowly until it reaches a maximum. The isosbestic points remain visible throughout the whole time of measurement. When the stock solutions are purged with nitrogen the oxidation of morin is slower (see Figure 40a) compared to the unpurged solutions (Figure 40b).

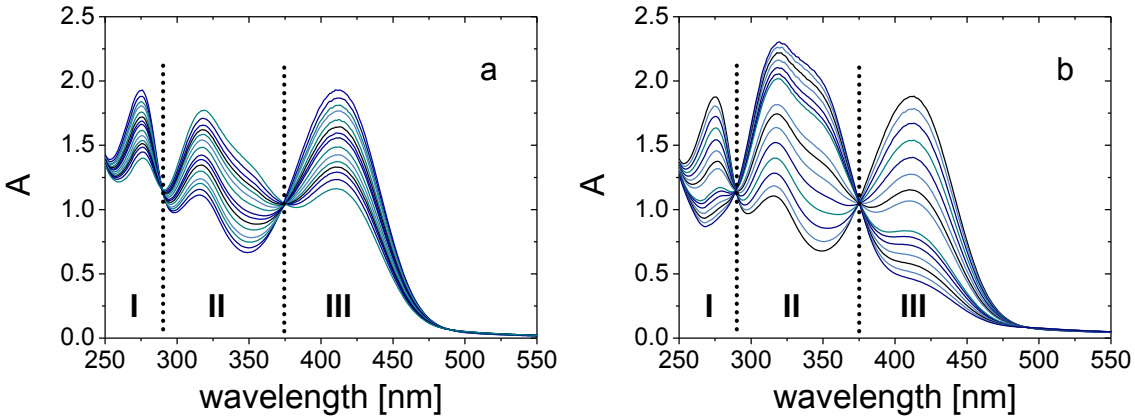

Figure 40: UV-vis-spectra of the oxidation of morin without H_2O_2, where all stock solutions were purged with nitrogen to remove dissolved oxygen (a), and when the stock solutions were not purged with nitrogen (b). The reaction conditions were: 10 mg L^{-1} MnO_x@SPB, 0.1 mM morin in 50 mM carbonate buffer solution, spectra taken every 2 minutes.

This indicates that oxygen dissolved in the water plays a major role in the catalyzed oxidation without H_2O_2. Interestingly, the reaction proceeds as well in solutions which were purged with nitrogen. Thus, in this starved conditions, the oxygen from the MnO_x NP may be of importance.

Espinal *et al*.[188] could demonstrate by ^{18}O labeling that for the epoxidation reaction of styrene with a high concentration of H_2O_2 and a low flow rate of O_2, the oxygen originates solely from the H_2O_2. Even at a low concentration of H_2O_2 and a high flow rate of O_2 most of the oxygen for the epoxidation arises from H_2O_2. At both reaction conditions the lattice oxygen of the catalyst was not found in the product. In reactions performed without H_2O_2 the oxygen is originates from O_2 and the lattice oxygen of the manganese oxide.[188] Therefore, the oxygen in solution and the lattice oxygen of the manganese oxide may be accountable for the oxidation of morin. The amount of oxygen in solution is reduced drastically by purging the solutions with nitrogen as can be observed in Figure 40. Thus, the reaction is much slower in this case.

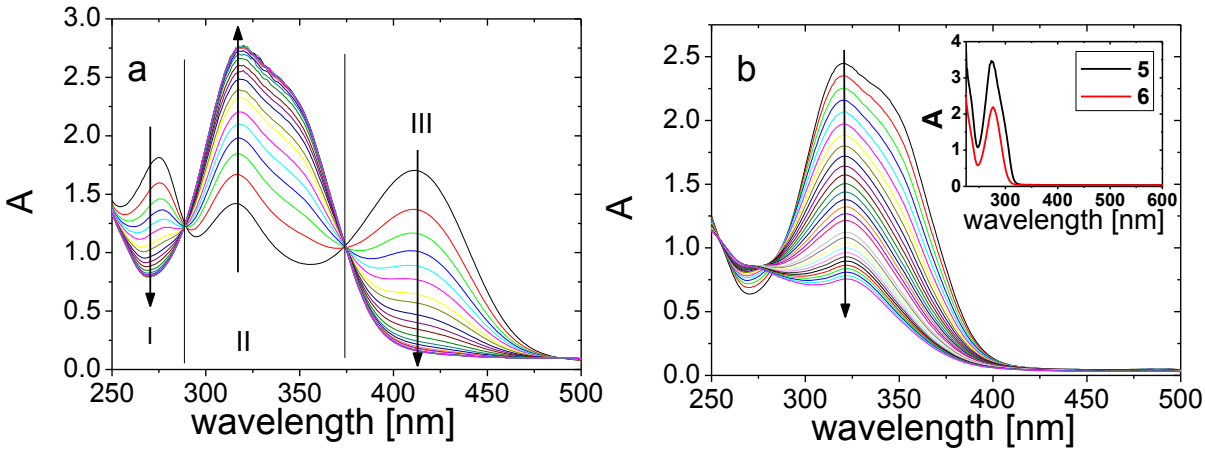

*Figure 41: a) UV-vis spectra of the reaction of morin without H_2O_2 in unpurged solutions. Spectra are taken every 8 minutes. The reaction conditions are: 10 mg L^{-1} MnO_x@SPB, 0.1 mM morin in 50 mM carbonate buffer solution. b) After the peak at 320 nm reaches a stable maximum, the solution is filtered to remove the catalyst. Thereafter, H_2O_2 is added and spectra are recorded every 4 minutes. The inset shows the adsorption spectra of the substances **5** (2,4,6-trihydroxy benzoic acid) and **6** (2,4-dihydroxy benzoic acid). The absorption maxima are in both cases at approximately 275 nm at 20 °C in 50 mM carbonate buffer solution.*

3.5.3 H_2O_2 as Oxidizing Agent

As shown in Figure 41a, the oxidation of morin without H_2O_2 in presence of the MnO_x@SPB proceeds until a maximum of peak II is reached. This is attributed to a reaction intermediate which is found to be stable for several hours. The UV-vis spectra of this intermediate is the same as the one Topalovic[189] measured in her study and is attributed to substance **7** (Figure 34). After filtration of the reaction mixture to exclude the catalyst, peak II decreases in presence of H_2O_2 (Figure 41b) and an additional shoulder at approximately 275 nm appears. Benzoic acids exhibit an absorption maximum around this wavelength as shown in the inset of Figure 41b which may be accountable for this shoulder.

This leads to the conclusion that the further decomposition to substances **5** and **6** (see Figure 33) proceeds only when H_2O_2 is present. Furthermore, these following reaction steps may be independent of the catalyzed reaction. As suggested in the work of Colombini *et al*.,[195] the first oxidizing step needs the manganese ion, whereas the following reaction steps can proceed in solution. Thus, Figure 41b may point in the same direction that the first oxidizing step occurs on the manganese oxide catalyst using surface bound oxygen

originated from O_2 or lattice oxygen under starved conditions or from the decomposition of H_2O_2. The following reaction steps may occur in the surrounding medium.

In Figure 42, the devolvement of peak II and III is shown for the reaction with H_2O_2. Both peaks are normalized by the absorption (A_0) at $t = 0$. Here, N_2 purged and unpurged solutions are shown for a better comparison. No visible difference between the purged and unpurged solutions occurred for the reactions with H_2O_2 as oxidizing agent (black squares in Figure 42 a and b). In contrary, the process of the reactions without H_2O_2 is very different if purged and unpurged solutions are used, as already indicated in Figure 40. In this context, non-nitrogen-purged reactions are faster than those treated with N_2. An additional measurement is performed as indicated by the purple dots in Figure 42. For this experiment, the solutions are purged with nitrogen and thereafter the cuvette is closed in order to avoid resolving of oxygen into the reaction solution. Surprisingly, no difference has been detected for the curves with and without this prevention.

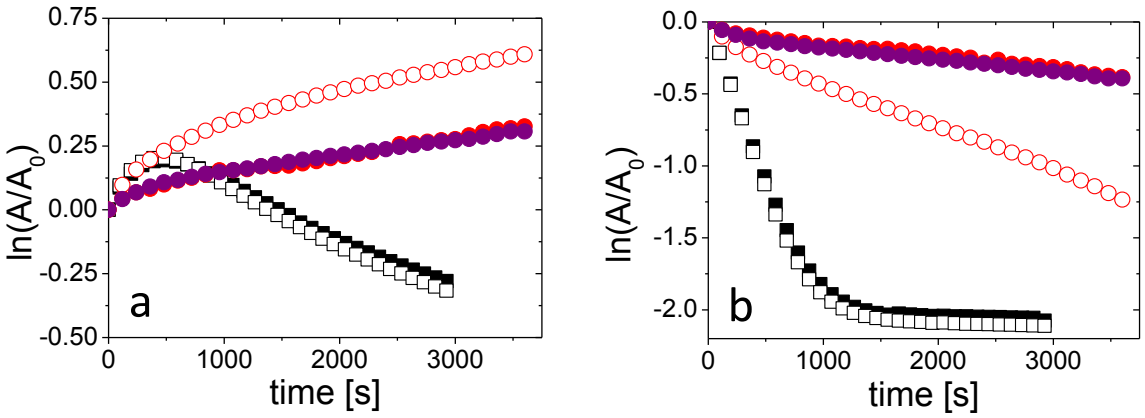

Figure 42: The filled symbols display measurements, for which the solutions are purged with nitrogen. Open symbols represent measurements without purging with nitrogen. The black squares symbolize measurements with H_2O_2 (10 mM H_2O_2), the dots and circles depict measurements without H_2O_2. The red dots show measurements of solutions, purged with nitrogen, whereas the purple dots represent measurements, for which the cuvette was additionally closed, to prevent dissolving of oxygen. Reaction conditions: 20 °C, 0.1 mM morin, 20 mg L^{-1} MnO_x@SPB. a) Dependence of the reaction conditions on the peak evaluation at 310 nm. b) Dependence of the reaction conditions on the peak evaluation at 410 nm.

All these experiments indicate that the oxidation by air is negligible in the reaction when H_2O_2 is used as oxidizing agent, because the oxidation by aerial oxygen is much slower. A similar behavior was found by Topalovic *et al.*[189], as well. Due to this, an excess of H_2O_2 is applied for the detailed analysis of the kinetics, in order to avoid such side effects.

3.5.4 Kinetic Study of the Catalytic Morin Oxidation

For further analysis of the rate constant, the decrease of the maxima of peak III at 410 nm is evaluated. The benefit of the evaluation of this peak is that no additional normalization is necessary. Due to the excess of the oxidizing agent, the reaction can be treated as a first order reaction without any loss of generality, which simplifies the analysis of the kinetics. If these prerequisites are fulfilled, the apparent rate constant k_{app} can be described as:

$$\frac{dc_{morin}}{dt} = - k_{app} \cdot c_{morin} \cdot c_{H_2O_2} = - k_{app} \cdot c_{morin} \qquad 3.29$$

where c_{morin} is the concentration of morin, $c_{H_2O_2}$ is the concentration of H_2O_2 and k_{app} is the apparent rate constant.

Additionally, the influence of the manganese content on the rate constant is investigated. In Figure 43, the evaluation of the catalytic oxidation with different weight percentages of manganese is shown. There, the applied morin concentration is 0.1 mM and H_2O_2 is 10 mM. The black squares in this figure correspond to the measurements directly after the synthesis of the manganese oxide platelets; the red diamonds represent measurements for the sample after a half year storage. This demonstrates that the particles are very stable in an aqueous environment. Furthermore, a linear dependence of the rate constant on the concentration of manganese in the system is found. For the detailed analysis of the catalytic activity always 10 wt. % of the MnO_x@SPB are used for the measurements which corresponds to a manganese content of 0.039 mg L^{-1}.

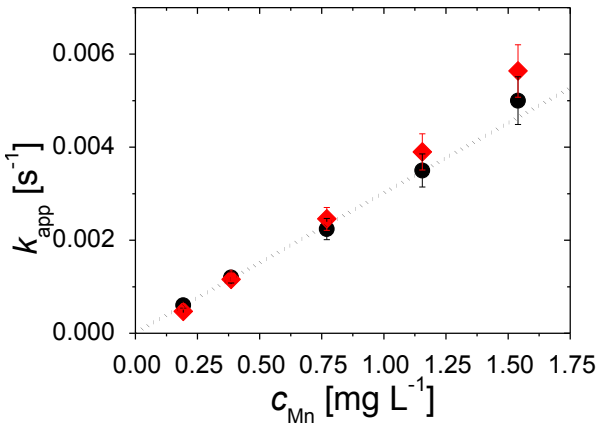

Figure 43: Dependence of the rate constant on the content of manganese oxide (c_{morin} = 0.1 mM, c_{H2O2} = 10 mM, carbonate buffer concentration = 12.5 mM, T = 20 °C). The black dots denote measurements directly after the synthesis of the MnO_x@SPB. The red diamonds represent the same measurements for MnO_x@SPB particles stored for nearly six month.

3.5.5 Influence of the Buffer System on the Oxidation

The pH-value is kept constant at pH = 10 in all reactions during this study by using a carbonate buffer. This is necessary because a) the absorbance of morin is pH dependent, b) the pH-value plays a role in the decomposition rate of H_2O_2,[196] c) MnO_x NP may dissolve under acidic conditions, which could cause side effects on the kinetics. The leaching of the catalyst at pH ≥ 9 is found to be around 1 ppm.[74] Therefore, an influence of free manganese ions can be excluded. Nevertheless, a fresh sample of the catalyst is used for each kinetic run in order to avoid any problems caused by decomposition of the MnO_x@SPB particles.

As a next step, the influence of the buffer system is studied. Ember *et al.*[192] proved that the concentration of carbonate ions have an influence on the oxidation rate with a manganese (II) complex. Here, they ascertain an equilibrium between H_2O_2, carbonate and peroxo-carbonate:

$$HCO_3^- + H_2O_2 \leftrightharpoons HCO_4^- + H_2O \qquad 3.30$$

They furthermore claimed that the reaction rate in the carbonate buffer is increased, because HCO_4^- is more reactive than H_2O_2. Moreover, they found a second order dependence on the buffer concentration for the catalytic activity in their study. Their explanation of the

second order dependency was that two carbonate ions are required for the oxidation reaction: one carbonate ion for the formation of the more reactive peroxocarbonate (HCO_4^-) and another carbonate ion for coordinating the manganese-pyridine-complex. Furthermore, they measured the dependence of the pH-value on the catalytic activity. Here, an optimum is reached at a pH-value of approximately 8.5.[192] By testing different concentrations of carbonate buffer at pH = 10, a nearly linear dependence of k_{app} on the total carbonate concentration is found as shown in Figure 44. The slope could be estimated with 0.004 L mol^{-1} s^{-1}. In contrast to Ember *et al.*[192], a second order dependence of k_{app} on the carbonate concentration is not found. The first order dependence found in Figure 44 may be due to the fact that solid MnO_x particles inside the brush do not form additional complexes with carbonate ions. Another reason for the smaller dependence is the higher pH-value in the present measurements. With higher pH-values, the concentration of hydrogen carbonate is decreasing and thus the enhancement by the peroxocarbonate is reduced. Without catalyst, no reaction takes place, which indicates that the peroxocarbonat alone is not able to oxidize morin. Moreover, the use of a boric acid buffer system leads to apparent rate constants in the same range as that in case of the carbonate buffer system (Figure 44). Therefore, a strong influence of the buffer on the rate constant in the MnO_x@SPB system can be ruled out. The residual dependence in the concentration of the buffer system may be explained by the finite influence of the ionic strength on the catalytic activity of manganese oxide nanoparticles.

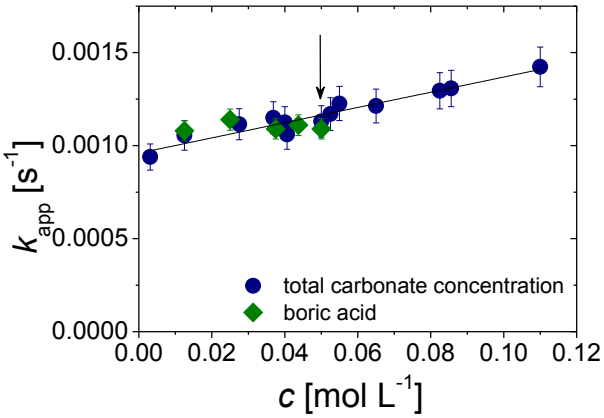

Figure 44: Dependence of the rate constant on the concentration of carbonate ions in solution (blue dots) and on the boric acid concentration (green diamonds). The arrow marks the carbonate concentration which is used in the Langmuir-Hinshelwood analysis. Reaction conditions: 10 mg L^{-1} MnO_x@SPB, 10 mM H_2O_2, 0.1 mM morin.

Two additional buffer-solutions are tested, namely a borax buffer and a CHES (2-(cyclohexylamino)ethanesulfonic acid) buffer solution. Figure 45a indicates that the oxidation in CHES buffer is much slower in comparison to the reaction in a carbonate buffer system. This may be due to the surfactant like structure of this buffer system. The reaction rate in the borax buffer is similar to that in the carbonate buffer (Figure 45b). However, there is a distinctive difference in the behavior of peak II, which shifts to smaller wavelengths, whereas in carbonate buffer peak II shifts to higher wavelengths. This indicates a different reaction pathway of the oxidation reaction in the borax buffer system. The increase in peak II is more pronounced in the borax buffer than in the carbonate buffer. The reason for this behavior may be that the reaction intermediate, which is produced in the first oxidation step, is more stable in this buffer.

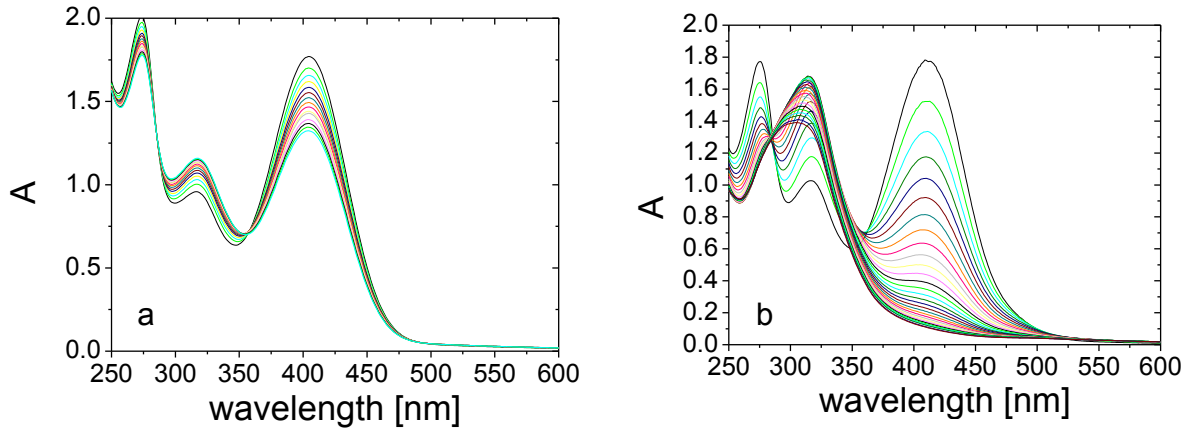

Figure 45: Catalytic oxidation of morin on MnO_x-nanoparticles with H_2O_2 a) in CHES buffer (pH 10) and b) in borax buffer (pH 10). Spectra are taken every 2 minutes. Reaction conditions: 10 mg L^{-1} MnO_x@SPB, 10 mM H_2O_2, 0.1 mM morin, T = 20 °C.

3.5.6 Langmuir-Hinshelwood Model

Analogous to the reduction of *p*-nitrophenol, two possible models are reasonable. First, the Langmuir-Hinshelwood model, where both educts must adsorb onto the surface of the nano-particles and second, the Eley-Rideal mechanism. Here, only one educt adsorbs onto the surface and reacts with the other educt in solution. By varying the concentration of one of the educts and keeping the other constant, it is easy to distinguish between these two mechanisms. The apparent reaction rate should be linearly increasing with an increasing concentration of

the educt which reacts from the solution in case of an Eley-Rideal mechanism.[98] In Figure 46 such a concentration variation of morin and H_2O_2 is shown.

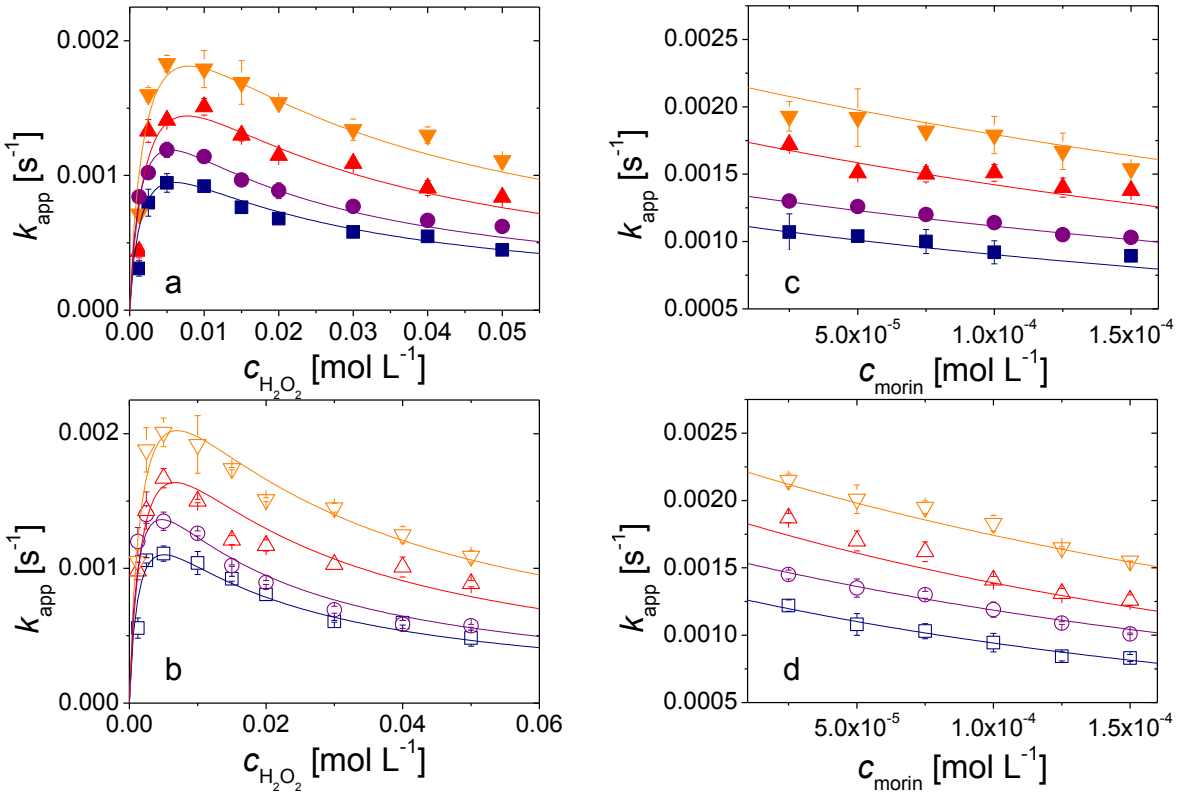

Figure 46: Left: influence of the concentration of H_2O_2 on the apparent rate constant k_{app} of the catalytic oxidation of morin with c_{morin} = 0.1 mM (filled symbols) and c_{morin} = 0.05 mM (open symbols) at c_{Mn} = 0.039 mg L^{-1} at different temperatures (blue squares = 15 °C, purple circles = 20 °C, red upright triangles = 25 °C, and orange inverted triangles = 30 °C). Right: influence of the concentration of morin on the apparent rate constant k_{app} of the catalytic oxidation of morin with c_{H2O2} = 10 mM (filled symbols) and c_{H2O2} = 5 mM (open symbols) at c_{Mn} = 0.039 mg L^{-1} at different temperatures (blue squares = 15 °C, purple circles = 20 °C, red upright triangles = 25 °C, and orange inverted triangles = 30 °C). The solid lines mark the fits by the Langmuir-Hinshelwood model.

On the left side of Figure 46 the concentration of morin is varied between 0.025 mM and 0.15 mM with two constant concentrations of H_2O_2, 10 mM (a) and 5 mM (b). On the right side, the concentration of H_2O_2 is varied between 2.5 mM and 50 mM with two constant concentrations of morin 0.1 mM (c) and 0.05 mM (d). As shown in Figure 46, there is no linear increase in the reaction rate with an increase in each concentration variation. Therefore, the Eley-Rideal mechanism can be excluded and the Langmuir-Hinshelwood ansatz is chosen for further analysis as indicated by the solid lines in the figure.

The scheme of a Langmuir-Hinshelwood kinetic is shown in Figure 47 for a better understanding: Both H_2O_2 and morin adsorb on the surface of the manganese oxide nanoparticles. The rate determining step is the surface reaction of the active oxide species and the adsorbed morin. Subsequently, the degradation product desorbs from the surface leaving an open active site for the reaction.

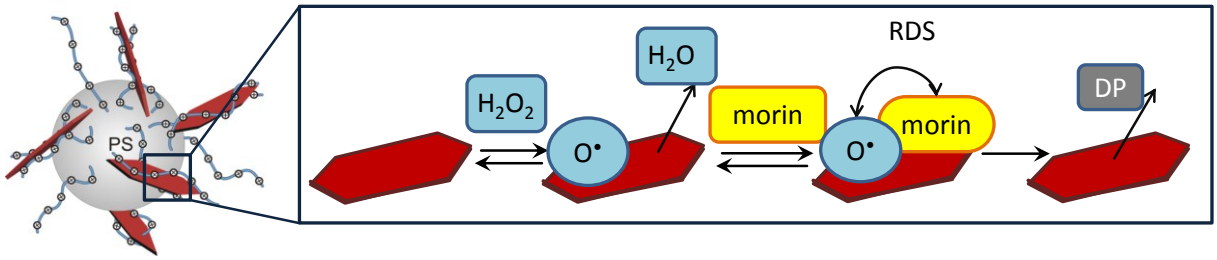

Figure 47: Mechanistic model of the oxidation of morin by H_2O_2 in the presence of manganese oxide nanoparticles (red hexagons) according to a Langmuir-Hinshelwood mechanism. These metal oxide nanoparticles are embedded in the brush layer of cationic SPB. The reaction of H_2O_2 with the surface leads to adsorbed active oxygen species and water is released. Parallel, morin adsorbs onto the nanoparticle surface. The reaction of morin with the active oxygen species on the surface is the rate determining step (RDS) of the overall catalytic cycle. Finally, the decomposition product of morin (DP) desorbs from the catalyst surface, leaving a free active site for a new catalytic reaction.

It was assumed for the modeling that the adsorption of all reactants is reversible and can be modeled by a Langmuir isotherm. The decomposition of H_2O_2 on MnO_2 particles is a complicated process with various steps as shown by Do *et al.*[74] (see chapter 3.4). First, H_2O_2 adsorbs on the manganese oxide nanoparticles. There, it can form various decomposition products as hydroperoxyl radicals, hydroperoxide/superoxide anions, or surface bound peroxides. The latter one can further react to produce oxygen or is involved in oxidation reactions and is therein reduced to water. The work of Zhou *et al.*[193] demonstrated that the kinetics of the decomposition of H_2O_2 on a manganese oxide surface can be described by:

$$- r_{H_2O_2} = k_{H_2O_2} \cdot \theta_{H_2O_2} \qquad 3.31$$

where $r_{H_2O_2}$ is the rate of the H_2O_2 decomposition on the surface, $k_{H_2O_2}$ is the overall reaction rate, which is independent of the concentration of H_2O_2, and $\theta_{H_2O_2}$ is the surface coverage of H_2O_2. This can be modeled by a Langmuir adsorption isotherm. The agreement of

the kinetic data in this study and the proposed reaction mechanism leads to the conclusion that a Langmuir adsorption is suitable to describe the adsorption on the manganese oxide. Considering the work of Do *et al*.[74] the use of a Langmuir adsorption isotherm may be a simplification.

In a Langmuir-Hinshelwood model the diffusion of the reactants to the catalyst surface and the adsorption/desorption processes are assumed to be fast. Due to the open structure of the brush the diffusion of the educts to the catalytic active nanoparticles should be very fast, similar to the diffusion of *p*-nitrophenol (chapter 2.2.4 and 3.2.2). The rate determining step is the surface reaction of morin with a surface-bound oxygen species. Moreover, it is assumed that no back reaction takes place. Desorption of the product leads to a free active site and the catalytic cycle can start again.

Within the frame of this approach, the Langmuir-Freundlich isotherm is used for modeling the adsorption of the reactants.[102] This ansatz takes into account that the surface is not homogenous. Therefore the adsorption energy is not equal for all active sites of the catalysts surface (for the detailed description see chapter 3.2.3). The reaction rate is therefore given by equation 3.32.

$$k_{app} = \frac{k \cdot S \cdot K_{morin}^{n} \cdot c_{morin}^{n-1} \cdot \left(K_{H_2O_2} \cdot c_{H_2O_2}\right)^{m}}{(1 + (K_{morin} \cdot c_{morin})^{n} + \left(K_{H_2O_2} \cdot c_{H_2O_2}\right)^{m})^{2}} \qquad 3.32$$

Here, k is the molar rate constant, S is the surface area of the catalyst, K_{morin} and $K_{H_2O_2}$ are the adsorption constants of the two reactants, and the parameters n and m are the Freundlich exponents for morin and H_2O_2, respectively.

Figure 43 demonstrates that k_{app} is proportional to the concentration of manganese oxide nanoparticles inside the SPB and thus the surface of the nanoparticles. As already mentioned, the MnO_x is formed in thin K^+-birnesite platelets inside the SPB. Due to the different orientations of the platelets inside the SPB, a surface determination of all MnO_x nanoparticles is not possible by means of TEM and cryo-TEM micrographs. Therefore, the exact value of the molar rate constant cannot be identified. For this reason, the product of the intrinsic rate constant and the surface area ($k \cdot S$) is applied as a fitting constant. Nevertheless, the Langmuir-Hinshelwood model describes the experimental data quite well (solid lines in Figure 46 a - d). By varying the concentration of morin at a constant concentration of H_2O_2 the reaction rate is slowly decreasing for all measured concentrations. In the case of the concentration variation

of H_2O_2 the reaction rate first increases, reaches then a maximum around c_{H2O2} = 0.01 mol L^{-1} and is slowly decreasing at a higher concentration of H_2O_2.

This behavior can be explained by the higher adsorption constant of morin compared to H_2O_2. Both educts compete for the active surface sites, and due to the higher adsorption affinity, morin is favored to be adsorbed. Therefore, the reaction rate decreases by a rising concentration of morin. In the case of H_2O_2, an increasing concentration leads to an increase in the rate constant until a maximum is reached, because more H_2O_2 can be adsorbed. The rate constant decreases again at higher concentrations of H_2O_2 because the surface gets saturated with the oxidizing agent.

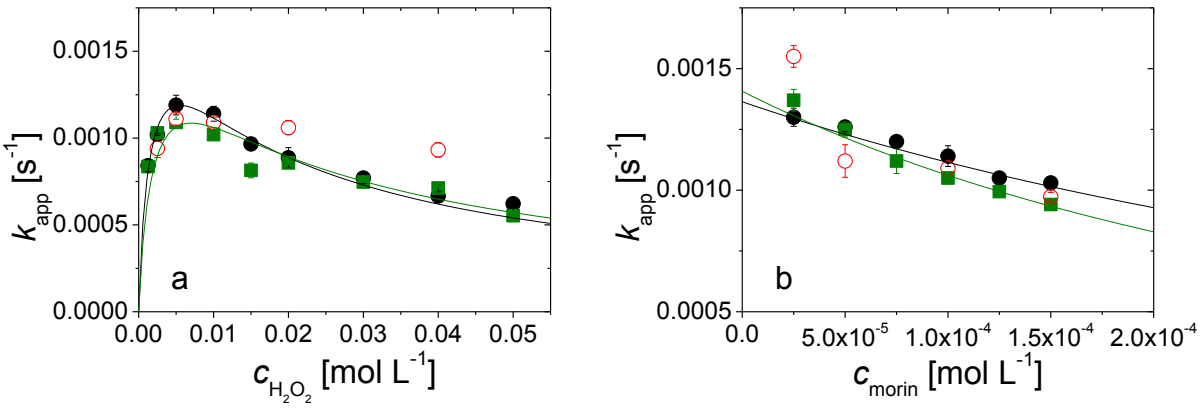

Figure 48: Langmuir-Hinshelwood analysis for different buffer systems: black points: 50 mM carbonate buffer; green squares: 12.5 mM carbonate buffer; red hollow circles: borax buffer at 20°C for the concentration variations of H_2O_2 (a) and the concentration variation of morin (b) at 10 mg L^{-1} MnO_x@SPB.

The same measurements are conducted for different buffer concentrations and a borax buffer system to determine the effect of the carbonate concentration. As shown in Figure 48 the deviations in the 12.5 mM and the 50 mM carbonate buffer solutions are very small and lie within the error of the measurements. Only the 50 mM borax buffer system shows a small discrepancy at higher concentrations of H_2O_2 and very low concentrations of morin. Therefore, for the carbonate system the influence of the buffer concentration can be neglected.

The values obtained by the application of the Langmuir-Hinshelwood model for the different temperatures are shown in Table 10. As expected, the intrinsic rate constant is increasing with an increasing temperature, while the adsorption constants of morin and H_2O_2 are decreasing with an increasing temperature. Therefore, the adsorption process is exothermic for both educts.

Table 10: Rate constant ($k \cdot S$) and the adsorption constants for the oxidation of morin with H_2O_2 on MnO_x@SPB obtained by best fit model according to eq. 3.32.

T [°C]	$k \cdot S$ [mol L^{-1} s^{-1}]	K_{morin} [mol L^{-1}]	$K_{H_2O_2}$ [mol L^{-1}]	n	m
15	$(1.36 \pm 0.26) \cdot 10^{-6}$	3866 ± 1157	242 ± 20	1 ± 0.04	0.87 ± 0.03
20	$(1.86 \pm 0.41) \cdot 10^{-6}$	3434 ± 1174	255 ± 24	1 ± 0.04	0.86 ± 0.02
25	$(2.48 \pm 0.82) \cdot 10^{-6}$	3145 ± 1623	175 ± 18	1 ± 0.07	0.90 ± 0.04
30	$(3.48 \pm 1.34) \cdot 10^{-6}$	2631 ± 1529	165 ± 17	1 ± 0.07	0.86 ± 0.04

From Table 10, the fitting values are restrained at n = 1 and m = 0.87 because the deviations of the exponents in the measured temperature range are very small. The remaining variables are refined by fixed n and m. The refined values are given in Table 11.

Table 11: Rate constant and ($k \cdot S$) the adsorption constants for the oxidation of morin with H_2O_2 on MnO_x@SPB obtained by best fit model according to eq. 3.32 by setting the exponents n = 1 and m = 0.87.

T [°C]	$k \cdot S$ [mol L^{-1} s^{-1}]	K_{morin} [mol L^{-1}]	$K_{H_2O_2}$ [mol L^{-1}]
15	$(1.33 \pm 0.09) \cdot 10^{-6}$	4052 ± 387	244 ± 10
20	$(1.89 \pm 0.15) \cdot 10^{-6}$	3368 ± 351	249 ± 11
25	$(2.46 \pm 0.33) \cdot 10^{-6}$	3146 ± 523	179 ± 11
30	$(3.47 \pm 0.50) \cdot 10^{-6}$	2642 ± 458	164 ± 9

3.5.7 Analysis of the Thermodynamic Parameters

From the values given in Table 11, the temperature dependence of the adsorption constants and the rate constants can be evaluated. The apparent activation energy for k_{app} is E_A = 35.6 ± 0.2 kJ mol^{-1} for a 12.5 mM carbonate buffer solution and E_A = 32.7 ± 0.8 kJ mol^{-1} for the 50 mM carbonate buffer solution as derived from Figure 49c. The activation energy for the intrinsic rate constant ($k \cdot S$) is E_A = 45.8 ± 7.0 kJ mol^{-1}, which is higher than that of the apparent rate constants (Figure 49a). This discrepancy can be explained by the use of the apparent rate constant for the calculation of the activation energy according to the discussion in chapter 3.2.6. It is dependent on the true activation energy, which can be obtained from the temperature dependence of the intrinsic rate constant ($k \cdot S$) and from the temperature dependence of the adsorption constants of both educts as indicated in eq. 3.33.

$$k_{app} = k \cdot S \cdot \theta_{morin} \cdot \theta_{H_2O_2} \qquad 3.33$$

The temperature dependence of the adsorption constants can be calculated by using the Van't Hoff equation. In Figure 49b this temperature dependence is shown. Table 12 summarizes the results. Both adsorption enthalpies are negative. Therefore, the exothermic adsorption process lowers the apparent activation energy considerably

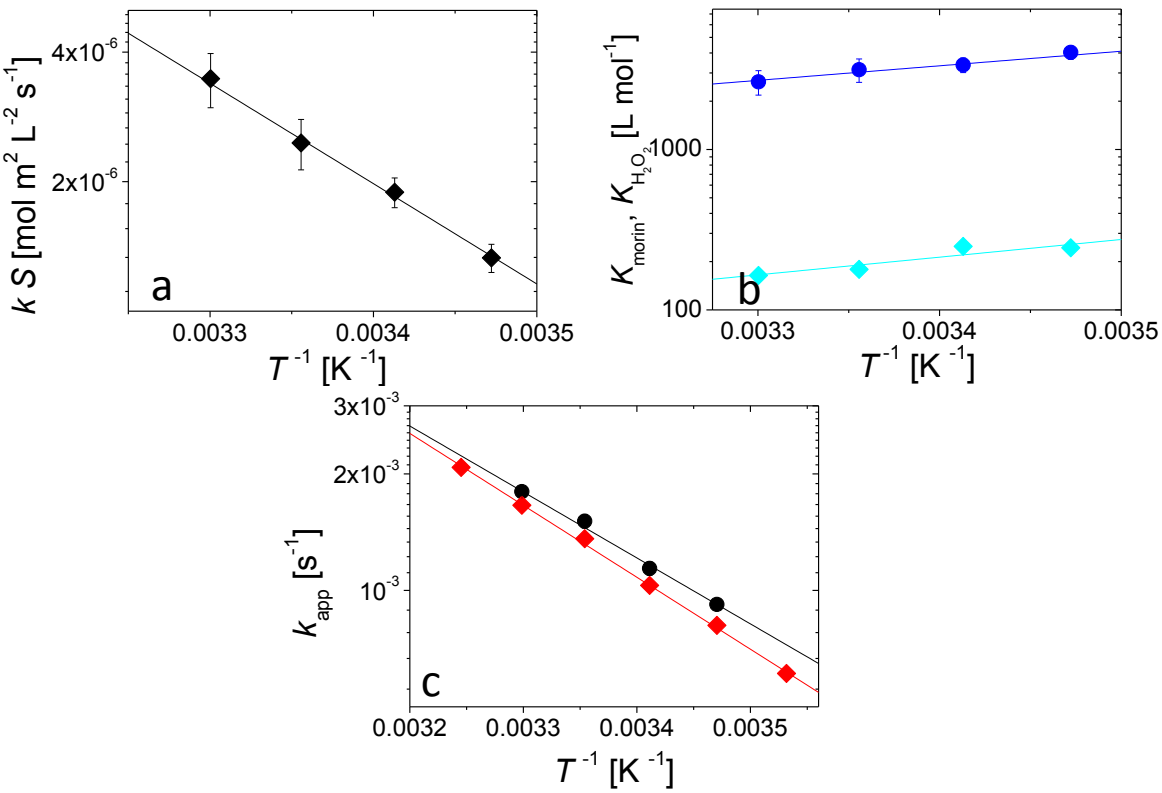

Figure 49: Temperature dependence of the intrinsic rate constant (a), the adsorption constants K_{morin} (blue dots) and K_{H2O2} (cyan diamonds) (b) and the apparent rate constants for two buffer concentrations (red diamonds: 12.5 mM; black dots: 50 mM) (c). a and b are measured with the 50 mM carbonate buffer solution.

Table 12: Temperature dependence of the adsorption constants of morin and H_2O_2 derived from the Langmuir-Hinshelwood model.

	ΔH [kJ mol^{-1}]	ΔS [J mol^{-1} K^{-1}]
K_{morin} [L mol^{-1}]	-19.8 ± 8.7	0.2 ± 29.6
K_{H2O2} [L mol^{-1}]	-20.8 ± 3.1	-26.1 ± 10.7

The adsorption entropy is negligible in case of morin, but the adsorption entropy is negative in the case of the H_2O_2. Apart from that, the interpretation of the thermodynamic parameters is difficult, because the adsorption of H_2O_2 on the surface of MnO_2 particles is a complex multi-step process.[74] However, the negative adsorption entropy indicates an increased order in the system by the adsorption of H_2O_2. The H_2O_2 decomposes on the surface eventually to water and surface oxygen. Thus, the adsorption of H_2O_2 may lead to a more ordered top layer of oxygen on the catalyst surface and sets free water as one decomposition product. Both possibilities lower the overall entropy of the system.

In summary, this reaction follows a Langmuir-Hinshelwood type of kinetic. Both educts adsorb onto the manganese oxide nanoparticles to react. Measurements at different temperatures allow the calculation of thermodynamic parameters as activation energy, adsorption enthalpy and entropy for morin and H_2O_2, respectively.

4. Summary

This work is divided in two main parts: first, the kinetic study of the reduction of *p*-nitrophenol and in the second part the oxidation of morin. Both reactions could be analyzed by UV-vis measurements due to the strong absorption bands of both molecules in the visible range.

Gold and platinum nanoparticles are synthesized in spherical polyelectrolyte brushes (SPB) and applied as catalysts in the mechanistic studies of the reduction of *p*-nitrophenol by sodium borohydride. The reaction follows the Langmuir-Hinshelwood mechanism. Therefore, both educts adsorb onto the surface of the catalyst. The surface reaction of both educts is the rate determining step. After the reaction, the product, *p*-aminophenol, desorbs from the surface and a free active site is formed. Applying the Langmuir-Hinshelwood model, the analysis of the apparent rate constant reveals the intrinsic rate constant and the adsorption constants for both educts. Furthermore, the temperature dependence of these constants is analyzed by performing measurements at different temperatures with gold nanoparticles of the size of 2.2 nm. This allows the calculation of the activation energy of the reaction (E_A = 50 kJ mol^{-1}) and the adsorption enthalpy and entropy of the educts. The adsorption enthalpy was ΔH = 13 kJ mol^{-1}, in case of *p*-nitrophenol and ΔH = 3 kJ mol^{-1} in case of borohydride. The adsorption enthalpy of *p*-nitrophenol is endothermic, thus energy is required to adsorb onto the surface. This is balanced by the high value of the adsorption entropy (ΔS = 116 J mol^{-1} K^{-1}). Therefore, the adsorption of *p*-nitrophenol is entropy driven. In comparison the adsorption of borohydride is independent of the temperature.

The induction time of the reaction is another interesting phenomenon which is analyzed in this study. The reason of this delay time is possibly due to the restructuring of the nanoparticle surface. The induction time is independent of the concentration of borohydride. But the concentration of *p*-nitrophenol has a strong dependence on the induction time, which points to a restructuring process due to the adsorption of *p*-nitrophenol. Remarkably, hints for a re-construction of the nanoparticles without *p*-nitrophenol were also found in this analysis.

The second part of this thesis is the catalytic oxidation of morin (3,5,7,2',4'-pentahydroxy flavone) with hydrogen peroxide by manganese oxide nanoparticles embedded inside the polyelectrolyte layer of the spherical polyelectrolyte brushes. Previous studies have shown that these platelets are of K^+-birnessite type. A Langmuir-Hinshelwood type kinetic can be

applied in this study as well. The intrinsic rate constant and the adsorption constants can be achieved at different temperatures. This allowes the calculation of the true activation energy of this reaction with E_A = 46 kJ mol^{-1} and the adsorption enthalpy and entropy for the educts. The adsorption enthalpy in both cases is exothermic, ΔH = -19.8 kJ mol^{-1} and ΔH = -20.8 kJ mol^{-1} for morin and hydrogen peroxide, respectively. The adsorption entropy in case of morin is negligible, whereas the adsorption entropy in case of H_2O_2 is ΔS = -26.1 J mol^{-1} K^{-1}, pointing to a more ordered structure after the adsorption of H_2O_2.

5. Experimental Part

5.1 Equipment

5.1.1 TEM

The polymeric solutions were diluted to 0.1 to 0.2 wt.% and dropped on copper grids. The transmission electron microscopy measurements were taken at a Zeiss 922 Omega electron microscope, cryo-TEM (TEM, Zeiss NTS GmbH, Oberkochen, Germany), and high resolution TEM studies of single particles were performed, applying an objective-lens corrected FEI Titan 80 - 300 operated at 300 keV. The aberration corrector was set to small negative values $c_s < 200$ nm.

5.1.2 DLS

The radii of the SPB particles were measured by dynamic light scattering (DLS). The DLS apparatus (ALV) consists of a 50 mW He-Ne-Laser ($\lambda = 632.8$ nm), a thermostat, a tempered measure cell, a goniometer, and a detector with signal reduction system. The data were analyzed with the ALV-Correlator Software V.3.0. For the measurements, the polymeric solutions were diluted to 1mg L^{-1}, filtered by a 1.2 µm filter (Pall, Supor Acrodisc, VWR), filled in a quartz glass cuvette (Hellma) and tempered in the measurement cell at 25 °C for approximately 20 minutes. The samples were prepared in a clean room bench from Herdinger to avoid dust contamination.

If the samples have a small polydispersity, the measurements at 25 °C can be performed only at a scattering angle of 90 °. From the calculated diffusion coefficient the radius of the particles can be achieved by the Stokes Einstein equation:

$$D = \frac{3 \cdot k_B \cdot T}{2 \cdot \pi \cdot \eta \cdot R_H} \qquad 5.1$$

where D is the diffusion coefficient, k_B is the Boltzmann constant, T is the temperature, η is the dynamic viscosity and R_h is the hydrodynamic radius.

5.1.3 NMR

NMR spectra were taken by a Bruker Avance 300-Spektrometer at 25 °C. The solvent was $CDCl_3$ (δ = 7.24, 77.0). The chemical shifts (δ) are determined relative to the signal of the solvent and are given in [ppm].

5.1.4 Ultrafiltration

The polymeric samples were cleaned by ultra filtration. A scheme of a ultra-filtraion cell is shown in Scheme 9. The polymeric solution is filled in the ultra-filtration cell. Clean water is pushed inside from a reservoire by overpressure. The solution is filtrated by a nitrocellulose membran with a pore size of 50 or 100 nm and the filtrate is expelled. The polymeric solution is stirred by a magnetic stirrer inside the cell to avoid sedimentation.

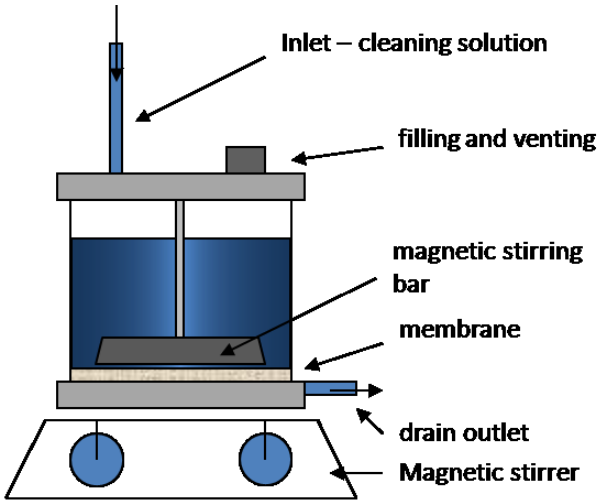

Scheme 9: Scheme of an ultra-filtration cell.

5.1.5 TGA

A Mettler Toledo STARe was used for the platinum nanoparticles. Approximately 8 mg of the solid composite particles were heated to 800 °C under a 60 mL min^{-1} nitrogen flow with a heating rate of 10 K min^{-1} and holding temperature at 800 °C for about 30 minutes.

The TGA samples in case of the gold NP with a size of 2.2 nm were measured at a Netsch STA 409PC LUXX®. For the TGA measurements approximately 20 mg of the dried samples were filled in the crucible which was then inserted in the TGA. With a heating rate of 10 K min^{-1} and an argon flow rate of 30 ml min^{-1} the samples were heated to 800 °C and then hold at this temperature for approximately one hour. The weight loss was attributed to the polymer and the remaining weight to the metal content of the sample. Pure polymer samples (PS-PTMAEMAC) were tested and showed a weight loss of 99.98 %.

5.1.6 UV-vis spectroscopy

The UV-vis spectra were taken with a PerkinElmer Lambda 650. Thereby, the visible spectra between 315 – 900 nm is generated by a tungsten-halogen-lamp, whereas the UV-range originates from a deuterium lamp. The sample environment is thermo-regulated by a thermostat (Julabo F30-C). For each series of measurements the absorption of distilled water is measured and subtracted from each measurement. For the measurement the solutions were mixed and placed in a Spectrosil® quartz glass cuvette (190 - 2700 nm, Roth). Immediately the extinction was recorded by the program: PerkinElmer WinLab, with respect to the measurement time. The concentration of the educt arises from the extinction by the Lambert-Beer-law.

$$E(\lambda) = \lg \frac{I_0}{I} = \varepsilon(\lambda) \cdot c \cdot d \qquad 5.2$$

With $E(\lambda)$ is the extinction, I_0 is the Intensity of the incoming light, I is the intensity of the outgoing light, $\varepsilon(\lambda)$ is the extinctions coefficient, c is the concentration of the educt and d is the thickness of the cuvette.

5.2 Chemicals

Table 13: Chemicals used in this thesis and the supplier

H_2AuCl_4	Aldrich
H_2PtCl_6	Aldrich
K_2PtCl_4	Aldrich
Na_2PdCl_4	Aldrich
$NaHCO_3$	Sigma
H_2CO_3	Sigma
Borax buffer solution	Roth
$NaBH_4$	Merk
styrene	Sigma
AEMH	Sigma
TMAEMAC	Aldrich
DMEMA	Aldrich
pyridine	Sigma
methacryloyl chloride	Sigma
Irgaure	BASF
p-nitrophenol	Aldrich
morin	Fluka
H_2O_2	Aldrich
$KMnO_4$	Aldrich
CTAB	Sigma
V50	Fluka
Pyridine	Aldrich

5.3 Synthesis

5.3.1 Photo initiator (HMEM)

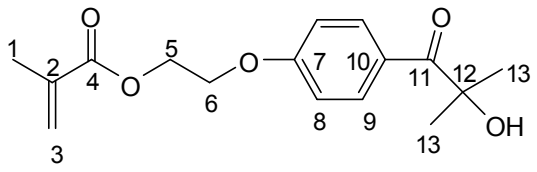

M: 292.16 g mol^{-1}

First step is the synthesis of the photo initiator 2-[*p*-(2-hydroxy-2-methylpropiophenon)]-ethylenglycolmethacrylat (HMEM). 94.8 g (0.426 mol) Irgacure is dissolved in 600 mL acetone at approximately 30 °C. Afterwards the base pyridine (50 mL) is added and the reaction mixture is cooled in an ice bath. After this 43.1 g (0.412 mol) methacryloyl chloride is added dropwise under constant stirring. The mixture is kept at room temperature overnight. Then the solvent is evaporated and the yellowish solution is cleaned first by extraction with water and then by a column of silica gel. The eluent is acetone : cyclohexane (1:2). The resulting HMEM was then characterized by NMR. The HMEM is stored as a solution in acetone of approximately 50 wt%.

Yield: 42.41 g (35.24 %) HMEM

^{1}H-NMR ($CDCl_3$) δ (ppm): 1.46 (s, 6H, H13); 1.80 (s, 3H, H1); 4.24 (br., 1H, OH); 4.18, 4.44 (m, 4H, H5, H6); 5.45, 5.99 (d, 2H, H13a, H13b); 6.82, 7.99 (m, 4H, H8, H9).

^{13}C-NMR ($CDCl_3$) δ (ppm): 18.1 (C1); 28.4 (C13); 63.1 (C6); 65.8 (C5); 77.3 (C12); 114.0 (C8); 126.1 (C3); 126.7 (C10); 132.4 (C9); 135.7 (C2); 162.0 (C7); 167.0 (C4); 202.4 (C11).

5.3.2 Polystyrene Core Synthesis

1.2 L water with 7.98 g hexadecyltrimethylammonium bromide (CTAB) is heated to 30 °C to dissolve the CTAB, then the mixture is cooled to room temperature again and 312 g of styrene is added under constant stirring. Afterwards the mixture is degassed, heated to 60 °C and 0.91 g initiator V50 (α,α′-azodiisobutyramidine dihydrochloride) in 30 ml H_2O is added. After 2 h of polymerization, 17.25 g photo initiator HMEM, dissolved in 17 g acetone, is added drop wise over a period of 3 h. The reaction is allowed to continue for another 3 h and then cooled to room temperature. The latex is cleaned by ultra-filtration until a conductivity of

20-30 μS cm^{-1} is reached. The radius of the poly(styrene)-co-HMEM particles is 40.7 nm and the concentration is 13.8 wt.% in water.

5.3.3 Synthesis of the Polyelectrolyte Brushes grafting on the Polystyrene Core

A 2.5 wt.% solution of the SPB-HMEM core is inserted inside the photo reactor and the 30 mol% solution (in reference to the styrene in the core particles) of the respective polyelectrolyte monomer is added slowly. Then the reaction media is stirred and repeatedly degassed. Afterwards the latex is irradiated by a CdI_2 doped mercury high pressure lamp TQ 150 Z_3 from Haraeus Noblelight (wavelengths 200 - 600 nm), which is cooled continually. The irradiation time is one hour, while the progress of the polymerization of the brush layer is verified by DLS measurements. The solution is stirred for one additional hour and then cleaned by ultra-filtration until the conductivity of the serum reached approximately 3 μS cm^{-1}. For the different monomers following brush lengths (*L*) and weight percent (wt. %) are obtained:

TMAEMAC	(*L*: 96 nm; wt. %: 2.8, TGA: -99.4%)
DEAMA	(salt free, *T*: 20°C: *L*: 80 nm; wt. %:3.9)
AEMH	(*L*: 60 nm, wt. %: 0.71)
TMAPMAA	(*L*: 73 nm; wt. %: 1.6).

5.3.4 Metallic Nanoparticles

For the metallic nanoparticles a 0.1 wt. % solution of the respective SPB is filled in a round bottom flask and stirred vigorously. To this solution 0.01 g of the metal salt in approximately 15 ml water is added drop wise in a time period of 20 minutes. This solution is stirred for 2 hours. Afterwards the solution is purged with nitrogen for a time period of 30 min while cooling by an ice bath. After this, 5 mol% sodium borohydride, with respect to the metal salt, in 20 ml H_2O is added drop wise over half an hour. The gray (Pt, Pd) or purple (Au) solution is stirred for one additional hour and then cleaned by ultra-filtration until the conductivity of the serum reaches 2 μS cm^{-1}. In case of the gold nanoparticles the AEMH

brush system is used, in case of platinum and manganese oxide the TMAEMAC brush system is used.

The size of the nanoparticles is obtained by measuring the diameter of approximately 400 nanoparticles in TEM micrographs, the metal content is analyzed by TGA measurements. The specific surface area of the nanoparticles can thus be calculated from the average radius and the total mass per particle. The density of the platinum and gold nanoparticle was taken from literature (Pt: 21.45 g cm^{-3} , [197] Au: 19.32 g cm^{-3}[197]).

Following NP were obtained and used in the kinetic measurements:

Pt NP: $r = 2.3 \pm 0.4$ nm, $S = 0.00687$ m^2 L^{-1} and $S = 0.00481$ m^2 L^{-1}

Au NP $r = 2.2 \pm 0.4$ nm, $S = 0.0108$ m^2 L^{-1}

5.3.5 Manganese Oxide Nanoparticles

In case of the manganese oxide nanoparticles, a 1.0 wt. % solution of the TMAEMAC-SPB system is purged with nitrogen under constant stirring for approximately 30 min, then 20 ml of a 0.04 mol L^{-1} solution of $KMnO_4$ is added drop wise. The solution is stirred overnight and then cleaned by ultra-filtration until the serum reached a conductivity lower than 3 µS cm^{-1}. Cryo-TEM micrographs, EDX and XRD measurements of a similar batch confirmed that the manganese oxide nanoparticles have a length of approximately 20 nm and a thickness of about 1.6 nm and are of a K^+-birnesste type.

5.3.6 Catalytic reactions

5.3.6.1 Reduction of *p*-Nitrophenol

In a typical UV-vis measurement 3 mL of the reaction solution is placed into the UV-vis spectrometer. In a "standard" nitrophenol reduction experiment 0.1 mol L^{-1} *p*-nitrophenol (Nip), 10 mol L^{-1} sodium borohydride (BH_4) (from a freshly prepared solution), and a certain amount of the catalyst solution is measured at a wavelength of 400 nm for 25 minutes. The stock solutions are purged with nitrogen before the reaction mixture is prepared. For the surface dependency standard concentrations (0.1 mM Nip, 10 mM BH_4^-) are used with different amounts of gold nanoparticles (2.2 nm) at 20 °C namely 20, 30, 40, 50, 70 and 90 µL of the catalyst stock solution, which are resulting in the following surface per volume 0.0086, 0.0130, 0.0173, 0.0216, 0.0302, and 0.0389 $m^2 L^{-1}$.

For the Langmuir-Hinshelwood study the following concentrations are used: The concentration of *p*-nitrophenol varies between 0.02 and 0.2 mol L^{-1} at two concentrations of borohydride (0.01 and 0.005 mol L^{-1}). The concentration of the catalyst is kept constant. For the concentrations of 0.01 mmol L^{-1} and 5 mmol L^{-1} borohydride the following mixtures are prepared:

Table 14: Concentration variation of p-nitrophenol at 10 mmol L^{-1} borohydride with a constant concentration of catalyst (platinum and gold nanoparticles).

volume [mL]	Nip [mmol L^{-1}]	Nip [ml]	BH_4 [mL]	H_2O [mL]
5.00	0.02	0.1	0.50	4.40
5.00	0.03	0.15	0.50	4.35
5.00	0.04	0.2	0.50	4.30
5.00	0.05	0.25	0.50	4.25
5.00	0.07	0.35	0.50	4.15
5.00	0.1	0.5	0.50	4.00
5.00	0.15	0.75	0.50	3.75
5.00	0.2	1	0.50	3.50

Table 15: Concentration variation of p-nitrophenol at 5 mmol L^{-1} borohydride with a constant concentration of catalyst (platinum and gold nanoparticles).

volume [mL]	Nip [mmol L^{-1}]	Nip [ml]	BH_4 [mL]	H_2O [mL]
5.00	0.02	0.1	0.25	4.65
5.00	0.03	0.15	0.25	4.60
5.00	0.04	0.2	0.25	4.55
5.00	0.05	0.25	0.25	4.50
5.00	0.07	0.35	0.25	4.40
5.00	0.1	0.5	0.25	4.25
5.00	0.15	0.75	0.25	4.00
5.00	0.2	1	0.25	3.75

For the concentration variation of borohydride the following concentrations of *p*-nitrophenol (0.1 mmol L^{-1} , 0.05 mmol L^{-1} and 0.025 mmol L^{-1}) are used as seen below. The concentration of 0.025 mmol L^{-1} was measured only with the platinum nanoparticles at 20 °C. The concentration of the catalysts is kept constant in all measurements.

Table 16: Concentration variation of borohydride at 0.1 mmol L^{-1} p-nitrophenol with a constant concentration of catalyst (platinum and gold nanoparticles).

volume [mL]	BH_4 [mmol L^{-1}]	BH_4 [mL]	Nip [mL]	H_2O [mL]
5.00	2	0.1	0.50	4.40
5.00	3	0.15	0.50	4.35
5.00	5	0.25	0.50	4.25
5.00	6	0.3	0.50	4.20
5.00	10	0.5	0.50	4.00
5.00	15	0.75	0.50	3.75
5.00	20	1	0.50	3.50

Table 17: Concentration variation of borohydride at 0.05 mmol L^{-1} p-nitrophenol with a constant concentration of catalyst (platinum and gold nanoparticles).

volume [mL]	BH_4 [mmol L^{-1}]	BH_4 [mL]	Nip [mL]	H_2O [mL]
5.00	2	0.1	0.25	4.65
5.00	3	0.15	0.25	4.60
5.00	5	0.25	0.25	4.50
5.00	6	0.3	0.25	4.45
5.00	10	0.5	0.25	4.25
5.00	15	0.75	0.25	4.00
5.00	20	1	0.25	3.75

Table 18: Concentration variation of borohydride at 0.025 mmol L^{-1} p-nitrophenol with a constant concentration of catalyst (platinum nanoparticles).

volume [mL]	BH_4 [mmol L^{-1}]	BH_4 [mL]	Nip [mL]	H_2O [mL]
5.00	2	0.1	0.125	4.775
5.00	3	0.15	0.125	4.725
5.00	5	0.25	0.125	4.625
5.00	6	0.3	0.125	4.575
5.00	10	0.5	0.125	4.375

From the respective 5 ml solution 3 ml are filled into the measurement cell and measured at a wavelength of 400 nm. For each concentration three to five measurements are performed. In case of the platinum nanoparticles the temperature is kept at 20 °C and two concentrations were measured. The calculated surfaces in these cases were S = 0.00687 m^2 L^{-1} and S = 0.00481 m^2 L^{-1}. In case of gold nanoparticles with the size of 2.2 nm, four different temperatures are measured: 10, 20, 25 and 30 °C with a surface area of S = 0.0108 m^2 L^{-1}. The measured data of the gold nanoparticles with the size of 1.5 nm at 20 °C is thankfully provided by F. Polzer. The absorbance (A) at 400 nm is normalized by A_0 at t = 0 s. From this plot the induction time is taken from the onset of the plateau phase. The apparent rate constant is calculated from the linear part of the slope.

5.3.6.2 Oxidation of Morin

A stock solution of 0.4 mM morin is used in these experiments, which is prepared fresh every day to avoid autoxidation of morin. Standard experiment conditions are 0.1 mM morin (1 mL from the stock solution), 10 mM H_2O_2 (40 µL from 0.1 mol L^{-1} solution), and 0.1 wt.% of the catalyst. For a constant pH-value a carbonate buffer solution is used. For the stock solution of morin the used buffer is employed. The volume of the overall mixture is 4 mL from which approximately 3 mL are put into the cuvette. For each data point approximately three to seven measurements are recorded. For the calculation of the activation energy, the apparent rate constant is determined for different temperatures. Hereby, the raw data of the measurements at 10, 15, 20, 25, 30, and 35 °C at a 0.0125 mol L^{-1} carbonate buffer at standard conditions is provided by F. Polzer. For the measurements concerning the manganese content the following concentrations of MnO_x@SPB are used: 5, 10, 20, 30, 40 mg L^{-1} at standard concentrations of morin and H_2O_2. In case of the concentration variation of morin, two

concentrations of H_2O_2 are used at a constant concentration of catalyst as shown in the following tables:

Table 19: Concentration variation of morin at 10 mmol L^{-1} H_2O_2 with a constant concentration of catalyst.

volume [mL]	morin [mmol L^{-1}]	morin [mL]	H_2O_2 [µl]	H_2O [mL]
4.00	0.15	1.5	40	2.42
4.00	0.125	1.25	40	2.77
4.00	0.1	1	40	2.92
4.00	0.75	0.75	40	3.17
4.00	0.5	0.5	40	3.42
4.00	0.25	0.25	40	3.67
4.00	0.1	0.1	40	3.82
4.00	0.05	0.05	40	3.87

Table 20: Concentration variation of morin at 5 mmol L^{-1} H_2O_2 with a constant concentration of catalyst.

volume [mL]	morin [mmol L^{-1}]	morin [mL]	H_2O_2 [µl]	H_2O [mL]
4.00	0.15	1.5	20	2.44
4.00	0.125	1.25	20	2.79
4.00	0.1	1	20	2.94
4.00	0.75	0.75	20	3.19
4.00	0.5	0.5	20	3.44
4.00	0.25	0.25	20	3.69
4.00	0.1	0.1	20	3.84
4.00	0.05	0.05	20	3.89

For the concentration variation of H_2O_2 at constant concentrations of morin following mixtures are used:

Table 21: Concentration variation of H_2O_2 at 0.1 mmol L^{-1} morin with a constant concentration of catalyst.

volume [mL]	H_2O_2 [mol L^{-1}]	H_2O_2 [µl]	morin [mL]	H_2O [mL]
4.00	0.050	200	1.0	2.76
4.00	0.040	160	1.0	2.80
4.00	0.030	120	1.0	2.84
4.00	0.020	80	1.0	2.88
4.00	0.015	60	1.0	2.90
4.00	0.010	40	1.0	2.92
4.00	0.005	20	1.0	2.94
4.00	0.0025	10	1.0	2.95

Table 22: Concentration variation of H_2O_2 at 0.05 mmol L^{-1} morin with a constant concentration of catalyst.

volume [mL]	H_2O_2 [mol L^{-1}]	H_2O_2 [µl]	morin [mL]	H_2O [mL]
4.00	0.050	200	0.50	3.26
4.00	0.040	160	0.50	3.30
4.00	0.030	120	0.50	3.34
4.00	0.020	80	0.50	3.38
4.00	0.015	60	0.50	3.40
4.00	0.010	40	0.50	3.42
4.00	0.005	20	0.50	3.44
4.00	0.0025	10	0.50	3.45

These concentrations are used for the LH model at four different temperatures: 10, 20, 25, and 30 °C in a 50 mM carbonate buffer system. Additional measurements were done according to Table 19 and Table 21 at 20 °C in a 50 mM borax buffer. Here, in the case of the 12.5 mM carbonate buffer the raw data is provided by F. Polzer for the same experimental setup. Furthermore, measurements at standard concentrations of morin and H_2O_2 at 20 °C were done in a 0.05 mol L^{-1} 2-(cyclohexylamino)ethanesulfonic acid (CHES) buffer solution. Different concentrations of carbonate buffer (0.0125, 0.04063, 0.00313, 0.08563, 0.0275, 0.11, 0.065, 0.03687, 0.055, 0.0825, 0.0525, 0.04, and0.05 mol L^{-1}) and borax buffer (0.05, 0.04375, 0.0375, 0.025, and 0.0125 mol L^{-1}) are used at standard conditions to ascertain the dependence of the buffer system. Additionally measurements at standard concentrations with and without purging of nitrogen are done and also measurements without H_2O_2 with purged and unpurged stock solutions to investigate the influence of the air-oxygen on the morin oxidation.

Bibliography

[1] Astruc, D., Nanoparticles and Catalysis, Wiley-VCH Verlag GmbH & Co. KGaA, Weinheim, 2007.
[2] Haruta, M., Kobayashi, T., Sano, H., Yamada, N., Novel Gold Catalysts for the Oxidation of Carbon-Monoxide at a Temperature Far Below 0-Degrees-C, *Chem. Lett.*, **1987**, 405.
[3] Hutchings, G.J., Vapor-Phase Hydrochlorination of Acetylene - Correlation of Catalytic Activity of Supported Metal Chloride Catalysts, *J. Catal.*, **1985**, 96, 292.
[4] Hashmi, A.S.K., Hutchings, G.J., Gold catalysis, *Angew. Chem. Int. Ed.*, **2006**, 45, 7896.
[5] Corma, A., Garcia, H., Supported gold nanoparticles as catalysts for organic reactions, *Chem. Soc. Rev.*, **2008**, 37, 2096.
[6] Arcadi, A., Alternatice Synthetic Methodes through New Development in Catalsysis by Gold, *Chem. Rev.*, **2008**, 108, 60.
[7] Della Pina, C., Falletta, E., Prati, L., Rossi, M., Selective oxidation using gold, *Chem. Soc. Rev.*, **2008**, 37, 2077.
[8] Della Pina, C., Falletta, E., Rossi, M., Update on selective oxidation using gold, *Chem. Soc. Rev.*, **2012**, 41, 350.
[9] Claus, P., Heterogeneously catalysed hydrogenation using gold catalysts, *Appl. Catal., A*, **2005**, 291, 222.
[10] McEwan, L., Julius, M., Roberts, S., Fletcher, J.C.Q., A review of the use of gold catalysts in selective hydrogenation reactions, *Gold Bulletin*, **2010**, 43, 298.
[11] Balanta, A., Godard, C., Claver, C., Pd nanoparticles for C-C coupling reactions, *Chem. Soc. Rev.*, **2011**, 40, 4973.
[12] Fihri, A., Bouhrara, M., Nekoueishahraki, B., Basset, J.-M., Polshettiwar, V., Nanocatalysts for Szuzuki cross-coupling reactions, *Chem. Soc. Rev.*, **2011**, 40, 5181.
[13] Gude, K., Narayanan, R., Colloidal Supported Metal Nanoparticles (CSMNs) as Effective Nanocatalysts for Liquid-Phase Suzuki Cross-Coupling Reactions, *J. Phys. Chem. C*, **2011**, 115, 12716.
[14] Berhault, G., Bisson, L., Thomazeau, C., Verdon, C., Uzio, D., Preparation of nanostructured Pd particles using a seeding synthesis approach - Application to the selective hydrogenation of buta-1,3-diene, *Appl. Catal., A*, **2007**, 327, 32.
[15] Piccolo, L., Valcarcel, A., Bausach, M., Thomazeau, C., Uziob, D., Berhault, G., Tuning the shape of nanoparticles to control their catalytic properties: selective hydrogenation of 1,3-butadiene on Pd/Al(2)O(3), *Phys. Chem. Chem. Phys.*, **2008**, 10, 5504.
[16] Manbeck, K.A., Musselwhite, N.E., Carl, L.M., Kauffman, C.A., Lyons, O.D., Navin, J.K., Marsh, A.L., Factors affecting activity and selectivity during cyclohexanone hydrogenation with colloidal platinum nanocatalysts, *Appl. Catal., A*, **2010**, 384, 58.
[17] Chen, Z.J., Guan, Z.H., Li, M.R., Yang, Q.H., Li, C., Enhancement of the Performance of a Platinum Nanocatalyst Confined within Carbon Nanotubes for Asymmetric Hydrogenation, *Angew. Chem. Int. Ed.*, **2011**, 50, 4913.
[18] Ferrando, R., Jellinek, J., Johnston, R.L., Nanoalloys: from theory to applications of alloy clusters and nanoparticles, *Chem Rev*, **2008**, 108, 845.
[19] Peng, X.H., Pan, Q.M., Rempel, G.L., Bimetallic dendrimer-encapsulated nanoparticles as catalysts: a review of the research advances, *Chem. Soc. Rev.*, **2008**, 37, 1619.
[20] Wang, D., Li, Y., bimetallic nanocrystalls: liquid phase synthesis and catalytic applications, *Adv. Mater.*, **2011**, 23, 1044.

[21] Serna, P., Boronat, M., Corma, A., Tuning the Behavior of Au and Pt Catalysts for the Chemoselective Hydrogenation of Nitroaromatic Compounds, *Top. Catal.*, **2011**, 54, 439.
[22] Zahmakiran, M., Ozkar, S., Metal nanoparticles in liquid phase catalysis; from recent advances to future goals, *Nanoscale*, **2011**, 3, 3462.
[23] Myers, V.S., Weir, M.G., Carino, E.V., Yancey, D.F., Pande, S., Crooks, R.M., Dendrimer-encapsulated nanoparticles: New synthetic and characterization methods and catalytic applications, *Chemical Science*, **2011**, 2, 1632.
[24] Eastoe, J., Hollamby, M.J., Hudson, L., Recent advances in nanoparticle synthesis with reversed micelles, *Advances in Colloid and Interface Science*, **2006**, 128, 5.
[25] Roucoux, A., Schulz, J., Patin, H., Reduced transition metal colloids: A novel family of reusable catalysts?, *Chem. Rev.*, **2002**, 102, 3757.
[26] Grubbs, R.B., Roles of polymer ligands in nanoparticle stabilization, *Polym Rev*, **2007**, 47, 197.
[27] Meilikhov, M., Yusenko, K., Esken, D., Turner, S., Van Tendeloo, G., Fischer, R.A., Metals@MOFs - Loading MOFs with Metal Nanoparticles for Hybrid Functions, *Eur. J. Inorg. Chem.*, **2010**, 3701.
[28] Wildgoose, G.G., Banks, C.E., Compton, R.G., Metal nanopartictes and related materials supported on carbon nanotubes: Methods and applications, *Small*, **2006**, 2, 182.
[29] Campelo, J.M., Luna, D., Luque, R., Marinas, J.M., Romero, A.A., Sustainable Preparation of Supported Metal Nanoparticles and Their Applications in Catalysis, *Chemsuschem*, **2009**, 2, 18.
[30] Karg, M., Hellweg, T., New "smart" poly(NIPAM) microgels and nanoparticle microgel hybrids: Properties and advances in characterisation, *Current Opinion in Colloid & Interface Science*, **2009**, 14, 438.
[31] Li, H., Jo, J.K., Zhang, L., Ha, C.-S., Suh, H., Kim, I., A General and Efficient Route to Fabricate Carbon Nanotube-Metal Nanoparticles and Carbon Nanotube-Inorganic Oxides Hybrids, *Adv. Funct. Mater.*, **2010**, 20, 3864.
[32] Castillejos, E., Debouttiere, P.J., Roiban, L., Solhy, A., Martinez, V., Kihn, Y., Ersen, O., Philippot, K., Chaudret, B., Serp, P., An Efficient Strategy to Drive Nanoparticles into Carbon Nanotubes and the Remarkable Effect of Confinement on Their Catalytic Performance, *Angew. Chem. Int. Ed.*, **2009**, 48, 2529.
[33] Wu, B.H., Kuang, Y.J., Zhang, X.H., Chen, J.H., Noble metal nanoparticles/carbon nanotubes nanohybrids: Synthesis and applications, *Nano Today*, **2011**, 6, 75.
[34] Ballauff, M., Borisov, O., Polyelectrolyte brushes, *Current Opinion in Colloid & Interface Science*, **2006**, 11, 316.
[35] Ruhe, J., Ballauff, M., Biesalski, M., Dziezok, P., Grohn, F., Johannsmann, D., Houbenov, N., Hugenberg, N., Konradi, R., Minko, S., Motornov, M., Netz, R.R., Schmidt, M., Seidel, C., Stamm, M., Stephan, T., Usov, D., Zhang, H.N., Polyelectrolyte brushes, in: M. Schmidt (Ed.) Polyelectrolytes with Defined Molecular Architecture I, 2004, pp. 79.
[36] Bruening, M.L., Dotzauer, D.M., Jain, P., Ouyang, L., Baker, G.L., Creation of functional membranes using polyelectrolyte multilayers and polymer brushes, *Langmuir*, **2008**, 24, 7663.
[37] Kidambi, S., Dai, J.H., Li, J., Bruening, M.L., Selective hydrogenation by Pd nanoparticles embedded in polyelectrolyte multilayers, *Journal of the American Chemical Society*, **2004**, 126, 2658.
[38] Contreras-Caceres, R., Sanchez-Iglesias, A., Karg, M., Pastoriza-Santos, I., Perez-Juste, J., Pacifico, J., Hellweg, T., Fernandez-Barbero, A., Liz-Marzan, L.M., Encapsulation and growth of gold nanoparticles in thermoresponsive microgels, *Adv. Mater.*, **2008**, 20, 1666.

[39] Du, P.C., Mu, B., Wang, Y.J., Shi, H.G., Xue, D.S., Liu, P., Facile approach for temperature-responsive polymeric nanocapsules with movable magnetic cores, *Mater. Lett.*, **2011**, 65, 1579.
[40] Wu, Y., Zhang, T., Zheng, Z., Ding, X., Peng, Y., A facile approach to Fe(3)O(4)@Au nanoparticles with magnetic recyclable catalytic properties, *Mater. Res. Bull.*, **2010**, 45, 513.
[41] Guo, X., Ballauff, M., Spherical polyelectrolyte brushes: Comparison between annealed and quenched brushes, *Phys. Rev. E*, **2001**, 64, 051406.
[42] Sharma, G., Ballauff, M., Cationic spherical polyelectrolyte brushes as nanoreactors for the generation of gold particles, *Macromol. Rapid Commun.*, **2004**, 25, 547.
[43] Wang, X., Wu, S.A., Li, L., Zhang, R., Zhu, Y., Ballauff, M., Lu, Y., Guo, X.H., Synthesis of Spherical Polyelectrolyte Brushes by Photoemulsion Polymerization with Different Photoinitiators, *Ind. Eng. Chem. Res.*, **2011**, 50, 3564.
[44] Schrinner, M., Polzer, F., Mei, Y., Lu, Y., Haupt, B., Ballauff, M., Goldel, A., Drechsler, M., Preussner, J., Glatzel, U., Mechanism of the formation of amorphous gold nanoparticles within spherical polyelectrolyte brushes, *Macromol. Chem. Phys.*, **2007**, 208, 1542.
[45] Palioura, D., Armes, S.P., Anastasiadis, S.H., Vamvakaki, M., Metal nanocrystals incorporated within pH-responsive microgel particles, *Langmuir*, **2007**, 23, 5761.
[46] Butun, S., Sahiner, N., A versatile hydrogel template for metal nano particle preparation and their use in catalysis, *Polymer*, **2011**, 52, 4834.
[47] Esumi, K., Dendrimers for nanoparticle synthesis and dispersion stabilization, *Colloid Chemistry Ii*, **2003**, 227, 31.
[48] Solanki, J.N., Murthy, Z.V.P., Highly monodisperse and sub-nano silver particles synthesis via microemulsion technique, *Colloid Surf. B*, **2010**, 359, 31.
[49] Burda, C., Chen, X.B., Narayanan, R., El-Sayed, M.A., Chemistry and properties of nanocrystals of different shapes, *Chem. Rev.*, **2005**, 105, 1025.
[50] Ayyappan, S., Gopalan, R.S., Subbanna, G.N., Rao, C.N.R., Nanoparticles of Ag, Au, Pd, and Cu produced by alcohol reduction of the salts, *J. Mater. Res.*, **1997**, 12, 398.
[51] Cushing, B.L., Kolesnichenko, V.L., O'Connor, C.J., Recent advances in the liquid-phase syntheses of inorganic nanoparticles, *Chem. Rev.*, **2004**, 104, 3893.
[52] Dahl, J.A., Maddux, B.L.S., Hutchison, J.E., Toward greener nanosynthesis, *Chem. Rev.*, **2007**, 107, 2228.
[53] Sharma, G., Mei, Y., Lu, Y., Ballauff, M., Irrgang, T., Proch, S., Kempe, R., Spherical polyelectrolyte brushes as carriers for platinum nanoparticles in heterogeneous hydrogenation reactions, *J. Catal.*, **2007**, 246, 10.
[54] Proch, S., Mei, Y., Villanueva, J.M.R., Lu, Y., Karpov, A., Ballauff, M., Kempe, R., Suzuki- and Heck-type cross-coupling with palladium nanoparticles immobilized on spherical polyelectrolyte brushes, *Adv. Synth. Catal.*, **2008**, 350, 493.
[55] Lu, Y., Mei, Y., Drechsler, M., Ballauff, M., Thermosensitive core-shell particles as carriers for Ag nanoparticles: Modulating the catalytic activity by a phase transition in networks, *Angew. Chem. Int. Ed.*, **2006**, 45, 813.
[56] Mei, Y., Lu, Y., Polzer, F., Ballauff, M., Drechsler, M., Catalytic activity of palladium nanoparticles encapsulated in spherical polyelectrolyte brushes and core-shell microgels, *Chem. Mater.*, **2007**, 19, 1062.
[57] Mei, Y., Ballauff, M., Effect of counterions on the swelling of spherical polyelectrolyte brushes, *Eur Phys J E Soft Matter*, **2005**, 16, 341.
[58] Mei, Y., Sharma, G., Lu, Y., Ballauff, M., Drechsler, M., Irrgang, T., Kempe, R., High catalytic activity of platinum nanoparticles immobilized on spherical polyelectrolyte brushes, *Langmuir*, **2005**, 21, 12229.

[59] Schrinner, M., Proch, S., Mei, Y., Kempe, R., Miyajima, N., Ballauff, M., Stable bimetallic gold-platinum nanoparticles immobilized on spherical polyelectrolyte brushes: Synthesis, characterization, and application for the oxidation of alcohols, *Adv. Mater.*, **2008**, 20, 1928.
[60] Schrinner, M., Ballauff, M., Talmon, Y., Kauffmann, Y., Thun, J., Moller, M., Breu, J., Single Nanocrystals of Platinum Prepared by Partial Dissolution of Au-Pt Nanoalloys, *Science*, **2009**, 323, 617.
[61] Lu, Y., Hoffmann, M., Yelamanchili, R.S., Terrenoire, A., Schrinner, M., Drechsler, M., Moller, M.W., Breu, J., Ballauff, M., Well-Defined Crystalline TiO(2) Nanoparticles Generated and Immobilized on a Colloidal Nanoreactor, *Macromol. Chem. Phys.*, **2009**, 210, 377.
[62] Polzer, F., Kunz, D.A., Breu, J., Ballauff, M., Formation of Ultrathin Birnessite-Type Nanoparticles Immobilized on Spherical Polyelectrolyte Brushes, *Chemistry of Materials*, **2010**, 22, 2916.
[63] Cheng, F.Y., Chen, J., Gou, X.L., Shen, P.W., High-power alkaline Zn-MuO(2) batteries using gamma-MnO2 nanowires/nanotubes and electrolytic zinc powder, *Adv. Mater.*, **2005**, 17, 2753.
[64] Osada, M., Sasaki, T., Exfoliated oxide nanosheets: new solution to nanoelectronics, *J. Mater. Chem.*, **2009**, 19, 2503.
[65] Kang, J.H., Paek, S.M., Hwang, S.J., Choy, J.H., Pre-swelled nanostructured electrode for lithium ion battery: TiO(2)-pillared layered MnO(2), *J. Mater. Chem.*, **2010**, 20, 2033.
[66] Brock, S.L., Duan, N., Tian, Z.R., Giraldo, O., Zhou, H., Suib, S.L., A Review of Porous Manganese Oxide Materials, *Chem. Mater.*, **1998**, 10, 2619.
[67] Cao, H., Suib, S.L., Highly Efficient Heterogeneous Photooxidation of 2-Propanol to Acetone with Amorphous Manganese Oxide Catalysts, *J. Am. Chem. Soc.*, **1994**, 116, 5334.
[68] Lee, G.H., Huh, S.H., Jeong, J.W., Choi, B.J., Kim, S.H., Ri, H.C., Anomalous magnetic properties of MnO nanoclusters, *J. Am. Chem. Soc.*, **2002**, 124, 12094.
[69] Shen, Y.F., Zerger, R.P., Deguzman, R.N., Suib, S.L., McCurdy, L., Potter, D.I., O'Young C, L., Manganese oxide octahedral molecular sieves: preparation, characterization, and applications, *Science*, **1993**, 260, 511.
[70] Tang, W.P., Kanoh, H.F., Yang, X.J., Ooi, K., Preparation of plate-form manganese oxide by selective lithium extraction from monoclinic Li2MnO3 under hydrothermal conditions, *Chem Mater*, **2000**, 12, 3271.
[71] Debart, A., Paterson, A.J., Bao, J., Bruce, P.G., Alpha-MnO2 nanowires: a catalyst for the O2 electrode in rechargeable lithium batteries, *Angew. Chem. Int. Ed.*, **2008**, 47, 4521.
[72] Zhang, W.X., Wang, H., Yang, Z.H., Wang, F., Promotion of H2O2 decomposition activity over beta-MnO2 nanorod catalysts, *Colloid Surf. A*, **2007**, 304, 60.
[73] Broughton, D.B., Wentworth, R.L., Mechanism of Decomposition of Hydrogen Peroxide Solutions with Manganese Dioxide .1., *J. Am. Chem. Soc.*, **1947**, 69, 741.
[74] Do, S.H., Batchelor, B., Lee, H.K., Kong, S.H., Hydrogen peroxide decomposition on manganese oxide (pyrolusite): kinetics, intermediates, and mechanism, *Chemosphere*, **2009**, 75, 8.
[75] Pradhan, N., Pal, A., Pal, T., Silver nanoparticle catalyzed reduction of aromatic nitro compounds, *Colloid Surf. B*, **2002**, 196, 247.
[76] Esumi, K., Miyamoto, K., Yoshimura, T., Comparison of PAMAM-Au and PPI-Au nanocomposites and their catalytic activity for reduction of 4-nitrophenol, *J. Colloid Interface Sci.*, **2002**, 254, 402.

[77] Shine, H.J., Mallory, H.E., Reduction of Aromatic Nitro Compounds by Potassium Borohydride, *J. Org. Chem.*, **1962**, 27, 2390.
[78] Ghosh, S.K., Mandal, M., Kundu, S., Nath, S., Pal, T., Bimetallic Pt-Ni nanoparticles can catalyze reduction of aromatic nitro compounds by sodium borohydride in aqueous solution, *Appl. Catal., A*, **2004**, 268, 61.
[79] Hayakawa, K., Yoshimura, T., Esumi, K., Preparation of gold-dendrimer nanocomposites by laser irradiation and their catalytic reduction of 4-nitrophenol, *Langmuir*, **2003**, 19, 5517.
[80] Zhang, H., Li, X., Chen, G., Ionic liquid-facilitated synthesis and catalytic activity of highly dispersed Ag nanoclusters supported on TiO(2), *J. Mater. Chem.*, **2009**, 19, 8223.
[81] Khalavka, Y., Becker, J., Soennichsen, C., Synthesis of Rod-Shaped Gold Nanorattles with Improved Plasmon Sensitivity and Catalytic Activity, *J. Am. Chem. Soc.*, **2009**, 131, 1871.
[82] Dannacher, J.J., Catalytic bleach: Most valuable applications for smart oxidation chemistry, *J. Mol. Catal. A-Chem.*, **2006**, 251, 159.
[83] Wieprecht, T., Heinz, U., Xia, J., Schlingloff, G., Dannacher, J., Terpyridine-manganese complexes: A new class of bleach catalysts for detergent applications, *J. Surfactants Deterg.*, **2004**, 7, 59.
[84] Colombini, M.P., Andreotti, A., Baraldi, C., Degano, I., Łucejko, J.J., Colour fading in textiles: A model study on the decomposition of natural dyes, *Microchem. J.*, **2007**, 85, 174.
[85] Osman, A., Makris, D.P., Oxidation of morin (2',3,4',5,7-Pentahydroxyfavone) with a peroxidase homogenate from onion, *IFRJ*, **2011**, 18, 1085.
[86] Zenkevich, I.G., Eshchenko, A.Y., Makarova, S.V., Vitenberg, A.G., Dobryakov, Y.G., Utsal, V.A., Identification of the products of oxidation of quercetin by air oxygen at ambient temperature, *Molecules*, **2007**, 12, 654.
[87] Zhou, A.L., Sadik, O.A., Comparative Analysis of Quercetin Oxidation by Electrochemical, Enzymatic, Autoxidation, and Free Radical Generation Techniques: A Mechanistic Study, *J. Agric. Food. Chem.*, **2008**, 56, 12081.
[88] Osman, A., Makris, D.P., Kefalas, P., Investigation on biocatalytic properties of a peroxidase-active homogenate from onion solid wastes: An insight into quercetin oxidation mechanism, *Process Biochem.*, **2008**, 43, 861.
[89] Makris, D.P., Rossiter, J.T., Hydroxyl free radical-mediated oxidative degradation of quercetin and morin: A preliminary investigation, *J. Food Compos. Anal.*, **2002**, 15, 103.
[90] Mabry, T.J., Markham, K.R., Thomas, M.B., The Systematic Identification of Flavonoids, 1970.
[91] Advincula, R.C., Brittain, W.J., Caster, K.C., Rühe, J., Polymer Brushes, in, WILEY-VCH Verlag GmBH & Co. KGaA, Weinheim, 2004.
[92] Jusufi, A., Likos, C.N., Ballauff, M., Counterion distributions and effective interactions of spherical polyelectrolyte brushes, *Colloid. Polym. Sci.*, **2004**, 282, 910.
[93] Guo, X., Ballauff, M., Spatial dimensions of colloidal polyelectrolyte brushes as determined by dynamic light scattering, *Langmuir*, **2000**, 16, 8719.
[94] Wittemann, A., Drechsler, M., Talmon, Y., Ballauff, M., High Elongation of Polyelectrolyte Chains in the Osmotic Limit of Spherical Polyelectrolyte Brushes: A Study by Cryogenic Transmission Electron Microscopy, *J. Am. Chem. Soc.*, **2005**, 127, 9688.
[95] de Robillard, Q., Guo, X., Ballauff, M., Narayanan, T., Spatial Correlation of Spherical Polyelectrolyte Brushes in Salt-Free Solution As Observed by Small-Angle X-ray Scattering, *Macromolecules*, **2000**, 33, 9109.

[96] Dingenouts, N., Merkle, R., Guo, X., Narayanan, T., Goerigk, G., Ballauff, M., Use of anomalous small-angle X-ray scattering for the investigation of highly charged colloids, *J. Appl. Crystallogr.*, **2003**, 36, 578.
[97] Lu, Y., Lunkenbein, T., Preussner, J., Proch, S., Breu, J., Kempe, R., Ballauff, M., Composites of Metal Nanoparticles and TiO(2) Immobilized in Spherical Polyelectrolyte Brushes, *Langmuir*, **2010**, 26, 4176.
[98] Vannice, M.A., Reactions, Springer Science + Buisness Media: Philadelphia, 2005.
[99] Wedler, G., Lehrbuch der Physikalischen Chemie, Wiles-VCH, 1997.
[100] Sips, R., ON THE STRUCTURE OF A CATALYST SURFACE, *J. Chem. Phys.*, **1948**, 16, 490.
[101] Jaroniec, M., Derylo, A., Marczewski, A., THE LANGMUIR-FREUNDLICH EQUATION IN ADSORPTION FROM DILUTE-SOLUTIONS ON SOLIDS, *Monatsh. Chem.*, **1983**, 114, 393.
[102] Rill, C., Kolar, Z.I., Kickelbick, G., Wolterbeek, H.T., Peters, J.A., Kinetics and thermodynamics of adsorption on hydroxyapatite of the [160Tb]terbium complexes of the bone-targeting ligands DOTP and BPPED, *Langmuir*, **2009**, 25, 2294.
[103] Malek, A., Farooq, S., Comparison of isotherm models for hydrocarbon adsorption on activated carbon, *AlChE J.*, **1996**, 42, 3191.
[104] Imbihl, R., Cox, M.P., Ertl, G., Kinetic Oscillations in the Catalytic Cooxidation on Pt(100) - Experiments, *J. Chem. Phys.*, **1986**, 84, 3519.
[105] Somorjai, G.A., Li, Y., Surface Chemistry and Catalysis, Wiley, Hoboken, New Jersey, 2010.
[106] Imbihl, R., Ertl, G., Oscillatory Kinetics in Heterogeneous Catalysis, *Chem. Rev.*, **1995**, 95, 697.
[107] Jakubith, S., Rotermund, H.H., Engel, W., Vonoertzen, A., Ertl, G., Spatiotemporal Concentration Patterns in a Surface-Reaction - Propagating and Standing Waves, Rotating Spirals, and Turbulence, *Phys. Rev. Lett.*, **1990**, 65, 3013.
[108] Pasteur, A.T., Dixonwarren, S.J., King, D.A., HYDROGEN DISSOCIATION ON PT(100) - NONLINEAR POWER-LAW IN HYDROGEN-INDUCED RESTRUCTURING, *J. Chem. Phys.*, **1995**, 103, 2251.
[109] Hopkinson, A., Bradley, J.M., Guo, X., King, D.A., Nonlinear island growth dynamics in adsorbate-induced restructuring of quasihexagonal reconstructed Pt{100} by CO, *Phys. Rev. Lett.*, **1993**, 71, 1597.
[110] van Beurden, P., Bunnik, B.S., Kramer, G.J., Borg, A., Mechanism and dynamics of the CO-induced lifting of the Pt(100) surface reconstruction, *Phys. Rev. Lett.*, **2003**, 90, 066106.
[111] van Beurden, P., Kramer, G.J., Atomistic mechanisms for the (1x1)reversible arrow hex surface phase transformations of Pt(100), *J. Chem. Phys.*, **2004**, 121, 2317.
[112] Esumi, K., Isono, R., Yoshimura, T., Preparation of PAMAM- and PPI-metal (silver, platinum, and palladium) nanocomposites and their catalytic activities for reduction of 4-nitrophenol, *Langmuir*, **2004**, 20, 237.
[113] Endo, T., Kuno, T., Yoshimura, T., Esumi, K., Preparation and catalytic activity of Au-Pd, Au-Pt, and Pt-Pd binary metal dendrimer nanocomposites, *J. Nanosci. Nanotechnol.*, **2005**, 5, 1875.
[114] Wu, H., Liu, Z., Wang, X., Zhao, B., Zhang, J., Li, C., Preparation of hollow capsule-stabilized gold nanoparticles through the encapsulation of the dendrimer, *J. Colloid Interface Sci.*, **2006**, 302, 142.
[115] Kundu, S., Mandal, M., Ghosh, S.K., Pal, T., Photochemical deposition of SERS active silver nanoparticles on silica gel, *J. Photochem. Photobiol. A-Chem.*, **2004**, 162, 625.

[116] Pich, A., Karak, A., Lu, Y., Ghosh, A.K., Adler, H.-J.P., Tuneable catalytic properties of hybrid microgels containing gold nanoparticles, *J. Nanosci. Nanotechnol.*, **2006**, 6, 3763.
[117] Yang, H., Nagai, K., Abe, T., Homma, H., Norimatsu, T., Ramaraj, R., Enhanced Catalytic Activity of Gold Nanoparticles Doped in a Mesoporous Organic Gel Based on Polymeric Phloroglucinol Carboxylic Acid-Formaldehyde, *ACS. Appl. Mater. Inter.*, **2009**, 1, 1860.
[118] Lu, Y., Yuan, J., Polzer, F., Drechsler, M., Preussners, J., In Situ Growth of Catalytic Active Au - Pt Bimetallic Nanorods in Thermoresponsive Core - Shell Microgels, *ACS Nano*, **2010**, 4, 7078.
[119] Sahiner, N., Ozay, H., Ozay, O., Aktas, N., A soft hydrogel reactor for cobalt nanoparticle preparation and use in the reduction of nitrophenols, *Appl. Catal., B*, **2010**, 101, 137.
[120] Zhang, J.-T., Wei, G., Keller, T.F., Gallagher, H., Stoetzel, C., Mueller, F.A., Gottschaldt, M., Schubert, U.S., Jandt, K.D., Responsive Hybrid Polymeric/Metallic Nanoparticles for Catalytic Applications, *Macromol. Mater. Eng.*, **2010**, 295, 1049.
[121] Sahiner, N., Ozay, H., Ozay, O., Aktas, N., New catalytic route: Hydrogels as templates and reactors for in situ Ni nanoparticle synthesis and usage in the reduction of 2-and 4-nitrophenols, *Appl. Catal., A*, **2010**, 385, 201.
[122] Wang, Y., Wei, G.W., Zhang, W.Q., Jiang, X.W., Zheng, P.W., Shi, L.Q., Dong, A.J., Responsive catalysis of thermoresponsive micelle-supported gold nanoparticles, *J. Mol. Catal. A-Chem.*, **2007**, 266, 233.
[123] Chen, X., Zhao, D., An, Y., Zhang, Y., Cheng, J., Wang, B., Shi, L., Formation and catalytic activity of spherical composites with surfaces coated with gold nanoparticles, *J. Colloid Interface Sci.*, **2008**, 322, 414.
[124] Chen, X., An, Y.L., Zhao, D.Y., He, Z.P., Zhang, Y., Cheng, J., Shi, L.Q., Core-shell-corona Au-micelle composites with a tunable smart hybrid shell, *Langmuir*, **2008**, 24, 8198.
[125] Chen, X., Zhao, D., An, Y., Shi, L., Hou, W., Chen, L., Catalytic properties of gold nanoparticles immobilized on the surfaces of nanocarriers, *J. Nanopart. Res.*, **2010**, 12, 1877.
[126] Lu, Y., Mei, Y., Walker, R., Ballauff, M., Drechsler, M., 'Nano-tree' - type spherical polymer brush particles as templates for metallic nanoparticles, *Polymer*, **2006**, 47, 4985.
[127] Lu, Y., Mei, Y., Schrinner, M., Ballauff, M., Moeller, M.W., In situ formation of Ag nanoparticles in spherical polyacrylic acid brushes by UV irradiation, *J. Phys. Chem. C*, **2007**, 111, 7676.
[128] Zhang, M., Liu, L., Wu, C., Fu, G., Zhao, H., He, B., Synthesis, characterization and application of well-defined environmentally responsive polymer brushes on the surface of colloid particles, *Polymer*, **2007**, 48, 1989.
[129] Lu, Y., Yu, M., Drechsler, M., Ballauff, M., Ag nanocomposite particles: Preparation, characterization and application, *Macromol. Symp.*, **2007**, 254, 97.
[130] Graetzel, M., Frank, A.J., Interfacial electron-transfer reactions in colloidal semiconductor dispersions. Kinetic analysis, *The Journal of Physical Chemistry*, **1982**, 86, 2964.
[131] Panigrahi, S., Basu, S., Praharaj, S., Pande, S., Jana, S., Pal, A., Ghosh, S.K., Pal, T., Synthesis and size-selective catalysis by supported gold nanoparticles: Study on heterogeneous and homogeneous catalytic process, *J. Phys. Chem. C*, **2007**, 111, 4596.
[132] Harish, S., Mathiyarasu, J., Phani, K.L.N., Yegnaraman, V., Synthesis of Conducting Polymer Supported Pd Nanoparticles in Aqueous Medium and Catalytic Activity Towards 4-Nitrophenol Reduction, *Catal. Lett.*, **2009**, 128, 197.

[133] Behrens, S., Heyman, A., Maul, R., Essig, S., Steigerwald, S., Quintilla, A., Wenzel, W., Buerck, J., Dgany, O., Shoseyov, O., Constrained Synthesis and Organization of Catalytically Active Metal Nanoparticles by Self-Assembled Protein Templates, *Adv. Mater.*, **2009**, 21, 3515.
[134] Bhandari, R., Knecht, M.R., Effects of the Material Structure on the Catalytic Activity of Peptide-Templated Pd Nanomaterials, *ACS Catal.*, **2011**, 1, 89.
[135] Halder, A., Patra, S., Viswanath, B., Munichandraiah, N., Ravishankar, N., Porous, catalytically active palladium nanostructures by tuning nanoparticle interactions in an organic medium, *Nanoscale*, **2011**, 3, 725.
[136] Arora, S., Kapoor, P., Singla, M.L., Catalytic studies of palladium nanoparticles immobilized on alumina synthesized by a simple physical precipitation method, *React. Kinet. Mech. Cat.*, **2010**, 99, 157.
[137] Yuan, J.Y., Schacher, F., Drechsler, M., Hanisch, A., Lu, Y., Ballauff, M., Muller, A.H.E., Stimuli-Responsive Organosilica Hybrid Nanowires Decorated with Metal Nanoparticles, *Chem. Mater.*, **2010**, 22, 2626.
[138] Murugadoss, A., Chattopadhyay, A., Surface area controlled differential catalytic activities of one-dimensional chain-like arrays of gold nanoparticles, *J. Phys. Chem. C*, **2008**, 112, 11265.
[139] Han, J., Li, L., Guo, R., Novel Approach to Controllable Synthesis of Gold Nanoparticles Supported on Polyaniline Nanofibers, *Macromolecules*, **2010**, 43, 10636.
[140] Liu, J.C., Qin, G.W., Raveendran, P., Kushima, Y., Facile "green" synthesis, characterization, and catalytic function of beta-D-glucose-stabilized Au nanocrystals, *Chem. Eur. J.*, **2006**, 12, 2132.
[141] Kuroda, K., Ishida, T., Haruta, M., Reduction of 4-nitrophenol to 4-aminophenol over Au nanoparticles deposited on PMMA, *J. Mol. Catal. A-Chem.*, **2009**, 298, 7.
[142] Wu, S.-H., Tseng, C.-T., Lin, Y.-S., Lin, C.-H., Hung, Y., Mou, C.-Y., Catalytic nano-rattle of Au@hollow silica: towards a poison-resistant nanocatalyst, *J. Mater. Chem.*, **2011**, 21, 789.
[143] Wu, H., Huang, X., Gao, M., Liao, X., Shi, B., Polyphenol-grafted collagen fiber as reductant and stabilizer for one-step synthesis of size-controlled gold nanoparticles and their catalytic application to 4-nitrophenol reduction, *Green Chem.*, **2011**, 13, 651.
[144] Signori, A.M., Santos, K.d.O., Eising, R., Albuquerque, B.L., Giacomelli, F.C., Domingos, J.B., Formation of Catalytic Silver Nanoparticles Supported on Branched Polyethyleneimine Derivatives, *Langmuir*, **2010**, 26, 17772.
[145] Eising, R., Signori, A.M., Fort, S., Domingos, J.B., Development of Catalytically Active Silver Colloid Nanoparticles Stabilized by Dextran, *Langmuir*, **2011**, 27, 11860.
[146] Lu, Y., Spyra, P., Mei, Y., Ballauff, M., Pich, A., Composite hydrogels: Robust carriers for catalytic nanoparticles, *Macromol. Chem. Phys.*, **2007**, 208, 254.
[147] Murugadoss, A., Chattopadhyay, A., A 'green' chitosan-silver nanoparticle composite as a heterogeneous as well as micro-heterogeneous catalyst, *Nanotechnology*, **2008**, 19, 9.
[148] Yu, M., Lu, Y., Schrinner, M., Polzer, E., Ballauff, M., Spherical polyelectrolyte brushes as carriers for catalytically active metal nanoparticles, *Macromol. Symp.*, **2007**, 254, 42.
[149] Lu, Y., Mei, Y., Schrinner, M., Ballauff, M., Moller, M.W., In situ formation of Ag nanoparticles in spherical polyacrylic acid brushes by UV irradiation, *J. Phys. Chem. C*, **2007**, 111, 7676.
[150] Lu, Y., Mei, Y., Ballauff, M., Drechsler, M., Thermosensitive core-shell particles as carrier systems for metallic nanoparticles, *J. Phys. Chem. B*, **2006**, 110, 3930.

[151] Jana, S., Ghosh, S.K., Nath, S., Pande, S., Praharaj, S., Panigrahi, S., Basu, S., Endo, T., Pal, T., Synthesis of silver nano shell-coated cationic polystyrene beads: A solid phase catalyst for the reduction of 4-nitrophenol, *Appl. Catal., A*, **2006**, 313, 41.
[152] Saha, S., Pal, A., Kundu, S., Basu, S., Pal, T., Photochemical Green Synthesis of Calcium-Alginate-Stabilized Ag and Au Nanoparticles and Their Catalytic Application to 4-Nitrophenol Reduction, *Langmuir*, **2010**, 26, 2885.
[153] Manesh, K.M., Gopalan, A.I., Lee, K.-P., Komathi, S., Silver nanoparticles distributed into polyaniline bridged silica network: A functional nanocatalyst having synergistic influence for catalysis, *Catal. Commun.*, **2010**, 11, 913.
[154] Shin, K.S., Choi, J.-Y., Park, C.S., Jang, H.J., Kim, K., Facile Synthesis and Catalytic Application of Silver-Deposited Magnetic Nanoparticles, *Catal. Lett.*, **2009**, 133, 1.
[155] Chang, Y.-C., Chen, D.-H., Catalytic reduction of 4-nitrophenol by magnetically recoverable Au nanocatalyst, *J. Hazard. Mater.*, **2009**, 165, 664.
[156] Zeng, J., Zhang, Q., Chen, J., Xia, Y., A Comparison Study of the Catalytic Properties of Au-Based Nanocages, Nanoboxes, and Nanoparticles, *Nano Lett.*, **2010**, 10, 30.
[157] Mahmoud, M.A., Snyder, B., El-Sayed, M.A., Polystyrene Microspheres: Inactive Supporting Material for Recycling and Recovering Colloidal Nanocatalysts in Solution, *J. Phys. Chem. Lett.*, **2010**, 1, 28.
[158] Mahmoud, M.A., Saira, F., El-Sayed, M.A., Experimental Evidence For The Nanocage Effect In Catalysis With Hollow Nanoparticles, *Nano Lett.*, **2010**, 10, 3764.
[159] Bond, G.C., Keane, M.A., Kral, H., Lercher, J.A., Compensation phenomena in heterogeneous catalysis: General principles and a possible explanation, *Cat. Rev. - Sci. Eng.*, **2000**, 42, 323.
[160] Rooney, J.J., The extended Eyring kinetic equation and the compensation effect in catalysis, *J. Mol. Catal. A-Chem.*, **1998**, 129, 131.
[161] Bond, G.C., Kinetics of alkane reactions on metal catalysts: activation energies and the compensation effect, *Catal. Today*, **1999**, 49, 41.
[162] Bond, G., Source of the catalytic activity of gold nanoparticles, *Gold Bulletin*, **2010**, 43, 88.
[163] Bligaard, T., Honkala, K., Logadottir, A., Norskov, J.K., Dahl, S., Jacobsen, C.J.H., On the compensation effect in heterogeneous catalysis, *J. Phys. Chem. B*, **2003**, 107, 9325.
[164] Jana, S., Pal, T., Synthesis, characterization and catalytic application of silver nanoshell coated functionalized polystyrene beads, *J. Nanosci. Nanotechnol.*, **2007**, 7, 2151.
[165] Sarkar, S., Sinha, A.K., Pradhan, M., Basu, M., Negishi, Y., Pal, T., Redox Transmetalation of Prickly Nickel Nanowires for Morphology Controlled Hierarchical Synthesis of Nickel/Gold Nanostructures for Enhanced Catalytic Activity and SERS Responsive Functional Material, *J. Phys. Chem. C*, **2011**, 115, 1659.
[166] Wei, D., Ye, Y., Jia, X., Yuan, C., Qian, W., Chitosan as an active support for assembly of metal nanoparticles and application of the resultant bioconjugates in catalysis, *Carbohydr. Res.*, **2010**, 345, 74.
[167] Huang, J., Vongehr, S., Tang, S., Meng, X., Highly Catalytic Pd-Ag Bimetallic Dendrites, *J. Phys. Chem. C*, **2010**, 114, 15005.
[168] Mahmoud, M.A., El-Sayed, M.A., Time dependence and signs of the shift of the surface plasmon resonance frequency in nanocages elucidate the nanocatalysis mechanism in hollow nanoparticles, *Nano Lett.*, **2011**, 11, 946.
[169] Wu, K.L., Wei, X.W., Zhou, X.M., Wu, D.H., Liu, X.W., Ye, Y., Wang, Q., NiCo(2) Alloys: Controllable Synthesis, Magnetic Properties, and Catalytic Applications in Reduction of 4-Nitrophenol, *J Phys Chem C*, **2011**, 115, 16268.

[170] Han, J., Dai, J., Li, L.Y., Fang, P., Guo, R., Highly Uniform Self-Assembled Conducting Polymer/Gold Fibrous Nanocomposites: Additive-Free Controllable Synthesis and Application as Efficient Recyclable Catalysts, *Langmuir*, **2011**, 27, 2181.
[171] Gao, Y., Ding, X., Zheng, Z., Cheng, X., Peng, Y., Template-free method to prepare polymer nanocapsules embedded with noble metal nanoparticles, *Chem Commun (Camb)*, **2007**, 3720.
[172] Wang, S.N., Zhang, M.C., Zhang, W.Q., Yolk-Shell Catalyst of Single Au Nanoparticle Encapsulated within Hollow Mesoporous Silica Microspheres, *ACS Catal.*, **2011**, 1, 207.
[173] Huang, T., Meng, F., Qi, L., Facile Synthesis and One-Dimensional Assembly of Cyclodextrin-Capped Gold Nanoparticles and Their Applications in Catalysis and Surface-Enhanced Raman Scattering, *J. Phys. Chem. C*, **2009**, 113, 13636.
[174] Liu, Z.L., Wang, X.D., Wu, H.Y., Li, C.X., Silver nanocomposite layer-by-layer films based on assembled polyelectrolyte/dendrimer, *J. Colloid Interface Sci.*, **2005**, 287, 604.
[175] Zhou, X., Xu, W., Liu, G., Panda, D., Chen, P., Size-dependent catalytic activity and dynamics of gold nanoparticles at the single-molecule level, *J. Am. Chem. Soc.*, **2010**, 132, 138.
[176] Bielejewska, A., Bylina, A., Duszczyk, K., Fiałkowski, M., Hołyst, R., Evaluation of Ligand-Selector Interaction from Effective Diffusion Coefficient, *Anal. Chem.*, **2010**, 82, 5463.
[177] Guella, G., Patton, B., Miotello, A., Kinetic features of the platinum catalyzed hydrolysis of sodium borohydride from B-11 NMR measurements, *J. Phys. Chem. C*, **2007**, 111, 18744.
[178] Liu, B.H., Li, Z.P., A review: Hydrogen generation from borohydride hydrolysis reaction, *J. Power Sources*, **2009**, 187, 527.
[179] Jiang, H.-L., Akita, T., Ishida, T., Haruta, M., Xu, Q., Synergistic Catalysis of Au@Ag Core-Shell Nanoparticles Stabilized on Metal-Organic Framework, *J. Am. Chem. Soc.*, **2011**, 133, 1304.
[180] Goswami, N., Saha, R., Pal, S.K., Protein-assisted synthesis route of metal nanoparticles: exploration of key chemistry of the biomolecule, *J. Nanopart. Res.*, **2011**, 13, 5485.
[181] Zhang, J.S., Delgass, W.N., Fisher, T.S., Gore, J.P., Kinetics of Ru-catalyzed sodium borohydride hydrolysis, *J. Power Sources*, **2007**, 164, 772.
[182] Driver, S.M., Zhang, T.F., King, D.A., Massively cooperative adsorbate-induced surface restructuring and nanocluster formation, *Angew. Chem. Int. Ed.*, **2007**, 46, 700.
[183] Pierce, M.S., Chang, K.C., Hennessy, D.C., Komanicky, V., Menzel, A., You, H., CO-induced lifting of Au(001) surface reconstruction, *J. Phys. Chem. C*, **2008**, 112, 2231.
[184] Zhang, W.X., Yang, Z.H., Wang, X., Zhang, Y.C., Wen, X.G., Yang, S.H., Large-scale synthesis of beta-MnO2 nanorods and their rapid and efficient catalytic oxidation of methylene blue dye, *Catal. Commun.*, **2006**, 7, 408.
[185] Liu, Y., Luo, M.F., Wei, Z.B., Xin, Q., Ying, P.L., Li, C., Catalytic oxidation of chlorobenzene on supported manganese oxide catalysts, *Appl. Catal., B*, **2001**, 29, 61.
[186] Li, X.Q., Zhou, L.P., Gao, J., Miao, H., Zhang, H., Xu, J., Synthesis of Mn(3)O(4) nanoparticles and their catalytic applications in hydrocarbon oxidation, *Powder Technol.*, **2009**, 190, 324.
[187] Qi, B., Lou, L.-L., Yu, K., Bian, W., Liu, S., Selective epoxidation of alkenes with hydrogen peroxide over efficient and recyclable manganese oxides, *Catal. Commun.*, **2011**, 15, 52.

[188] Espinal, L., Suib, S.L., Rusling, J.F., Electrochemical catalysis of styrene epoxidation with films of MnO(2) nanoparticles and H(2)O(2), *J. Am. Chem. Soc.*, **2004**, 126, 7676.
[189] Topalovic, T., Catalytic Bleaching of Cotton: Molecular and Macroscopic Aspects, in, University of Twente, Netherlands, 2007.
[190] Topalovic, T., Nierstrasz, V.A., Warmoeskerken, M.M.C.G., Model System for Mechanistic Study of Catalytic Bleaching of Cotton, *Fiber. Polym.*, **2010**, 11, 72.
[191] Rothbart, S., Ember, E., van Eldik, R., Comparative study of the catalytic activity of [Mn(II)(bpy)2Cl2] and [Mn2(III/IV)(mu-O)2(bpy)4](ClO4)3 in the H2O2 induced oxidation of organic dyes in carbonate buffered aqueous solution, *Dalton Trans.*, **2010**, 39, 3264.
[192] Ember, E., Gazzaz, H.A., Rothbart, S., Puchta, R., van Eldik, R., Mn(II)-A fascinating oxidation catalyst: Mechanistic insight into the catalyzed oxidative degradation of organic dyes by H(2)O(2), *Appl. Catal., B*, **2010**, 95, 179.
[193] Zhou, H., Shen, Y.F., Wang, J.Y., Chen, X., O'Young, C.L., Suib, S.L., Studies of decomposition of H2O2 over manganese oxide octahedral molecular sieve materials, *J Catal.*, **1998**, 176, 321.
[194] Polzer, F., Wunder, S., Lu, Y., Ballauff, M., Oxidation of an organic dye catalyzed by MnOx nanoparticles, *J. Catal.*, **2012**.
[195] Colombini, M.P., Andreotti, A., Baraldi, C., Degano, I., Lucejko, J.J., Colour fading in textiles: A model study on the decomposition of natural dyes, *Microchem. J.*, **2007**, 85, 174.
[196] Kitajima, N., Fukuzumi, S., Ono, Y., Formation of Superoxide Ion during Decomposition of Hydrogen-Peroxide on Supported Metal-Oxides, *J Phys Chem-Us*, **1978**, 82, 1505.
[197] ULLMANN'S Encyclopedia of Industrial Chemistry, 5th edition ed., Wiley, Weinheim, 1989.
[198] Lee, K.Y., Hwang, J., Lee, Y.W., Kim, J., Han, S.W., One-step synthesis of gold nanoparticles using azacryptand and their applications in SERS and catalysis, *J. Colloid Interface Sci.*, **2007**, 316, 476.
[199] Zhang, L., Swift, J., Butts, C.A., Yerubandi, V., Dmochowski, I.J., Structure and activity of apoferritin-stabilized gold nanoparticles, *J. Inorg. Biochem.*, **2007**, 101, 1719.
[200] Kumar, S.S., Kumar, C.S., Mathiyarasu, J., Phani, K.L., Stabilized gold nanoparticles by reduction using 3,4-ethylenedioxythiophene-polystyrenesulfonate in aqueous solutions: Nanocomposite formation, stability, and application in catalysis, *Langmuir*, **2007**, 23, 3401.
[201] Rashid, M.H., Mandal, T.K., Templateless synthesis of polygonal gold nanoparticles: An unsupported and reusable catalyst with superior activity, *Adv. Funct. Mater.*, **2008**, 18, 2261.
[202] Tang, R., Liao, X.-P., Shi, B., Heterogeneous gold nanoparticles stabilized by collagen and their application in catalytic reduction of 4-nitrophenol, *Chem. Lett.*, **2008**, 37, 834.
[203] Lee, K.Y., Lee, Y.W., Kwon, K., Heo, J., Kim, J., Han, S.W., One-step fabrication of gold nanoparticles-silica composites with enhanced catalytic activity, *Chem. Phys. Lett.*, **2008**, 453, 77.
[204] Wang, Y., Wei, G., Wen, F., Zhang, X., Zhang, W., Shi, L., Synthesis of gold nanoparticles stabilized with poly(N-isopropylacrylamide)-co-poly(4-vinyl pyridine) colloid and their application in responsive catalysis, *J. Mol. Catal. A-Chem.*, **2008**, 280, 1.
[205] Selvaraju, T., Das, J., Jo, K., Kwon, K., Huh, C.H., Kim, T.K., Yang, H., Nanocatalyst-based assay using DNA-conjugated Au nanoparticles for electrochemical DNA detection, *Langmuir*, **2008**, 24, 9883.

[206] Chen, X., Zhao, D., Zhao, L., An, Y., Ma, R., Shi, L., He, Q., Chen, L., Optic and catalytic properties of gold nanoparticles tuned by homopolymers, *Sci. China Ser. B-Chem.*, **2009**, 52, 1372.
[207] Juarez, J., Cambon, A., Goy-Lopez, S., Topete, A., Taboada, P., Mosquera, V., Obtention of Metallic Nanowires by Protein Biotemplating and Their Catalytic Application, *J. Phys. Chem. Lett.*, **2010**, 1, 2680.
[208] Li, L., Wang, Z., Huang, T., Xie, J., Qi, L., Porous Gold Nanobelts Templated by Metal-Surfactant Complex Nanobelts, *Langmuir*, **2010**, 26, 12330.
[209] Zhang, H., Yang, X., Synthesis of tetra-layer polymer composite microspheres and the corresponding hollow polymer microspheres with Au nanoparticles functionalized movable cores, *Polymer. Chem.*, **2010**, 1, 670.
[210] Deng, Y., Cai, Y., Sun, Z., Liu, J., Liu, C., Wei, J., Li, W., Liu, C., Wang, Y., Zhao, D., Multifunctional Mesoporous Composite Microspheres with Well-Designed Nanostructure: A Highly Integrated Catalyst System, *J. Am. Chem. Soc.*, **2010**, 132, 8466.
[211] Dasog, M., Hou, W., Scott, R.W.J., Controlled growth and catalytic activity of gold monolayer protected clusters in presence of borohydride salts, *Chem. Commun.*, **2011**, 47, 8569.
[212] Hortigueela, M.J., Aranaz, I., Gutierrez, M.C., Luisa Ferrer, M., del Monte, F., Chitosan Gelation Induced by the in Situ Formation of Gold Nanoparticles and Its Processing into Macroporous Scaffolds, *Biomacromolecules*, **2011**, 12, 179.
[213] Jan, J.-S., Chen, P.-J., Ho, Y.-H., Bioassisted synthesis of catalytic gold/silica nanotubes using layer-by-layer assembled polypeptide templates, *J. Colloid Interface Sci.*, **2011**, 358, 409.
[214] Koga, H., Kitaoka, T., One-step synthesis of gold nanocatalysts on a microstructured paper matrix for the reduction of 4-nitrophenol, *Chem. Eng. J.*, **2011**, 168, 420.
[215] Lin, F.-h., Doong, R.-a., Bifunctional Au-Fe(3)O(4) Heterostructures for Magnetically Recyclable Catalysis of Nitrophenol Reduction, *J. Phys. Chem. C*, **2011**, 115, 6591.
[216] Wu, F., Yang, Q., Ammonium bicarbonate reduction route to uniform gold nanoparticles and their applications in catalysis and surface-enhanced Raman scattering, *Nano Res.*, **2011**, 4, 861.
[217] Yazid, H., Adnan, R., Farrukh, M.A., Hamid, S.A., Synthesis of Au/Al(2)O(3) Nanocatalyst and its Application in the Reduction of p-Nitrophenol, *J. Chin. Chem. Soc.*, **2011**, 58, 593.
[218] Zhang, Z., Shao, C., Zou, P., Zhang, P., Zhang, M., Mu, J., Guo, Z., Li, X., Wang, C., Liu, Y., In situ assembly of well-dispersed gold nanoparticles on electrospun silica nanotubes for catalytic reduction of 4-nitrophenol, *Chem. Commun.*, **2011**, 47, 3906.
[219] Zhu, Y., Shen, J., Zhou, K., Chen, C., Yang, X., Li, C., Multifunctional Magnetic Composite Microspheres with in Situ Growth Au Nanoparticles: A Highly Efficient Catalyst System, *J. Phys. Chem. C*, **2011**, 115, 1614.
[220] Balamurugan, A., Ho, K.-C., Chen, S.-M., One-pot synthesis of highly stable silver nanoparticles-conducting polymer nanocomposite and its catalytic application, *Synth. Met.*, **2009**, 159, 2544.
[221] Rashid, M.H., Mandal, T.K., Synthesis and catalytic application of nanostructured silver Dendrites, *J. Phys. Chem. C*, **2007**, 111, 16750.
[222] Liu, P., Zhao, M., Silver nanoparticle supported on halloysite nanotubes catalyzed reduction of 4-nitrophenol (4-NP), *Appl. Surf. Sci.*, **2009**, 255, 3989.
[223] Tang, S., Vongehr, S., Meng, X., Carbon Spheres with Controllable Silver Nanoparticle Doping, *J. Phys. Chem. C*, **2010**, 114, 977.

[224] Leelavathi, A., Rao, T.U.B., Pradeep, T., Supported quantum clusters of silver as enhanced catalysts for reduction, *Nanoscale Res. Lett.*, **2011**, 6, 123.
[225] He, H., Gao, C., Synthesis of Fe(3)O(4)/Pt Nanoparticles Decorated Carbon Nanotubes and Their Use as Magnetically Recyclable Catalysts, *J. Nanomater.*, **2011**.
[226] Wang, R., Jiang, X., Yu, B., Yin, J., Stimuli-responsive microgels formed by hyperbranched poly(ether amine) decorated with platinum nanoparticles, *Soft. Matter.*, **2011**, 7, 8619.
[227] Hoseini, S.J., Rashidi, M., Bahrami, M., Platinum nanostructures at the liquid-liquid interface: catalytic reduction of p-nitrophenol to p-aminophenol, *J. Mater. Chem.*, **2011**, 21, 16170.
[228] Komathi, S., Palaniappan, S., Manisankar, P., Gopalan, A.I., Lee, K.-P., Large Scale Preparation of Palladium Nanoparticles Loaded Polyaniline Nanostructures through Seed Induced Bulk Polymerization, *Macromol. Chem. Phys.*, **2010**, 211, 1330.
[229] Morere, J., Tenorio, M.J., Torralvo, M.J., Pando, C., Renuncio, J.A.R., Cabanas, A., Deposition of Pd into mesoporous silica SBA-15 using supercritical carbon dioxide, *J. Supercrit. Fluids*, **2011**, 56, 213.
[230] Endo, T., Yoshimura, T., Esumi, K., Synthesis and catalytic activity of gold-silver binary nanoparticles stabilized by PAMAM dendrimer, *J. Colloid Interface Sci.*, **2005**, 286, 602.
[231] Kim, M., Lee, K.Y., Jeong, G.H., Jang, J., Han, S.W., Fabrication of Au-Ag alloy nanoprisms with enhanced catalytic activity, *Chem. Lett.*, **2007**, 36, 1350.
[232] Oh, S.-D., Kim, M.-R., Choi, S.-H., Chun, J.-H., Lee, K.-P., Gopalan, A., Hwang, C.-G., Sang-Ho, K., Hoon, O.J., Radiolytic synthesis of Pd-M (M = Ag, Au, Cu, Ni and Pt) alloy nanoparticles and their use in reduction of 4-nitrophenol, *J. Ind. Eng. Chem.*, **2008**, 14, 687.
[233] Samal, A.K., Pradeep, T., Pt(3)Te(4) Nanoparticles from Tellurium Nanowires, *Langmuir*, **2010**, 26, 19136.
[234] Tang, S., Vongehr, S., Meng, X., Controllable incorporation of Ag and Ag-Au nanoparticles in carbon spheres for tunable optical and catalytic properties, *J. Mater. Chem.*, **2010**, 20, 5436.
[235] Harish, S., Sabarinathan, R., Joseph, J., Phani, K.L.N., Role of pH in the synthesis of 3-aminopropyl trimethoxysilane stabilized colloidal gold/silver and their alloy sols and their application to catalysis, *Mater. Chem. Phys.*, **2011**, 127, 203.
[236] Kim, K., Kim, K.L., Shin, K.S., Co-reduced Ag/Pd Bimetallic Nanoparticles: Surface Enrichment of Pd Revealed by Raman Spectroscopy, *J. Phys. Chem. C*, **2011**, 115, 14844.

Appendix

In the following are tables with literature data for the reduction of *p*-nitrophenol. The tables are organized according to metals employed in the catalysis, the stabilizing system, the temperature, size of the nanoparticles, and the apparent rate constant. The term "graphic" here implies that the apparent rate constant is plotted in the respective paper, but the actual value is not given. In the "comments" additional information about the system and other interesting values like activation energy or the normalized rate constants is mentioned.

Table 23: Summary of the p-nitrophenol reduction by gold nanoparticles. The stabilizing system, the reaction temperature, the size of the nanoparticles and the apparent rate constant are given as well, if denoted in the corresponding reference.

Reference (Au NP)	Stabilization	T [°C]	comments	Size [nm]	k_{app} [s^{-1}]
Wu *et al.* [114]	hollow capsule	-	-	2.3 ±0.8	0.002
Lee *et al.* [198]	azacryptand	25	-	20.9±3.3	0.01
Lee *et al.* [198]	citrate	25	-	19.6±3.7	0.002
Zhang *et al.* [199]	horse spleen apoferritin	25	-	3.6±1.2	-
Kumar *et al.* [200]	3,4-ethylenedioxy-thiophene/polystyrene sulfonate	25	-	26.3±1.5	0.0439
Wang *et al.* [122]	micelle (PNIPAM-poly(4-vinyl pyridine)	25	LCST	3.3±0.2	0.00144
Rahsid *et al.* [201]	unstabilized	-	sedimentation after 6 h	100±22	0.0012
Tang *et al.* [202]	collagen	-	different rations collagen/Au	6.5±3.1 (0.05) 5.9±0.9 (0.1) 3.6±0.6 (0.2)	graphic
Chen *et al.* [123]	micelle (poly(styrene)-b-poly(4-vinyl pyridine)	20	k_1, E_A (graphic)	~15	0.00315
Lee *et al.* [203]	silica gel		column of silica gel	~10	-
Wang *et al.*	micelle (PNIPAM-*b*-		LCST	2	graphic

[204]	poly(4-*vinyl pyridine)				
Murugadoss *et al.* [138]	citrate	RT	chain like aggregates due to acetanilide, k_1	5.0±1.7	0.00503
Chen *et al.* [124]	poly(ethylene glycol)-*b*-poly(styrene)-*b*-(4-vinlypyridine)	20	-	3	0.00265
Selvarraju *et al.* [205]	DNA	25	-	8.1±0.8	
Zhang [128]	polymer brush (poly(2-(dimethyl amino) ethyl methacrylate)	RT	LCST	4.2±1.12	0.0032
Chen *et al.* [206]	polymer (poly(*N*,*N*-dimethylamino ethyl methacrylate)	35	LCST	…	graphic
Yang *et al.* [117]	mesoporous organic gel	RT	-	8	0.0079
Huang *et al.* [173]	cyclodextrin	25	-	11.2±1.1	0.00465
				20.1±1.4	0.00345
				26.2±1.8	0.00298
Khaavka *et al.* [81]	CTAB	-	rods	length ca. 62 width ca. 30	graphic
Han *et al.* [139]	polyaniline fibers	RT	-	~2	0.00117
Juarez *et al.* [207]	fibrils		-	3.7-8.0	graph
Li *et al.* [208]	surfactant	20	nanobelt	length several µm	0.00372 (solid)
					0.00999 (porous)
Zhang *et al.* [209]	nanorattle, with an Au-doped movable core	RT	nanorattles	4.5	-
Deng *et al.* [210]	mesoporous microsphere	25	shell thickness of the carrier: 90 nm 40 nm 20 nm	12	0.0033 0.0042 0.0058
Chen *et al.* [125]	micelle (polystyrene-b-poly(acrylic acid)	20	-	2-3	graphic
Schrinner *et al.* [44]	spherical polyelectrolyte brush	20	k_1	1-3	-
Kuroda *et al.* [141]	poly(methyl methacrylate)	22	E_A, k_1	6.9±5.5	0.0072-0.0079

Panigrahi *et al.* [131]	anion exchange resin	25	E_A, different sizes of NP, k_1 graph	20	0.00163
Chang *et al.* [155]	core shell (Fe_2O_3-chitosan)	30	E_A	3.14	0.0125
Saha *et al.* [152]	calcium alginate	-	E_A, cero-order	5±2	-
Zeng *et al.* [156]		24	nanobox, E_A	cage	0.0477
				box	0.0187
				partial hollow box	0.00983
Dasog *et al.* [211]	monolayer stabilized	-	PVP	2.9±0.3	0.0115
			C18SH	1.9±0.2	0.00467
			C12SH	1.6±0.2	0.00517
			C6SH	1.9±0.2	0.00583
			MUA	1.9±0.2	0.003
Hortigüela *et al.* [212]	Chitosan		different mass Au employed	~5	$6 \cdot 10^{-5}$
Jan *et al.* [213]	poly(L-lysine)-poly(L-tyrosine) multilayer films		different gold content	10 -18	0.0012
Koga *et al.* [214]	ceramic fibers containing ZnO whiskers	25		4.3±2.1	0.024
Lin *et al.* [215]	Bifunctional Au-Fe_3O_4 Heterostructures	.		12-16 Dumbell	0.0105
				20-28 flower	0.0063
Wu *et al.* [216]	sodium stearate	RT		9	0.00843
				12	0.00722
				17	0.00594
Wu *et al.* [142]	nano-rattle of Au core, hollow silica shell	25	k_{nor}	2.8±0.7	0.00065
				3.3±0.6	0.001
				4.5±0.7	0.000783
Yazid *et al.* [217]	Alumina	RT		5.27 ± 1.08	0.0079
				5.09 ± 1.64	0.0068
				5.71 ± 1.74	0.0077
Zhang *et al.* [218]	Silica nanotubes	-		3-5	0.001064
Zhu *et al.* [219]	Fe_3O_4@SiO_2 core with PE shell by layer by layer	-	1 coated layer of PE	4	0.00307
			2 coated layer		0.0035
			3 coated layer		0.00567

Table 24: Summary of the p-nitrophenol reduction by silver nanoparticles. The stabilizing system, the reaction temperature, the size of the nanoparticles and the apparent rate constant are given as well, if denoted in the corresponding reference.

Reference (Ag NP)	Stabilization	T [°C]	comments	Size [nm]	k_{app} [s^{-1}]
Saha *et al.* [152]	calcium alginate	-	E_A, cero-order	7±2	-
Esumi *et al.* [112]	dendrimer	-	PAMAM (G4, 10mM)	6.5±1.9	0.00059
			PPI (G4,10mM)	5.5±1.9	0.000467
Murrudagoss *et al.* [147]	chitosan	23-24	-	3	0.0015
Pradhan *et al.* [75]		-	E_A	25	graphic
Liu *et al.* [174]	PAA/G3-PAMAM	-	Reaction complete after 120 min	5-10	-
Lu *et al.* [127]	SPB (PS-PAA)	20	k_1	3 ±1.2	graphic
Lu et al. [146]	PVA	20	k_1	35±5	graphic
	PVA/PS-PEGMA	20	k_1	45±5	graphic
Lu *et al.* [126]	SPB (nanotree)	20	k_1	7.5±2	graphic
Lu *et al.* [150]	PS-PNIPAM	20	k_1 with three different sizes of NP	8.5±1.5	graphic
				7.3±1.5	
				6.5±1.0	
Balamurugan *et al.* [220]	poly(3,4 ethylene dioxythiophene)-PSS	25	only UV-vis spectra 200-600 nm	10-15	-
Rahsid *et al.* [221]	Citrate stabilized – Ag dendrites	-	Different dendrites structures	(corall-shaped)	0.00519
				(banana leave shaped)	0.00165
				(banana leave shaped)	0.00278
				40	0.00036
Shin *et al.* [154]	Fe_2O_3	35	E_A	5-10	0.015
Liu *et al.* [222]	halloysite nanotubes	-		10	graphic
Tang *et al.* [223]	Carbon sphere	-		10±2	0.00169

Manesh *et al.* [153]	poly[*N*-(3-Tri-methoxy silyl) propyl] aniline	30	E_A	10	0.00317
Jana *et al.* [151]	PS sphere coated with Ag	30	E_A	Shell thickness:30 ±5	0.0053
Zhang *et al.* [120]	poly[NIPAM-(maleated carboxy-methylchitosan)] with crosslinker	-	k_1	2.81±0.62	graphic
	poly[NIPAM-(maleated carboxy-methylchitosan)] without crosslinker	-	k_1	3.45±0.64	graphic
Eising *et al.* [145]	Dextran	25	k_1	6.1±1.3	graphic
Leelavathi *et al.* [224]	Mercaptosuccinic acid	-	E_A, cluster: Ag_7, Ag_8	-	graphic

Table 25: Summary of the p-nitrophenol reduction by platinum nanoparticles. The stabilizing system, the reaction temperature, the size of the nanoparticles and the apparent rate constant are given as well, if denoted in the corresponding reference.

Reference (Pt NP)	Stabilization	T [°C]	comments	Size [nm]	k_{app} [s^{-1}]
Esumi *et al.* [112]	dendrimer		PAMAM (G4, 10mM)	1.5±0.35	0.00262
			PPI (G4,10mM)	1.5±0.23	0.147
Mei *et al.* [58]	SPB	30	k_1	2.1±0.4	0.0095
		15	k_1	2.1±0.4	0.00347
Mahmoud *et al.* [157]	Timethyltetradecyl ammonium bromide	25	Ea, cubic NP	20	$6.2 \cdot 10^{-4}$
	PS			20	$9.5 \cdot 10^{-5}$
Mahmoud *et al.* [158]	-	25	hollow cubic NP, E_A	length 74	$6.0 \cdot 10^{-5}$
He *et al.* [225]	multiwalled carbon nanotubes			2.5	0.0192
Wang *et al.* [226]	microgels hyperbrunched poly(ether amine)	15		7.2±0.1	0.00033
Hoseini *et al.* [227]	polyvinylpyrrolidone	25	PVP thin film	- (nanosheets)	0.00214
			without stabilizer		0.00198
			aminoclay thin film		0.00384

Table 26: Summary of the p-nitrophenol reduction by palladium nanoparticles. The stabilizing system, the reaction temperature, the size of the nanoparticles and the apparent rate constant are given as well, if denoted in the corresponding reference.

Reference (Pd NP)	Stabilization	T [°C]	comments	Size [nm]	k_{app} [s^{-1}]
Esumi *et al.* [112]	dendrimer		PAMAM (G4, 10 mM)	1.8±0.42	0.00179
			PPI (G4,10 mM)	1.6±0.36	0.1153
Mahmoud *et al.* [158]	-	25	hollow cubic NP, E_A	length: 74	$3.2 \cdot 10^{-4}$
Mei *et al.* [56]	SPB	15	k_1	2.4±0.5	0.00441
	Microgel	15	k_1	3.8±0.6	0.0015
Harish *et al.* [132]	poly(3,4-ethylene dioxythiophene)-PSS	25		1-9	0.0658
Komathi *et al.* [228]	polyaniline	RT	for 0.39 mg catalyst	7-15	0.011 (mol/L s)
Arora *et al.* [136]	Al_2O_3	25	E_A, k_1 (graphic)	6.0±0.5	graphic
Morere *et al.* [229]	SBA-15	20		8	0.012

Table 27: Summary of the p-nitrophenol reduction by bimetallic nanoparticles. The stabilizing system, the reaction temperature, the size of the nanoparticles and the apparent rate constant (the values in brackets give the ration of the metals) are given as well, if denoted in the corresponding reference.

Reference (bimetallic NP)	Stabilization	T [°C]	comments	Size [nm]	k_{app} [s^{-1}]
Mahmoud. *et al.* [158]	(Pt Pd Alloy)	25	hollow cubic NP, E_A	length 74Pd-Pt	0.00022
	(Pt-Pd nanocube)				$3.2 \cdot 10^{-4}$
	(Pd-Pt nanocube)				$5.8 \cdot 10^{-5}$
Endo *et al.* [230]	Dendrimer (Au-Ag)	25	k_{app} depend on amount of Au	3-4	graphic
Kim *et al.* [231]	PVP (Au-Ag nanoprism)		k_{app} depend on Au content	Edge size 84, thickness 8.8±3	0.00393 (10:90)
Endo *et al.* [113]	Dendrimer (Au-Pt)		k_{app} depend on amount of Au	2.7-2.9	graphic
	Dendrimer (Au-Pd)		k_{app} dependent on the amount of Au	2.0-2.7	graphic

	Dendrimer (Pt-Pd)		k_{app} depend on amount of Pt	1.8-2.1	graphic
Oh *et al.* [232]	PVP (Pd–M (M = Ag, Au, Cu, Ni and Pt)	RT	k_{app} depend on scond metal	20-30 (Pd-Ag), 15 (Pd-Cu), 5-10 (Pd--Ni), 2-5 (Pd-Pt)	graphic
Samal *et al.* [233]	- (Pt_3Te_4)	-	aggregates of small NP	4 (aggregates 200 nm)	0.0013
Lu *et al.* [118]	Microgel (Au-Pt)	25	k_1	length: 34.5±5.2, width: 6.6±0.3	graphic
Tang *et al.* [234]	Carbon sphere (Ag-Au/Ag)	RT	k_{app} dependent on Au content	10	0.00169(Ag)
					0.00296 (0.5:1)
					0.00646 (2.6:1)
					0.00547 (6:1)
Gosh *et al.* [78]	CTAB (Pt-Ni)	30	E_A	20±2.5	$1.25 \cdot 10^{-5}$(Pt)
				19±2.75	$4.83 \cdot 10^{-4}$ (64:36)
				20±2	$9.0 \cdot 10^{-4}$ (80:20)
				19±3	$1.93 \cdot 10^{-3}$ (96:4)
				Raney Ni	$1.48 \cdot 10^{-4}$
Harish *et al.* [235]	modified aminosilicate sol (Au-Ag)	25	different ratio Au:Ag	7.8 4.2 7.8	0.006133 (au) 0.027 (50:50) 0.01995 (ag)
Kim *et al.* [236]	- (Ag:Pd)	25	Alloy NP, depend on Pd content	56 (ag) 53 (98:2) 29 (95:2) 5.3 (Pd)	graphic
Mahmoud *et al.* [168]	Au nanocubes	25	wall thickness: 20	length: 64	0.102
	AuPt nanocubes		13		0.019
	Au nanocubes		10		0.079
	AuPt nanocubes		10		0.029
	Au nanocubes		9		0.106
	AuPt nanocubes		7		0.014

5.4 Activation Energies of *p*-Nitrophenol Reduction

In the following table (Table 28) the recalculated activation energies and pre-exponential factors are listed. The values in brackets are the values given in the literature, if they derivate strongly with the recalculated values.

Table 28: Recalculated values for the activation energies and pre-exponential factors (k_0) for activation energies in the literature according to the metal applied in the study, concentration of p-nitrophenol and borohydride as well as the size of the nanoparticles.

Ref	Metal	c_{Nip} [M]	c_{BH4} [M]	d_{NP} [nm]	k_0 [s^{-1}]	E_A [kJ mol^{-1}]
Panigrahni *et al.* [131]	Au NP (citrate-stabilized)	$1.00x10^{-4}$	$6.67x10^{-3}$	20	$4.5x10^{2}$	31
Chen *et al.* [123]	Au NP (PS-P4VP micelles)	$1.10x10^{-4}$	$3.60x10^{-1}$	15	$1.7x10^{1}$	23
Chang *et al.* [155]	Au-NP (chitosan-coated ironoxide carrier)	$2.00x10^{-4}$	$6.67x10^{-4}$	3.1	$4.8x10^{5}$	51
Kuroda *et al.* [141]	Au NP (PMMA beads)	$4.94x10^{-5}$	$7.22x10^{-2}$	6.9	$4.3x10^{4}$	38
Shin *et al.* [154]	Ag NP (Fe_2O_3 carrier)	$1.03x10^{-4}$	$1.05x10^{-2}$	~28	$8x10^{5}$	45
Arora *et al.* [136]	Pd NP (Al_2O_3)	$1.00x10^{-4}$	$1.32x10^{-2}$	6	$2.1x10^{5}$	43
Mahmoud *et al.* [157]	Pt nanocubes (PS) Pt nanocubes (colloidal)	$1.95x10^{-5}$	$3.16x10^{-2}$	20 20	2.2 3.5	12 (25) 12 (27)
Manesh *et al.* [153]	Ag NP (silica network)	$1.00x10^{-4}$	$1.0x10^{-2}$	10	$5.4x10^{2}$	24 (192)
Zeng *et al.* [156]	Au nanocage Au nanobox Au hollow nanobox	$1.40x10^{-4}$	$4.20x10^{-2}$	50 50 50	$4.5x10^{3}$ $1.1x10^{6}$ $6.0x10^{7}$	28 44 55
Mahmoud *et al.* [158]	Pt Pd Alloy nanocubes Pd nanocubes Pt Pd nanocubes Pd Pt nanocubes Pt nanocubes	$2.60x10^{-4}$	$3.12x10^{-2}$	cavity:49 cavity:53 cavity:57 cavity:51 cavity:52	$2.9x10^{15}$ $8.5x10^{12}$ $1.5x10^{8}$ $3.6x10^{11}$ $3.9x10^{7}$	104 90 74 83 65
Sahiner *et al.* [121]	Ni NP (hydrogel network)	$1.44x10^{-2}$	$2.88x10^{-1}$	100	$2.5x10^{1}$	26
Sahiner *et al.* [119]	Co NP (hydrogel network)	$1.44x10^{-2}$	$2.88x10^{-1}$	50-100	$8.6x10^{1}$	28

Bhandari *et al.* [134]	Pd NP (pepitide stabilized, different ratios)	$1.28x10^{-4}$ $1.20x10^{-4}$ $1.17x10^{-4}$	$3.78x10^{-2}$ $3.57x10^{-2}$ $3.47x10^{-2}$	2.6 - -	$6.5x10^{-1}$ $5.3x10^{-1}$ $9.5x10^{-1}$	7.5 7.2 8.7
Jiang *et al.* [179]	Au-Ag core-shell NP (metal-organic framework)	$1.10x10^{-4}$	$8.7x10^{-2}$	2-6	$4.2x10^{2}$	14
Mahmoud *et al.* [168]	Au nanocubes AuPt nanocubes Au nanocubes AuPt nanocubes Au nanocubes AuPt nanocubes	$1.97x10^{-3}$	2.96	wall thickness: 20 20 10 10 9 9	$5.2x10^{2}$ $5.8x10^{11}$ $8.3x10^{2}$ $6.7x10^{2}$ $4.0x10^{1}$ $2.7x10^{1}$	30 84 32 32 24 30
Lu *et al.* [126]	Ag NP (anionic SPB)	$1.00x10^{-4}$	$1.00x10^{-2}$	7.5	$1.1x10^{8}$	62
This work	Pt NP (cationic SPB)	$1.00x10^{-4}$	$1.00x10^{-2}$	2.3	$2.5x10^{5}$	40
This work	Au NP (cationic SPB)	$1.00x10^{-4}$	$1.00x10^{-2}$	2.2	$3.6x10^{6}$	52

5.5 List of Tables

Table 1: Catalytic activity of metal nanoparticles for the reduction of p-nitrophenol taken or recalculated (*) from literature. 29
Table 2: Catalytic activity of metal nanoparticles embedded inside of SPB for the reduction of p-nitrophenol. 31
Table 3: Activation energies for the p-nitrophenol reduction inclusive the carrier systems, sizes and concentrations of the educts. 34
Table 4: Activation energies for the p-nitrophenol reduction inclusive the carrier systems, sizes and concentrations of the educts. 35
Table 5: Activation energies for the p-nitrophenol reduction inclusive the carrier systems, sizes and concentrations of the educts. 36
Table 6: Summary of the rate constants, and the adsorption constants of Nip and BH_4^- according to eq. 3.11. 50
Table 7: Parameters of the modified Langmuir-Hinshelwood model for the gold nanoparticles in dependency of the temperature T of the intrinsic rate constant k, the adsorption constants K_{nip} and K_{BH4} and the Langmuir Freundlich constants n and m. 52
Table 8: Adsorption enthalpy and entropy derived calculated by equation 3.12 and 3.13 with the data shown in Figure 23. 54
Table 9: Activation energies E_A of the surface normalized rate constants k_1 and the pre-exponential factor k_0 for different concentrations of Nip and BH_4^-. 55
Table 10: Rate constant (k·S) and the adsorption constants for the oxidation of morin with H_2O_2 on MnO_x@SPB obtained by best fit model according to eq. 3.32. 87
Table 11: Rate constant and (k·S) the adsorption constants for the oxidation of morin with H_2O_2 on MnO_x@SPB obtained by best fit model according to eq. 3.32 by setting the exponents n = 1 and m = 0.87. 87
Table 12: Temperature dependence of the adsorption constants of morin and H_2O_2 derived from the Langmuir-Hinshelwood model. 89
Table 13: Chemicals used in this thesis and the supplier 95
Table 14: Concentration variation of p-nitrophenol at 10 mmol L^{-1} borohydride with a constant concentration of catalyst (platinum and gold nanoparticles). 99
Table 15: Concentration variation of p-nitrophenol at 5 mmol L^{-1} borohydride with a constant concentration of catalyst (platinum and gold nanoparticles). 100
Table 16: Concentration variation of borohydride at 0.1 mmol L^{-1} p-nitrophenol with a constant concentration of catalyst (platinum and gold nanoparticles). 100
Table 17: Concentration variation of borohydride at 0.05 mmol L^{-1} p-nitrophenol with a constant concentration of catalyst (platinum and gold nanoparticles). 100
Table 18: Concentration variation of borohydride at 0.025 mmol L^{-1} p-nitrophenol with a constant concentration of catalyst (platinum nanoparticles). 101
Table 19: Concentration variation of morin at 10 mmol L^{-1} H_2O_2 with a constant concentration of catalyst. 102
Table 20: Concentration variation of morin at 5 mmol L^{-1} H_2O_2 with a constant concentration of catalyst. 102
Table 21: Concentration variation of H_2O_2 at 0.1 mmol L^{-1} morin with a constant concentration of catalyst. 102
Table 22: Concentration variation of H_2O_2 at 0.05 mmol L^{-1} morin with a constant concentration of catalyst. 103

Table 23: Summary of the p-nitrophenol reduction by gold nanoparticles. The stabilizing system, the reaction temperature, the size of the nanoparticles and the apparent rate constant are given as well, if denoted in the corresponding reference. 117
Table 24: Summary of the p-nitrophenol reduction by silver nanoparticles. The stabilizing system, the reaction temperature, the size of the nanoparticles and the apparent rate constant are given as well, if denoted in the corresponding reference. 120
Table 25: Summary of the p-nitrophenol reduction by platinum nanoparticles. The stabilizing system, the reaction temperature, the size of the nanoparticles and the apparent rate constant are given as well, if denoted in the corresponding reference. 121
Table 26: Summary of the p-nitrophenol reduction by palladium nanoparticles. The stabilizing system, the reaction temperature, the size of the nanoparticles and the apparent rate constant are given as well, if denoted in the corresponding reference. 122
Table 27: Summary of the p-nitrophenol reduction by bimetallic nanoparticles. The stabilizing system, the reaction temperature, the size of the nanoparticles and the apparent rate constant (the values in brackets give the ration of the metals) are given as well, if denoted in the corresponding reference. 122
Table 28: Recalculated values for the activation energies and pre-exponential factors (k_0) for activation energies in the literature according to the metal applied in the study, concentration of p-nitrophenol and borohydride as well as the size of the nanoparticles. 124

5.6 List of Figures

Figure 1: left: Schema of a spherical polyelectrolyte brush system with embedded nanoparticles; right: cryo-TEM micrographs of a) platinum nanoparticles, reprinted with permission from ref [58]. Copyright 2005, American Chemical Society. b) Gold nanoparticles immobilized inside the SPB. Reprinted with permission from ref [44]. Copyright 2007 WILEY-VCH Verlag. 2
Figure 2: UV-vis spectra of the reduction of p-nitrophenol by sodium borohydride with silver nanoparticles. Reprinted from ref [75]. Copyright 2001, with permission from Elsevier. 4
Figure 3: a) Dependence of brush thickness L on pH for annealed PAA brush. The parameter of the data is the ionic strength in the solution, which was adjusted by adding a KCl solution: crosses, 1M; open squares, 0.1M; triangles, 0.01M; open circles, 0.001M; filled squares, 0.0001M. b) Dependence of brush thickness L on pH in the solution for a quenched PSS brush. The parameter of the data is the ionic strength in the solution, which was adjusted by adding KCl. Crosses, 1M; open squares, 0.1M; triangles, 0.01M; open circles, 0.001M; filled squares, 0.0001M. Reprinted figures with permission from ref [41]. Copyright 2001 by the American Physical Society. (http://link.aps.org/doi/10.1103/PhysRevE.64.051406) 9
Figure 4: Cryo-transmission electron microscopy of nanoparticles a) platinum nanoparticles, reprinted with permission from ref [58]. Copyright 2005 American Chemical Society. b) Palladium nanoparticles, reprinted with permission from ref [56]. Copyright 2007 American Chemical Society. c) Gold nanoparticles. Reprinted with permission from ref [44]. Copyright 2007 WILEY-VCH Verlag. 11
Figure 5: a) Cryo-TEM of the composite system SPB-MnO2 and b) the MnOx nanoparticles in a higher magnification. Reprinted with permission from ref [62]. Copyright 2010 American Chemical Society. 12
Figure 6: Reaction scheme of a Eley-Rideal mechanism for a varying the concentrations of A by a constant concentration of B. 18
Figure 7:Dependence of the reaction rate of the reaction on variation of concentration A at a constant concentration B according to Ref [98]. 20
Figure 8: Pure and reconstructed surfaces of the three low index planes of platinum. The 1x1 surface of the Pt(100) is reconstructed to a hexagonal pattern, the Pt (110) surface to a missing row structure. Reprinted with permission from ref [106]. Copyright 1995 American Chemical Society. 22
Figure 9: Model of the CO-induced 1 x 1 and 1 x 2 surface phase transition of Pt (110). On the left side is the restructured of the platinum surface by adsorption of CO, on the right side is the reconstructed surface of the Pt (110) shown. The different sticking coefficients of oxygen, s_{o2}, of the two phases are responsible for rate oscillations during the catalytic CO oxidation. The model also demonstrates how the mass transport of Pt atoms creates an atomic step on the surface. Reprinted with permission from ref [106].Copyright 1995 American Chemical Society. 23
Figure 10: Oscillating waves on a Pt(110) surface during the oxidation of CO. The PEEM (photoemission electron microscope) images demonstrating the temporal evolution of spirals with strongly different rotation periods and wavelengths: T = 448 K, p_{co} = 4.3 x 10^{-5} mbar, and p_{o2} = 4 x 10^{-4} mbar. The spiral with the largest wavelength rotates around a core of 25 x 14 pm^2, while the size of the core region is only 5 x 3 $pm^2$for the fast

rotating spiral visible in the foreground. Reprinted with permission from ref [106].Copyright 1995 American Chemical Society. 24
Figure 11: Absorbance curves of p-nitrophenol at 400 nm at different reaction conditions. (a) Instantaneous addition. (a') Introduction of a fresh batch of substrate Nip to the same reaction mixture just before completion of the reduction, (b) 5 min and (c) 15 min after the completion of the reduction. Reprinted from ref [75]. Copyright 2001 with permission from Elsevier. 26
Figure 12: Dependence of the surface area of the nanoparticles (S) on the apparent rate of the reaction. (squares: Ag@SPB, circles: Ag@PNIPAM, triangle: Pd@PNIPAM, diamonds: Pt@SPB). Reprinted with permission from ref [149]. Copyright 2007 American Chemical Society. 32
Figure 13: Compensation plot of the pre-exponential factors (ln A)and the activation energies (E_a) of the Arrhenius equation for catalysts based on Au nanocages or nanoboxe. Reprinted with permission from ref [156]. Copyright 2010 American Chemical Society. 38
Figure 14: TEM micrographs of the platinum nanoparticles with a diameter of 2.3 nm (a), gold nanoparticles with a size of 1.5 nm (b), and gold nanoparticles with a size of 2.2 nm. Enlarged by the use of the HR-TEM, it can be seen that the gold nanoparticles are facetted. 41
Figure 15: a) UV-vis Spectra of the reduction of p-nitrophenol and b) dependence of the absorption peak of p-nitrophenol at 400 nm with the reaction time. 42
Figure 16: Dependence of the apparent rate constant on the surface of the added nanoparticles, in this case Au NP with a size of 2.2 ± 0.4 nm at constant concentrations of 0.1 mM Nip and 10 mM BH_4^-. 42
Figure 17: Apparent rate constant k_{app} vs. the concentration of Nip (c_{Nip}, left) and BH_4^- (c_{BH4}, right): The surface area of Pt nanoparticles is $S = 0.00687\ m^2\ L^{-1}$ for panels (a) and (c). The Panels (b) and (d) describe the kinetic data taken for Pt-nanoparticles with a surface area of $S = 0.00481\ m^2\ L^{-1}$. 43
Figure 18: Apparent rate constant k_{app} vs. the concentration Nip (c_{Nip}, left) and BH_4^- (c_{BH4}, right): The solid lines show the results of the Langmuir-Hinshelwood-model with a Langmuir isotherm. The surface area of Pt nanoparticles is $S = 0.00687\ m^2\ L^{-1}$ for panels a and c and $S = 0.00481\ m^2\ L^{-1}$ for panels b and d. The arrows mark the strong deviation of the predicted rate constants from the Langmuir-Hinshelwood model. 47
Figure 19: Apparent rate constant k_{app} vs. the concentration Nip (c_{Nip}, left) and BH_4^- (c_{BH4}, right): The lines represent the results of the modified Langmuir-Hinshelwood model. The surface area of Pt nanoparticles is $S = 0.00687\ m^2\ L^{-1}$ for panels a and c and $S = 0.00481\ m^2\ L^{-1}$ for panels b and d. Panels e and f describe the kinetic data obtained for Au nanoparticles. The dashed lines display the calculated results of the modified Langmuir-Hinshelwood model for the gold nanoparticles. The surface area in the case of Au is $S = 0.01078\ m^2\ L^{-1}$. The calculated results of the modified Langmuir-Hinshelwood-model are listed in Table 6. 49
Figure 20: Dependence of the rate constant times the concentration of p-nitrophenol ($k_{app} \cdot c_{Nip}$) on the surface coverage of the nanoparticles ($\theta_{Nip} \cdot \theta_{BH4}$). The solid squares stand for the platinum nanoparticles with $S = 0.00687\ m^2 L^{-1}$, while the hollow squares depict the platinum nanoparticles with $S = 0.00481\ m^2\ L^{-1}$, and the blue diamonds symbolize the gold nanoparticles with $S = 0.01078\ m^2\ L^{-1}$. 50

Figure 21: Arrhenius plot of the apparent rate constant k_1 (black dots) and the inverse induction time t_0 (red diamonds) for platinum nanoparticles with a diameter of 2.3 nm embedded inside spherical polyelectrolyte brushes. 51
Figure 22: Dependence of the temperature on the rate constant at different concentrations of p-nitrophenol (a and b) and different concentrations of borohydride (c and d) for gold nanoparticles (S = 0.0108 m^2 L^{-1}). The temperatures are marked with 10 °C = blue squares; 20 °C = violet dots; 25 °C = red triangles; 30 °C = orange diamonds. The solid lines are the fits for the modified Langmuir-Hinshelwood model. 52
Figure 23: Dependence of the adsorption constant K_{Nip} of Nip (a) and the adsorption constant K_{BH4} of borohydride (b) on the inverse temperature. The enthalpies and entropies of the adsorption process were calculated using van't Hoff's equation (eq. 3.12, solid lines) and the results are listed in Table 8. 54
Figure 24: Compensation plot of different metallic nanoparticles confined in SPB carrier systems from literature (squares: Pt NP from Ref [58] (hollow) and Pt NP from Figure 21 (filled); up triangle: Pd NP;[56] diamond: Ag NP[126]) and from the results of some representative concentrations of p-nitrophenol and sodium borohydride for the Au NP, summarized in Table 9 (orange inverted triangles). 55
Figure 25: Compensation plot of the activation energy E_A and the pre-exponential factor $k_{app,o}$ as recalculated from literature values.[119, 121, 123, 126, 131, 134, 136, 141, 154-158, 168, 179]....56
Figure 26: Dependence of the intrinsic reaction rate k (blue diamonds) and the calculated rate constants with a constant coverage of p-nitrophenol (squares) on inverse temperature. 58
Figure 27: Dependence of the induction time on the concentration of borohydride (a) squares: 0.1 mM Nip, diamonds: 0.05 mM Nip; black/red for platinum nanoparticles, dark/light blue for gold nanoparticles and dependence on p-nitrophenol (b) squares: 10 mM BH_4^-, diamonds: 5 mM BH_4^-; black/red for platinum nanoparticles, dark/light blue for gold nanoparticles. 60
Figure 28: Dependence of the inverse normalized rate constant on the concentration of Nip (black and dark blue for 10 mM borohydride, red and light blue for 5 mM borohydride; with two different concentration of Pt NP: S = 0.00687m^2L^{-1} (filled squares) open squares for Pt NP with S = 0.00481 m^2 L^{-1} (open squares); diamonds for gold nanoparticles S = 0.01078 m^2 L^{-1}. 61
Figure 29: Dependence of the induction time on the concentration of the initial concentration of BH_4 at 0.1 mM (closed symbols) and 0.05 mM Nip (open symbols) (a) and of p-nitrophenol at 10 mM (closed symbols) and 5 mM BH_4 (open symbols) (b) at four different temperatures. The temperatures are symbolized as following: 10 °C = blue squares; 20 °C = violet dots; 25 °C = red triangles; 30 °C = orange diamonds for gold nanoparticles with 2.2 nm size. 62
Figure 30: Temperature dependence of the inverse spontaneous induction time for gold nanoparticles at c_{Nip} = 0 mol L^{-1} derived from the intercept in Figure 29b. 63
Figure 31: Double logarithmic plot of the surface restructuring rate and the surface coverage of p-nitrophenol. Filled symbols represent 10 mM and open symbols 5 mM borohydride. The different temperatures are marked as follows: blue squares: 10 °C; violet dots: 20 °C; red triangles: 25 °C, and orange diamonds: 30 °C for gold nanoparticles with 2.2 nm size. 63
Figure 32: Relation of the substrate induced surface restructuring of the p-nitrophenol covered surface at a) 10 mM and b) 5 mM borohydride. The temperatures are marked

with: blue: 10 °C; violet: 20 °C; red 25 °C, and orange: 30 °C for gold nanoparticles with 2.2 nm. 64
Figure 33: Decomposition of morin to 2,4-dihydroxy benzoic acid and 2,4,6-trihydroxy benzoic acid by a nucleophilic attack in 2-position and ring opening as proposed by Colombini et al..[84] 68
Figure 34: Proposed reaction product of the oxidation of morin by Topalovic [189]. 68
Figure 35: Second-order bicarbonate dependence on the oxidation of different dyes (PADA: trans-pyridine-azo-p-dimethylanilin, MO: morin, PNP: p-nitrophenol). Experimental conditions: $Mn(NO_3)_2$: 0.02 mmol L^{-1}, dye: 0.05 mmol L^{-1}, H_2O_2: 0.01 mol L^{-1}at a pH-value of 8.5 at 25 °C. Repinted from ref [192]. Copyright 2010 with permission from Elsevier. 69
Figure 36: Proposed reaction pathway of the selective epoxidation of alkenes redrawn according to Ref [187]. Mn^{2+} exists on the surface of the MnO-catalysts, which can be coordinated by HCO_4^- on the surface of the catalyst. This intermediate can transfer active atomic oxygen to the C-C-double bond of the alkene and decompose to Mn^{2+} on the surface of the catalyst and CO_3^-.[187] 71
Figure 37: a) Scheme of the manganese oxide containing SPB, the red hexagons symbolizes the platelets of MnO_x NP embedded inside the polyelectrolyte layer. b) Cryo-TEM image of these composite particles, where the platelets of MnO_x NP are wrapped around the dark grey PS core of the SPB.[194] 73
Figure 38: a) Spectra of the first 12 minutes of the oxidation of morin by H_2O_2 on K^+-birnessite nanoparticles, where the isosbestic points are clearly visible. These points are marked by dashed lines. The time between the spectra is two minutes. b) Spectra over the whole reaction time of about one hour; the spectra are taken each 4 minutes. The reaction conditions are: 10 mg L^{-1} MnO_x@SPB, 10 mM H_2O_2, 0.1 mM morin in 50 mM carbonate buffer solution. 74
Figure 39: a) Spectra of the oxidation of morin normalized by the spectra at 58 minutes, where the main absorption peak at 410 nm is diminished. b) Peak development using the normalized spectra at 58 minutes. The analyzing of peak II (310 nm) is difficult, due to the fact, that the peak maximum shifts to higher wavelengths with propagating reaction time, c) normalized absorption of the peaks at t = 0 to a value of 1, d) logarithmic plot of the peak development with time. For a better comparison the peak at 310 nm is multiplied by -1. 75
Figure 40: UV-vis-spectra of the oxidation of morin without H_2O_2, where all stock solutions were purged with nitrogen to remove dissolved oxygen (a), and when the stock solutions were not purged with nitrogen (b). The reaction conditions were: 10 mg L^{-1} MnO_x@SPB, 0.1 mM morin in 50 mM carbonate buffer solution, spectra taken every 2 minutes. 76
Figure 41: a) UV-vis spectra of the reaction of morin without H_2O_2 in unpurged solutions. Spectra are taken every 8 minutes. The reaction conditions are: 10 mg L^{-1} MnO_x@SPB, 0.1 mM morin in 50 mM carbonate buffer solution. b) After the peak at 320 nm reaches a stable maximum, the solution is filtered to remove the catalyst. Thereafter, H_2O_2 is added and spectra are recorded every 4 minutes. The inset shows the adsorption spectra of the substances **5** (2,4,6-trihydroxy benzoic acid) and **6** (2,4-dihydroxy benzoic acid). The absorption maxima are in both cases at approximately 275 nm at 20 °C in 50 mM carbonate buffer solution. 77
Figure 42: The filled symbols display measurements, for which the solutions are purged with nitrogen. Open symbols represent measurements without purging with nitrogen.

The black squares symbolize measurements with H_2O_2 (10 mM H_2O_2), the dots and circles depict measurements without H_2O_2. The red dots show measurements of solutions, purged with nitrogen, whereas the purple dots represent measurements, for which the cuvette was additionally closed, to prevent dissolving of oxygen. Reaction conditions: 20 °C, 0.1 mM morin, 20 mg L^{-1} MnO_x@SPB. a) Dependence of the reaction conditions on the peak evaluation at 310 nm. b) Dependence of the reaction conditions on the peak evaluation at 410 nm. 78
Figure 43: Dependence of the rate constant on the content of manganese oxide (c_{morin} = 0.1 mM, c_{H2O2} = 10 mM, carbonate buffer concentration = 12.5 mM, T = 20 °C). The black dots denote measurements directly after the synthesis of the MnO_x@SPB. The red diamonds represent the same measurements for MnO_x@SPB particles stored for nearly six month. 80
Figure 44: Dependence of the rate constant on the concentration of carbonate ions in solution (blue dots) and on the boric acid concentration (green diamonds). The arrow marks the carbonate concentration which is used in the Langmuir-Hinshelwood analysis. Reaction conditions: 10 mg L^{-1} MnO_x@SPB, 10 mM H_2O_2, 0.1 mM morin. 81
Figure 45: Catalytic oxidation of morin on MnO_x-nanoparticles with H_2O_2 a) in CHES buffer (pH 10) and b) in borax buffer (pH 10). Spectra are taken every 2 minutes. Reaction conditions: 10 mg L^{-1} MnO_x@SPB, 10 mM H_2O_2, 0.1 mM morin, T = 20 °C. ...82
Figure 46: Left: influence of the concentration of H_2O_2 on the apparent rate constant k_{app} of the catalytic oxidation of morin with c_{morin} = 0.1 mM (filled symbols) and c_{morin} = 0.05 mM (open symbols) at c_{Mn} = 0.039 mg L^{-1} at different temperatures (blue squares = 15 °C, purple circles = 20 °C, red upright triangles = 25 °C, and orange inverted triangles = 30 °C). Right: influence of the concentration of morin on the apparent rate constant k_{app} of the catalytic oxidation of morin with c_{H2O2} = 10 mM (filled symbols) and c_{H2O2} = 5 mM (open symbols) at c_{Mn} = 0.039 mg L^{-1} at different temperatures (blue squares = 15 °C, purple circles = 20 °C, red upright triangles = 25 °C, and orange inverted triangles = 30 °C). The solid lines mark the fits by the Langmuir-Hinshelwood model. 83
Figure 47: Mechanistic model of the oxidation of morin by H_2O_2 in the presence of manganese oxide nanoparticles (red hexagons) according to a Langmuir-Hinshelwood mechanism. These metal oxide nanoparticles are embedded in the brush layer of cationic SPB. The reaction of H_2O_2 with the surface leads to adsorbed active oxygen species and water is released. Parallel, morin adsorbs onto the nanoparticle surface. The reaction of morin with the active oxygen species on the surface is the rate determining step (RDS) of the overall catalytic cycle. Finally, the decomposition product of morin (DP) desorbs from the catalyst surface, leaving a free active site for a new catalytic reaction. 84
Figure 48: Langmuir-Hinshelwood analysis for different buffer systems: black points: 50 mM carbonate buffer; green squares: 12.5 mM carbonate buffer; red hollow circles: borax buffer at 20°C for the concentration variations of H_2O_2 (a) and the concentration variation of morin (b) at 10 mg L^{-1} MnO_x@SPB. 86
Figure 49: Temperature dependence of the intrinsic rate constant (a), the adsorption constants K_{morin} (blue dots) and K_{H2O2} (cyan diamonds) (b) and the apparent rate constants for two buffer concentrations (red diamonds: 12.5 mM; black dots: 50 mM) (c). a and b are measured with the 50 mM carbonate buffer solution. 88

Abbreviations

AEMH	2-aminoethyl methacrylate hydrochloride
BH_4	borohydride
CHES	(2-(cyclohexylamino)ethanesulfonic acid)
CTAB	hexadecyltrimethylammonium bromide
DMEMA	2-(dimethylamino) ethyl methacrylate
LH	Langmuir-Hinshelwood
LF	Langmuir Freundlich
morin	3,5,7,2',4'-pentahydroxy flavone
MnO_x@SPB	manganese oxide nanoparticles embedded inside SPB carrier systems
Nip	*p*-nitrophenol
NP	nanoparticles
P4VP	Poly(4-vinyl pyridine)
PAA	poly(acrylic acid)
PAMAM	poly(amido amine)
PANI	poly(aniline)
PEDOT	poly(3,4-ethylenedioxythiophene)
PEI	poly(ethylene imide)
PNIPAM	poly(*N*-isoproplyacrylamide)
PPI	poly(propylene imine)
PS	poly(styrene)
PSS	poly(styrene sulfonate)
PVA	poly(vinyl alcohol)
rds	rate determining step
ref	reference
SPB	spherical polyelectrolyte brush
TMAEMAC	2-[(methacryloyloxy)ethyl]trimethylammonium chloride
TMAPMAA	3-trimethylammonium propyl methacrylamide chloride
V50	α,α′-Azodiisobutyramidine dihydrochloride
wt. %	weight percent
$\Delta H°$	standard enthalpy change
$\Delta S°$	standard entropy change
c_i	concentration of i
D	diffusion constant
d	diameter
$E(\lambda)$	extinction
E_A	activation energy
$E_{A,0}$	true activation energy
$E_{A,app}$	apparent activation energy
E_{ad}	adsorption energy
F	collision frequency
$f(\theta)$	free adsorption site

$f(\theta)$	occupied adsorption site
I	the intensity of the outgoing light
I_0	intensity of the incoming light
k	intrinsic rate constant
$K^{\ddagger}$	equilibrium constant
k_0	pre-exponential factor
k_1	surface normalized rate constant
k_{ad}	adsorption rate
k_{app}	apparent rate constant
k_B	Boltzmann constant
k_{des}	desorption rate
k_{et}	electron transfer rate
k_{H2O2}	overall reaction rate independent of the concentration of H_2O_2
K_i	adsorption constant of i
k_{iso}	isokinetic rate constant
L	brush thickness
m	mass
m, n	Freundlich exponents
p	pressure
p	slope of the compensation plot
q	intercept of the compensation plot
Q_{ad}	heat of adsorption
R	radius
r	reaction rate
R	gas constant
r_{ad}	rate of adsorption
r_{des}	rate of desorption
R_H	hydrodynamic radius
r_{H2O2}	rate of the H_2O_2 decomposition
S	surface of nanoparticles
s	sticking coefficient
T	temperature
t_0	induction time
$t_{0,sp}$	spontaneous induction time
T_{iso}	isokinetic temperature
δ	characteristic length scale
δ	grafting density
$\Delta H^{\ddagger}$	enthalpy of activation
ΔH_{ad}	enthalpy of adsorption
$\Delta S^{\ddagger}$	entropy of activation
ΔS_{ad}	entropy of adsorption
$\varepsilon(\lambda)$	extinctions coefficient
η	dynamic viscosity
θ_{H2O2}	surface coverage of H_2O_2
θ_i	surface coverage of i
λ	wavelength
ν	velocity
ν	reaction order ($r(\theta) = r_0 \cdot \theta^{\nu}$)

σ	probability of the right adsorption energy

cryo-TEM	cryogenic temperature transmission electron microscopy
DLS	dynamic ligth scattering
EDX	Energy-dispersive X-ray spectroscopy
HR-TEM	high resolution transmission electron microscopy
NMR	nuclear magnetic resonance spectroscopy
PEEM	photoemission electron microscope
PXRD	powder X-ray diffraction
SAXS	small angle X-ray scattering
TEM	transmission electron microscopy
TGA	thermogravimetric ananlysis
UV-vis	ultra violet spectroscopy
XRD	X-ray diffraction

Publications

S. Wunder, F. Polzer, Y. Lu, Y. Mei, M. Ballauff "Kinetic Analysis of Catalytic Reduction of 4-Nitrophenol by Metallic Nanoparticles Immobilized in Spherical Polyelectrolyte Brushes." *J. Phys. Chem. C*, **2010**, 114 (19), pp. 8814-4420.

S. Wunder, Y. Lu, M. Albrecht, M. Ballauff "Catalytic Activity of Faceted Gold Nanoparticles Studied by a Model Reaction: Evidence for Substrate-Induced Surface Restructuring." *ACS Catal*., **2011**, 1 (8), pp. 908-916.

F. Polzer, S. Wunder, Y. Lu, M. Ballauff "Oxidation of an Organic Dye Catalyzed by MnO_x Nanoparticles." *J. Catal*., **2012**, 289, pp. 80-87.

J. Y. Yuan, S. Wunder, F. Warmuth, Y. Lu "Spherical polymer brushes with vinylimidazolium-type poly(ionic liquid) chains as support for metallic nanoparticle." *Polymer*, **2012**, 53 (1), 43-49.

J. Kaiser, L. Leppert, H. Welz, F. Polzer, S. Wunder, N. Wanderka, M. Albrecht, T. Lunkenbein, J. Breu, S. Kümmel, Y. Lu, M.Ballauff "Catalytic activity of nanoalloys from gold and palladium." *Phys. Chem. Chem. Phys.*, **2012**, 14, pp. 6487-6495.

M. Sommer, S. Hüttner, S. Wunder, M. Thelakkat "Electron-Conducting Block Copolymers: Morphological, Optical, and Electronic Properties." *Adv. Mater*. **2008**, 20 (13), pp. 2523-2527.

Acknowledgment

At this point I want to take the opportunity to thank all the people, who helped me to complete this work.

I would like to thank Prof. Matthias Ballauff for scientific guidance, advice, support, and for providing a very pleasant working environment.

Furthermore I'd like to express my gratitude to my supervisor Dr. Yan Lu for the help and discussions whether in questions about the synthesis of the particles or UV-measurements especially at the beginning of this work.

I'd like to thank all my colleagues and friends, whether in Bayreuth or in Berlin for the enjoyable time, especially Miriam Siebenbürger, Christoph Hollfelder, Kathrin Holtzmann, Julian Kaiser, Christian Rabe, Katja Henzler and Björn Haupt. I am very grateful for all the scientific discussions and I would like to appreciate the very interesting coffee time discussions.

Special thanks to Yvonne Hertl, Frank Polzer and Julian Kaiser for the TEM measurements and Martin Albrecht for the HR-TEM measurements.

Frank Polzer, I want to thank for all the discussions surrounding the topic "catalysis".

Special thanks goes to Ralf Stehle for the patience of the last weeks.

Last, but not least, I want to thank my family, without their love, guidance and support this would not have been possible.

Selbständigkeitserklärung

Hiermit versichere ich die vorliegende Dissertation selbst verfasst und nur unter Zuhilfenahme der angegebenen Hilfsmittel angefertigt zu haben.

Berlin,den Stefanie Wunder